APPLICATION OF LINEAR SWITCHED RELUCTANCE ACTUATOR IN ACTIVE SUSPENSION SYSTEMS

ZHANG ZHU

Ph.D

The Hong Kong Polytechnic University

2012

THE HONG KONG POLYTECHNIC UNIVERSITY

Department of Electrical Engineering

APPLICATION OF LINEAR SWITCHED RELUCTANCE ACTUATOR IN ACTIVE SUSPENSION SYSTEMS

ZHANG ZHU

A thesis submitted in partial fulfillment of the requirements

For the degree of Doctor of Philosophy

March 2012

CERTIFICATE OF ORIGINALITY

I hereby declare that this thesis is my own work and that, to the best of my knowledge and belief, it reproduces no material previously published or written, nor material that has been accepted for the award of any other degree or diploma, except where due acknowledgement has been made in the text.

_____(Signed)

Zhang zhu (Name of student)

To my parents, Jian Jun Zhang and Chi Feng Liang

To my wife, Jian Xin Tang

To my son, Pok Fei Zhang

Abstract

Electromagnetic active suspension system is attracting more and more attention due to recent advances in motor design, power electronics and modern control method. Compared to the hydraulic active suspension system, it is more energy-efficient, and has a faster dynamic response. In this thesis, a novel configuration of linear switched reluctance actuator (LSRA) is proposed for the application in active suspension system. The robust construction, low manufacturing and maintenance cost, less thermal problem, good fault tolerance capability and high reliability in harsh environments make LSRA attractive alternative to permanent magnet actuator.

In order to determine the requirements on actuator design, the effects of suspension parameters on system characteristics are analyzed by the frequency response Bode plots method. A Linear Quadratic Regulator (LQR) controller is developed and simulated with the quarter-vehicle model to obtain the optimal force requirement on LSRA. By considering the requirements and constraints, a novel configuration of LSRA that comprises of four double-sided modules is proposed. The whole design procedure, ranging from the determination of basic actuator parameters to the calculation of flux linkage and force characteristics, is demonstrated in this thesis. The accuracy of the analytical design is then verified by the finite element method (FEM). Besides, the longitudinal and transversal end effects of double-sided LSRA are evaluated by analyzing the sensitivities of

translator position and excitation current.

To improve the performance of designed actuator, a multi-objective optimization method to obtain higher average force, reduced force ripple and higher force density is proposed in this thesis. Some practical constraints are taken into consideration in the optimization procedure. The effects of stator and translator pole width on the three optimization criteria and the actuator volume are analyzed. Based on the optimized specification, a prototype of the proposed LSRA was fabricated. The flux linkage and force characteristics were measured to verify the theoretical design.

Finally, an improved direct instantaneous force control (DIFC) scheme for four-quadrant operation of the proposed LSRA is developed. The controller incorporates adaptive force distribution function (FDF), instantaneous force estimation, hysteresis force controller and on-line determination of switching positions. By introducing the on-line estimated force of outgoing phase to FDF, the force demand of incoming phase is adaptively adjusted. Hence, the force ripple can be minimized over a wider range of switching positions. On the other hand, the operational efficiency is improved by on-line optimizing the switching positions according to the force demand. The simulation and experimental results demonstrate the effectiveness of the proposed control scheme.

Acknowledgements

I would like to express my sincere appreciation to my supervisors, Dr. Norbert C. Cheung and Professor K. W. E. Cheng, for all their invaluable guidance, support, and continuous encouragement during my research.

I would like to thank Dr. X. D. Xue. His academic guidance is extremely useful and beneficial. Special thanks go to my fellow colleagues and friends, Mr J. K. Lin, Mr. Y. J. Bao, Mr. D. H. Wang for all their technical support in this project. Also, many thanks go to Mr. Jones Chan and Mr. John Lam at the Power Electronic Research Center for the mechanical support in the test rig design and fabrication.

I gratefully acknowledge the financial support of Innovation and Technology Fund of Hong Kong SAR under the project code ITP/025/09AP.

Last but not the least; I would like to thank my parents, my wife and my family for their endless love, patience, care and devotion.

Table of contents

List of figures

List of tables

List of acronyms

ASS	Active Suspension System
LSRA	Linear Switched Reluctance Actuator
LQR	Linear Quadratic Regulator
FEA	Finite Element Analysis
FEM	Finite Element Method
MMF	Magntomotive Force
RSRM	Rotary Switched Reluctance Motor
DIFC	Direct Instantaneous Force Control
FDF	Force Distribution Function
LVDT	Linear Variable Differential Transformer

List of symbols

m_s	Sprung mass
m_{us}	Unsprung mass
x_s	Displacement of sprung mass
$\ddot{x}_s$	Acceleration of sprung mass
x_{us}	Displacement of sprung mass
$\ddot{x}_{us}$	Acceleration of unsprung mass
k_s	Spring stiffness
k_t	Tire stiffness
b_s	Damper coefficient
x_r	Road disturbance
u	Active force
d	System characteristic polynomial
f_{rs}	Body natural frequency
f_{ru}	Wheel natural frequency
$L_{\max}$	Maximum inductance
$L_{\min}$	Minimum inductance
w_{sp}	Stator pole width
w_{tp}	Translator pole width

w_{ts}	Translator pole slot
w_{ss}	Stator pole slot
τ_t	Stator pole pitch
τ_t	Translator pole pitch
l	Length of stator
l_s	Stator back iron thickness
h_s	Stator pole height
h_t	Translator pole height
w	Double-sided module width
D	Width of LSRA
w_c	Winding width
h_c	Winding height
A_c	Winding area
σ	Stroke
N_{ph}	Number of phase
N_{sp}	Number of stator pole
N_{tp}	Number of translator pole
g	Air gap
V	Voltage
i	Current
R	Resistance

L	Inductance
λ	Flux linkage
v	Movement speed
x	Translator position
e	EMF
P	Mechanical power
F_e	Force
F	Magntomotive force
W_e	Electrical energy
W_f	Magnetic field
W_m	Mechanical work
W_f'	Coenergy
H	Magnetic field intensity
B	Flux density
φ	Flux
A_j	Effective area
l_j	Effective length
F_{inst}	Instantaneous force
F_{ave}	Average force

Chapter 1

Introduction

1.1 Background

Vehicle systems have complex dynamics, due to road irregularities, breaking and cornering, changeable load effects, and other nonlinearities. The undesired oscillations may reduce the vehicle service life, lower the driving safety and riding comfort, and cause damages to cargo [1]. Therefore, suspension system is one of the most important components of any vehicle. The fundamental purpose of ground vehicle suspension system is to maintain continuous contact between the wheels and road surface, and to isolate the passengers or the cargo from the vibration induced by the road irregularities [2]. These two purposes are responsible for the road handling quality and the riding comfort, respectively. However, these goals are generally contradictory; it is difficult to achieve simultaneously best performance of riding comfort and road handling under all driving conditions [3].

There are three types of suspension systems applied in ground vehicle: passive, semi-active and active [4]. Each type appears in several structures and sizes according to their applications and intent. Passive suspension system is the most common type used in vehicle for its simplicity, reliability and low cost. It is composed of a spring and a damper with constant coefficients. Both coefficients are

pre-set at a fixed value to achieve the desired performance by making proper compromise between road handling and riding comfort. As a result, the suspension can only be tuned within a narrow range of performance. For example, race car is designed for better handing whose suspension is generally very stiff and sacrifices the ride quality, while the situation is completely different for a luxury car.

Semi-active suspension system is almost identical in mechanical structure to its passive counterpart, but the damper can be actively controlled through a low power signal. The damper force reacts accordingly to different damping coefficients. The operation range with good performance is thus beyond that of than the passive suspension. However, it can not provide an external force and can only control the energy dissipation of the system [5]. Furthermore, its performance will degrade with time because of the sealing problem.

Superior performance without compromise in road handling quality and ride comfort is obtained by active suspension system. External controllable force is introduced between the sprung mass and unsprung mass by means of several types of actuators. A spring is mounted in parallel with the actuator to shore the load. Active suspensions can enhance the dynamic characteristic of suspensions, and it can also achieve the adjustment of vehicle height. The relatively higher consumption of energy, implementation cost and size are its biggest disadvantages, which prevents its widespread use in common commercial cars.

1.2 Literature Review

1.2.1 Active suspension system

Although current active suspension system is complex and expensive, it shows significant improvements in riding comfort and road handling capability compared to passive and semi-active suspensions. Furthermore, with the developments in power electronics, control methods, sensor technologies and permanent magnet materials, the cost and size of active suspensions can be decreasing with improved performance.

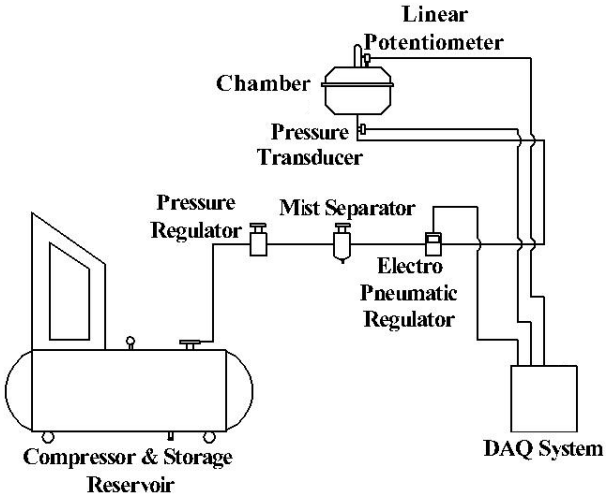

Fig. 1-1 A schematic of pneumatic system

The breakthrough in active suspension development is the implementation of an external force actuator between the vehicle body and the wheel. According to the type of actuator, active suspension system can be classified into three types: pneumatic, hydraulic and electromagnetic [6]. Pneumatic active suspension system, shown in Fig. 1-1, consists of a compressor and a storage reservoir which produce the compressed air. The compressed air is then transmitted to a chamber from the

reservoir, and its pressure is applied on the diaphragm in the chamber. The air pressure is converted into active force which is controlled by an electrical regulator, according to the pressure sensor mounted at the entry of the chamber [7]. Pneumatic actuators provide a high force density with a relatively low cost due to cheap power source and easy maintenance. However, this type of actuator has a complex structure, and it reacts at a relatively low bandwidth (around 1Hz), which is inefficient for continuous irregular road surface. Also, due to the air compressor and the complex friction in the chamber, pneumatic actuator tends to be highly nonlinear. This increases the complexity of control and degrades the overall performance.

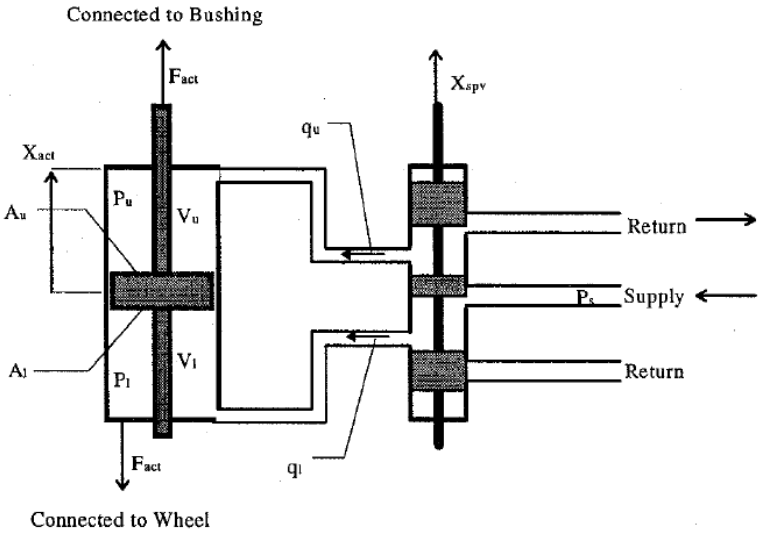

Fig. 1-2 A schematic of hydraulic system

Hydraulic active suspension systems have been extensively studied and developed [8-12]. Many car manufacturers, like Lotus, Nissan, and Citroën, have developed several prototypes or commercial products. Hydraulic actuator is always driven by the vehicle engine through a hydraulic pump. By adjusting the flow rate of the hydraulic fluid, the hydraulic pressure is controlled and converted to

active force in the piston, which is located between the vehicle body and the wheels, as shown in Fig. 1-2. Hydraulic suspension system has the advantages of high force density, high reliability, technical maturity and high availability. However, it suffers the same problem of large time constant as the pneumatic actuator. It is because of the large inertia of the fluid and the valve's motion in the piston. Moreover, the hydraulic actuator exhibits highly nonlinearity due to the dry friction. The continuous pressure requirement increases the energy consumption [13].

Comparing with passive suspension system, the high complexity and poor performance in the high frequency range limit the application of pneumatic and hydraulic active suspension systems. On the other hand, electromagnetic active suspension system has been studied and introduced in vehicles over the past decades [14-16]. Compared to hydraulic suspension systems, the electromagnetic actuator suspension system has a higher bandwidth (10-50Hz) and it is more environment-friendly due to the absence of acid fluid. Although the force density of electromagnetic actuator is lower than the hydraulic device, the system structure is simpler, due to reduced mechanical components and connection. Furthermore, the electromagnetic actuator is much more energy-efficient, because it does not need continuous power supply, and it can operate in both motoring and generating mode. The kinetic energy from road irregularities, which is dissipated as heat in the dampers, can be regenerated and stored in the battery or in the electromagnetic actuators [17-21]. Furthermore, the actuator can provides a damper force to absorb the road vibrations. Thus, electromagnetic active suspension system is attracting more and more attention. The developments in power electronics, permanent magnet

material and modern control method justify the implementation of electromagnetic actuator in vehicle suspension systems.

Fig. 1-3 The Bose® electromagnetic active suspension

Various technologies of rotary and linear machine have been proposed and employed in active suspension systems. Toyota proposed a rotary type active suspension that composed of DC brushless motor, reduction gear and torsion spring [22]. Michelin Corp. developed an active wheel integrated with active suspension. The active force is provided by an in-wheel rotary motor [23]. However, the desired motion of suspension system is linear; in both cases the electromagnetic force applied by rotary motor has to be converted to linear motion by mechanical transmission devices like gear and lead screw. The friction and transmission result in energy loss and reduced accuracy. The acceleration and reliability of the suspension system are also affected. Therefore, direct drive by linear electromagnetic actuator would be a better choice for suspension application. Bose Corp. is the most representative corporation in developing this kind of linear electromagnetic actuator.

The researchers had developed the first prototype in 1989 [24]. Since then, the performance of their motor has been improved in both the size and energy-consumption. Fig. 1-3 shows the recent Bose® suspension front module. More linear electromagnetic actuators were proposed in the past decade. Ismenio, et al. constructed a cylindrical linear actuator with axially magnetized NdFeB [25]. The prototype with their dimensions can fit in the available space of commercial vehicles, but it is larger than the equivalent hydraulic actuator. Bart, et al. proposed a slot-less brushless tubular permanent magnetic actuator [26]. Both interior and exterior-magnet topologies are investigated for three different magnetization patterns in his research, as shown in Fig. 1-4. Similar active suspensions with tubular linear permanent magnetic actuator were proposed in [27]. The mover is composed of a series of cylindrical permanent magnets and the coils are placed at stator side. However, the force and dimension of the prototype are scaled down for laboratory test. To reduce the production cost, another tubular permanent magnets motor with solid stator core is proposed in [28].

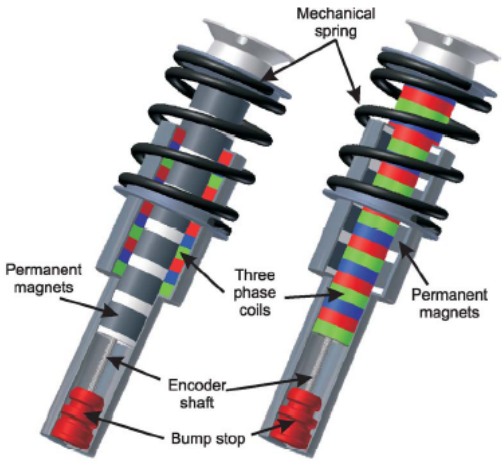

Fig. 1-4 Suspension struts with permanent magnets

It can be observed that most of linear electromagnetic actuators consist of NdFeB permanent magnet. It justifies the development of permanent magnetic materials with high-energy density in the recent years. Therefore, smaller and lighter actuators are achieved at the same power and they become more suitable for suspension application. However, the NdFeB magnet is expensive which make this kind of suspension more expensive than other suspension systems. Furthermore, there is a big drawback in NdFeB magnet. It would lose its magnetization characteristics at around 150℃. The suspension systems are usually working under tough environment. Thus, the temperature rise in the suspension has to be controlled within the acceptable range by sacrificing the performance.

1.2.2 Linear switched reluctance actuator

Switched reluctance motor (SRM) is an electric motor with doubly salient and singly excited structure, which operates according to the minimum reluctance principle. The rotor tries to align its poles with the position with minimum reluctance for the magnetic circuit. By exciting the windings sequentially with the position, full rotation of SRM is achieved. There is no need for permanent magnets, and the coils are concentrated rather than distributed.

Linear switched reluctance actuator (LSRA) is based on the rotary switched reluctance motor (RSRM) principle and it retains the merits of its counterparts. The robust construction, low manufacture and maintenance cost, less thermal problem, good fault tolerance capability and high reliability in harsh environments make LSRA an attractive alternatives in industrial applications, especially for use in linear

motions. Compared with the RSRM, LSRA has a quicker response, higher accuracy and less energy consumption due to the absence of rotary-to-linear mechanical transformation. Up to now, various configurations of LSRA have been introduced and studied. A standard design procedure by converting the specifications of RSRM for single-sided LSRA is proposed by B. S. Lee [29]. A novel configuration of LSRA for high precision position control is proposed in [30]. Deshpande, et al. proposed a high force density LSRA with the configuration of double-side, double-translator [31, 32]. Another high force density LSRA with segmented translator and full-pitch-winding stator was presented in [33]. Liu, et al. designed a micro LSRA for high precision application in semiconductor fabrication [34]. Lim, et al. constructed a new configuration of double-sided LSRA for the propulsion of a ship elevator [35, 36].

LSRAs not only inherit the merits of RSRMs, but also retain the drawbacks of inherent nonlinearity and force ripple problem. The problem is severer and even intolerable in direct-driven servo motion system. Two major approaches were applied to reduce the force ripple: geometry design optimization and control technologies improvement. The geometry optimization is realized by adjusting the shape or width of stator and translator poles. This is considered to be the most effective way to alleviate the inherent problem. A great variety of methods were proposed to optimize the geometry of RSRM, such as progressive quadratic response surface method [37], genetic algorithm [38, 39], fuzzy logic algorithm [40, 41], Neural-network method [42] and deterministic methods [43]. Although plenty of articles have been published on the geometric optimization of RSRM, there is little

literature related to the LSRA. The control method is optimized by adjusting the control parameters, such as turn-on/off positions, and excitation current [44-49]. Instantaneous force control is another practical way to minimize the force ripple of LSRA. The instantaneous force is on-line estimated from the measurable quantities like translator position and phase current, and then adapted directly from a force controller. The faster response and better elimination of force ripple are achieved without the indirect modulation of phase current [50]. A typical direct instantaneous torque control of RSRM was proposed by Inderka [51]. The instantaneous torque is estimated by a lookup table from measuring phase current and flux linkage, and regulated by a hysteresis torque controller. Another direct instantaneous torque control using a novel 4-level converter is presented in [52]. Fast magnetization and demagnetization is achieved to improve the dynamic performance and efficiency. In [53], the direct instantaneous torque control is discussed for four-quadrant operation. A novel switching scheme is developed for both operation modes from a state chart in this paper. In [54], an iterative learning control based direct instantaneous torque controller is proposed, and sliding mode control is applied to improve the performance during transient periods.

1.3 Objectives and Structure of this thesis

1.3.1 Objectives

Although LSRAs have so many advantages over other motors, there is no previous work or researches related to the application of electromagnetic active suspension system. Therefore, the primary objective of this research is to design an

LSRA based on the requirements and implement in the active suspension system. Since the force ripple will degrade the performance of LSRA, the second objective is to minimize the force ripple at both design and control stage.

1.3.2 Structure

The structure of this thesis is outlined as following:

Chapter 1 gives some background on the vehicle suspension system. In this chapter the merits and drawbacks of different kinds of suspension system are discussed and the methods for force ripple minimization of LSRA are introduced. The objectives and structures of this research are summarized at the end of this chapter.

In Chapter 2, quarter-car model of suspension system is described and the effects of suspension parameters, such as spring stiffness, damping coefficient, sprung and unsprung mass are discussed. Based on the analysis, the design aspects for the LSRA are identified in this chapter.

Chapter 3 introduces the basic operation principle of the LSRA and details the preliminary design procedure. In this chapter, the configuration of the LSRA for the active suspension system is proposed and its magnetic circuit analysis is conducted for the preparation of the preliminary design.

In order to improve the accuracy of FEA, the longitudinal and transversal end effects are discussed in Chapter 4. The FEA results are presented to verify the preliminary design.

In Chapter 5, a multi-objective optimization for the proposed LSRA is conducted

to achieve higher average force, reduced force ripple and higher average force per core volume. The effects of stator pole and translator pole width are discussed in this chapter.

Chapter 6 introduces a direct instantaneous force control scheme for LSRA, which incorporates instantaneous force estimation, force distribution function, hysteresis force control and on-line determination of switching position.

In the last chapter, the major contributions and achievements of this thesis are summarized, and some suggestions for further research on the proposed actuator are concluded.

Chapter 2

Design Aspects for the Linear Switched Reluctance Actuator

Vehicle system is highly dynamic and nonlinear that exhibits vibration under external road irregularities. The performance of road handling and riding comfort is largely dependent on the feature of vehicle suspension system. In order to analyze the system and identify the suspension parameters, three vehicle models have been developed: quarter-vehicle [55], half-vehicle [56] and full-vehicle model [57].

Generally, full-vehicle model is preferred in the analysis of suspension dynamics, because the seven degree-of-freedom model can reflect more realistic dynamic characteristics by evaluating the vehicle roll and pitch motion, vertical displacement of vehicle body and four wheels [11, 58, 59]. However, the full-vehicle model is very complex when the four wheel suspension models are coupled together. Quarter-vehicle model is more extensively used to analyze and understand the influence of suspension parameters. It has simpler structure with two degrees of freedom in the vertical direction only. This structure can be easily applied for the design and control of suspension systems. Although roll and pitch behaviors are eliminated in this kind of model, they can be simulated as external disturbance

acting on the vehicle body [60]. Hence, the quarter-vehicle model is selected in this thesis for the analysis. To identify the suspension parameters and optimize the design of the LSRA based active suspension, the quarter-vehicle model is analyzed by frequency response with the variations of spring stiffness, damping coefficient, unsprung and sprung mass through the Bode-plot analysis.

2.1Quarter-vehicle Model Description

2.1.1 The Passive Suspension

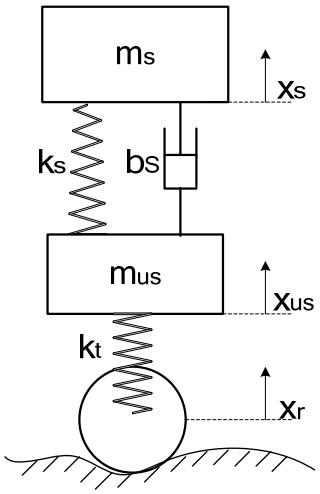

Fig. 2-1 Quarter-vehicle model of passive suspension

The quarter-vehicle model with conventional passive suspension, as shown in Fig. 2-1, is a lumped element model with two degrees of freedom. It is modeled by a linear spring and damper. The spring is considered to support the sprung mass, which is valued at one fourth of the total vehicle body mass. The damper is used to dissipate the energy generated by the vibration. The tire is modeled as a spring of high stiffness without damping, which acting on both unsprung and sprung mass.

The dynamic motion can be represented by the following equations:

$$m_s\ddot{x}_s + k_s(x_s - x_{us}) + b_s(\dot{x}_s - \dot{x}_{us}) = 0 \qquad (2\text{-}1)$$

$$m_{us}\ddot{x}_{us} - k_s(x_s - x_{us}) - b_s(\dot{x}_s - \dot{x}_{us}) + k_t(x_{us} - x_r) = 0 \qquad (2\text{-}2)$$

where m_s and m_{us} are the sprung mass and unsprung mass respectively, x_s and x_{us} are the displacements of respective masses respectively, k_s and k_t are the spring stiffness, b_s is the damper coefficient and x_r represents the road disturbance.

2.1.2 The Active Suspension

The quarter-vehicle models of the hydraulic and electromagnetic active suspension system are shown in Fig. 2-2 (a) and (b), respectively. The hydraulic active suspension is modeled by a conventional passive suspension with an addition of active actuator between the sprung and unsprung masses. In the electromagnetic suspension system the passive damper is replaced by an active actuator. The damping effect of tire is negligible in the active suspension model.

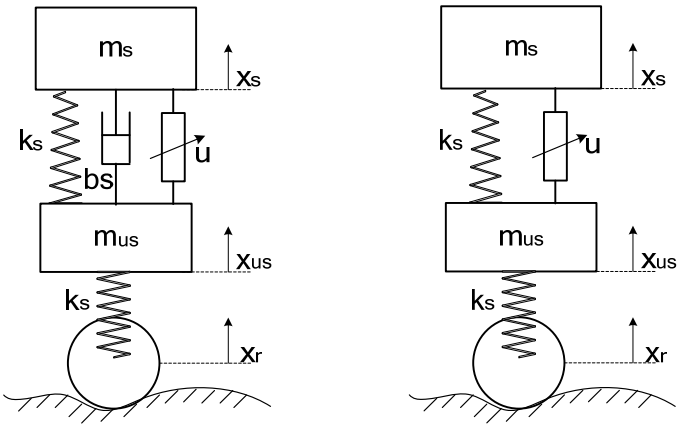

(a) Hydraulic (b) Electromagnetic

Fig 2-2 Quarter-vehicle model of active suspension

The dynamic equations of active suspensions are:

$$m_s\ddot{x}_s + k_s(x_s - x_{us}) + b_s(\dot{x}_s - \dot{x}_{us}) = u \tag{2-3}$$

$$m_{us}\ddot{x}_{us} - k_s(x_s - x_{us}) - b_s(\dot{x}_s - \dot{x}_{us}) + k_t(x_{us} - x_r) = -u \tag{2-4}$$

where u is the active force generated by actuator. The damping coefficient is set to zero when analyzing the electromagnetic suspension.

Considering the following state variables

$x_1 = x_s - x_{us}$ Suspension deflection

$x_2 = \dot{x}_s$ Sprung mass velocity

$x_3 = x_{us} - x_r$ Tire deflection

$x_4 = \dot{x}_{us}$ Unsprung mass velocity

The state space equation can be obtained as:

$$\dot{X} = AX + Bu + L\dot{x}_r \tag{2-5}$$

where $A = \begin{bmatrix} 0 & 1 & 0 & -1 \\ -\frac{k_s}{m_s} & -\frac{b_s}{m_s} & 0 & \frac{b_s}{m_s} \\ 0 & 0 & 0 & 1 \\ \frac{k_s}{m_{us}} & \frac{b_s}{m_{us}} & -\frac{k_t}{m_{us}} & -\frac{b_s}{m_{us}} \end{bmatrix}$

$$B = \begin{bmatrix} 0 & \frac{1}{m_s} & 0 & -\frac{1}{m_{us}} \end{bmatrix}^T$$

$$L = \begin{bmatrix} 0 & 0 & -1 & 0 \end{bmatrix}^T$$

2.2Effect analysis of suspension parameters

To investigate the influence of suspension parameters on system characteristics, the frequency response of the quarter-vehicle model is analyzed by varying the spring stiffness, damping coefficient, sprung and unsprung mass. The sprung mass acceleration, suspension deflection and tire deflection are selected as the criteria to evaluate the suspension performance, and the tire's vertical velocity is considered as external disturbance.

From the dynamic equations, the open loop transfer functions are obtained. The effect of each system parameter is investigated by referring to the bode plot. The transfer function from road vertical velocity to sprung mass acceleration, suspension deflection and tire deflection are respectively:

$$\frac{\ddot{x}_s}{\dot{x}_r} = \frac{k_t s(b_s s + k_s)}{d} \tag{2-6}$$

$$\frac{x_s - x_{us}}{\dot{x}_r} = -\frac{k_t m_s s}{d} \tag{2-7}$$

$$\frac{x_{us} - x_r}{\dot{x}_r} = -\frac{m_{us} m_s s^3 + (m_{us} + m_s) b_s s^2 + (m_{us} + m_s) k_s s}{d} \tag{2-8}$$

where *d* is the system characteristic polynomial.

$$d = m_{us} m_s s^4 + (m_{us} + m_s) b_s s^3 + [(m_{us} + m_s) k_s + m_s k_t] s^2 + b_s k_t s + k_s k_t \tag{2-9}$$

2.2.1 Effects of spring stiffness

The effect of spring stiffness can be examined by comparing five curves with increasing stiffness, as is shown in Fig. 2-3. It can be observed that there exist two peaks for each curve in each sub-Bode-plot of Fig. 2-3. The first peak occurs at a lower frequency, which is called as vehicle body natural frequency, and the other peak occurs at vehicle wheel natural frequency. The exact value of two natural frequencies can be obtained by solving the system characteristic polynomial.

$$f_{rs} = \frac{1}{2\pi}\sqrt{\frac{k_s}{m_s}} \tag{2-10}$$

$$f_{ru} = \frac{1}{2\pi}\sqrt{\frac{k_t}{m_{us}}} \tag{2-11}$$

Fig. 2-3(a) shows the frequency response of sprung mass acceleration to vertical wheel velocity. It can be seen that the isolation of vibration is increasingly improved as the spring stiffness is decreased. However, the performance of suspension deflection at low frequencies become more severe, which results in larger suspension stroke, as shown in Fig. 2-3(b). The tire deflection is reduced with lower spring stiffness around the body natural frequency. It can be observed that the spring stiffness has little influence on suspension performance beyond the wheel natural frequency.

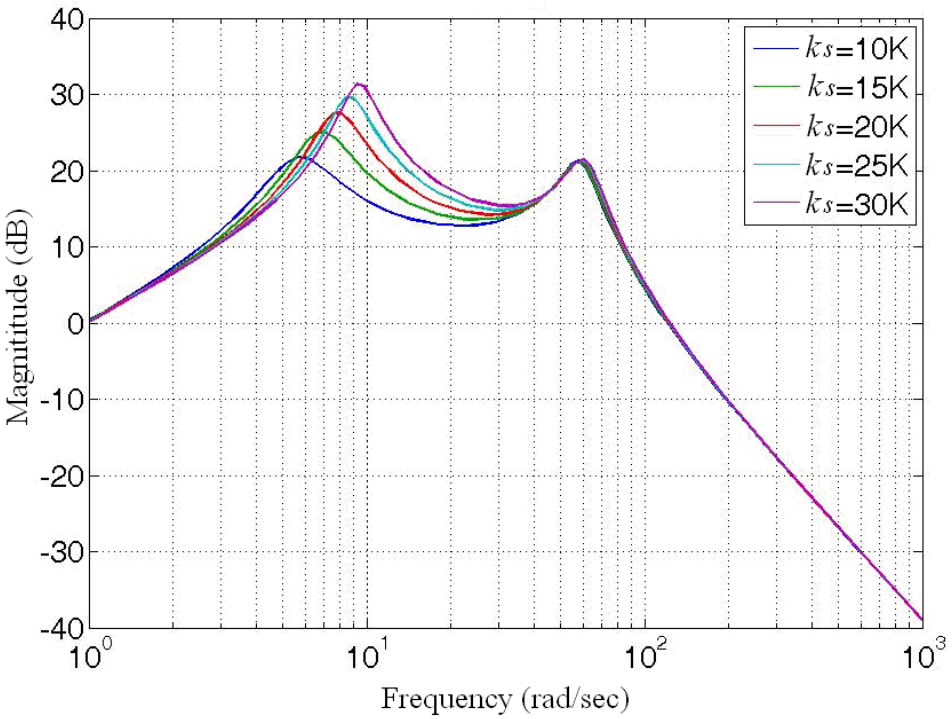

(a) Acceleration response with varying spring stiffness

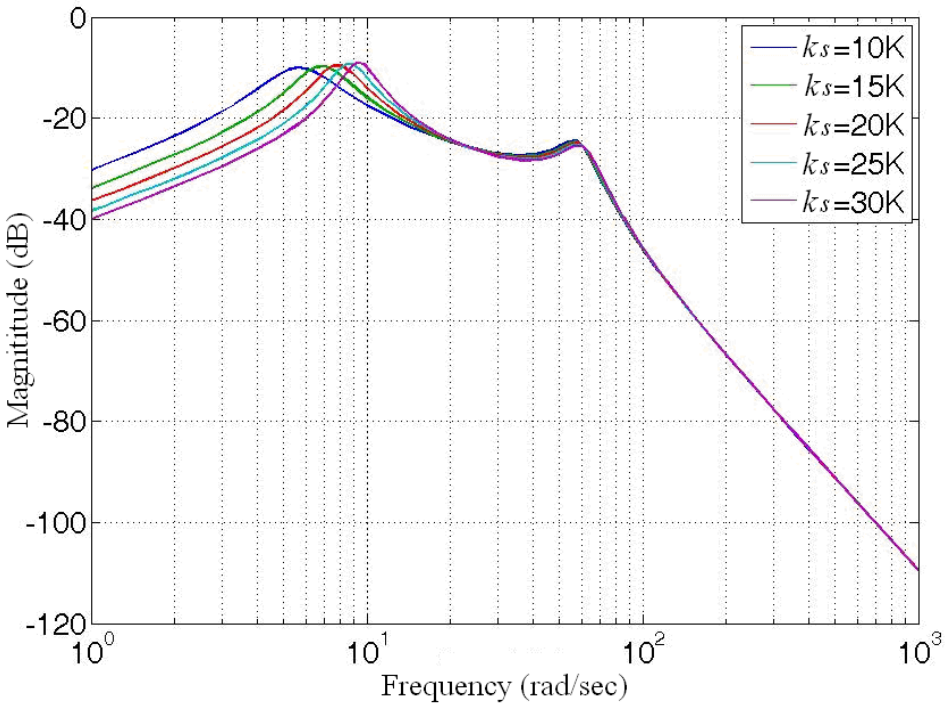

(b) Suspension deflection response with varying spring stiffness

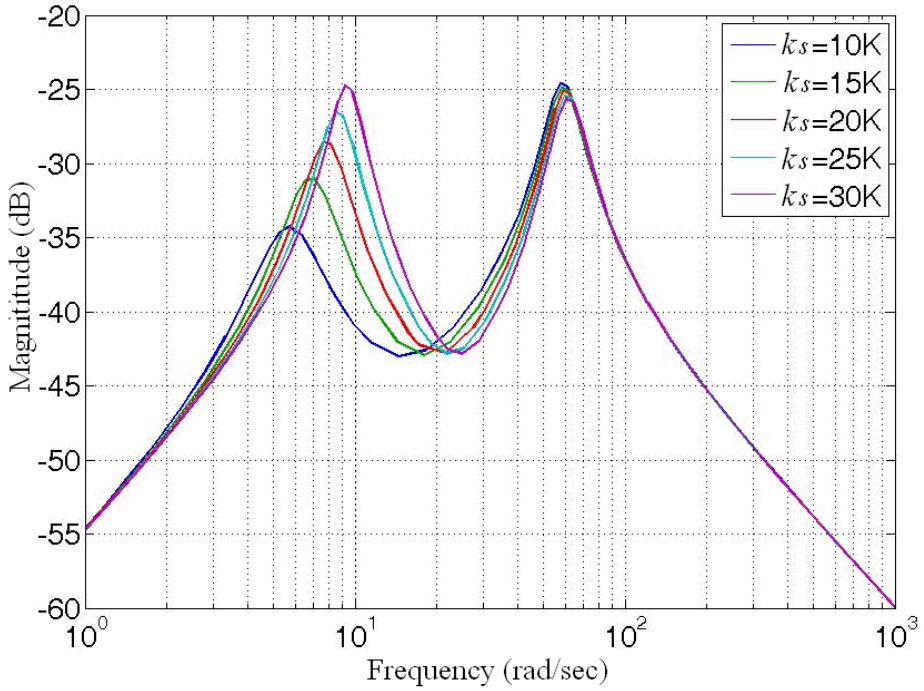

(c) Tire deflection response with varying spring stiffness

Fig. 2-3 Effect of spring stiffness

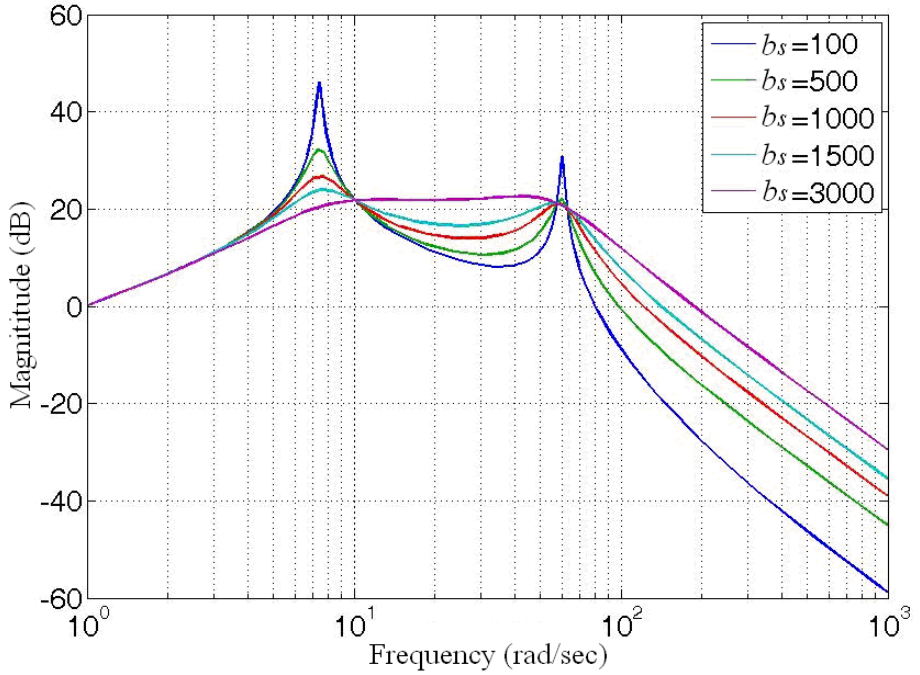

(a) Acceleration response with varying damping coefficient

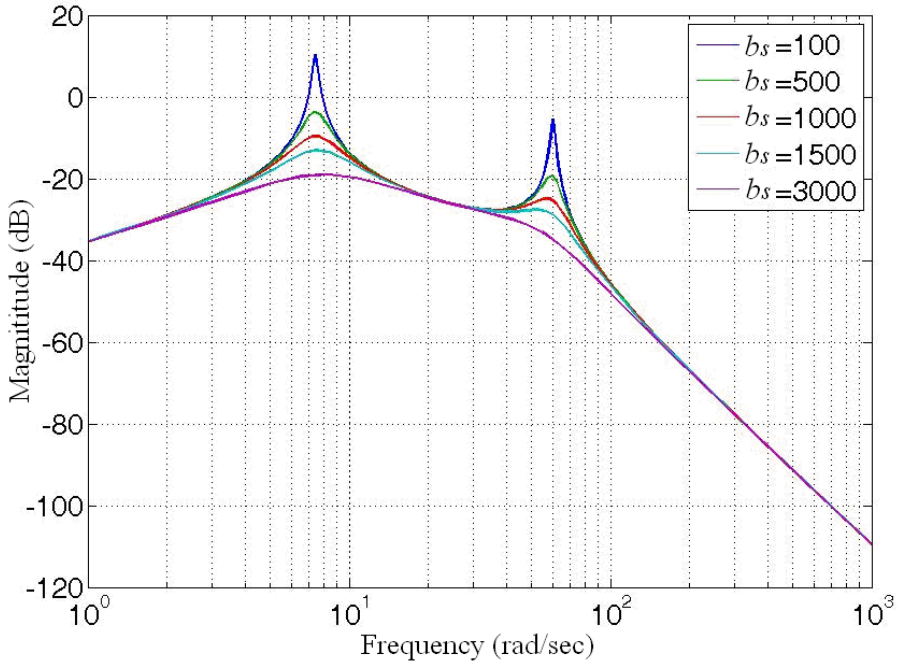

(b) Suspension deflection response with varying damping coefficient

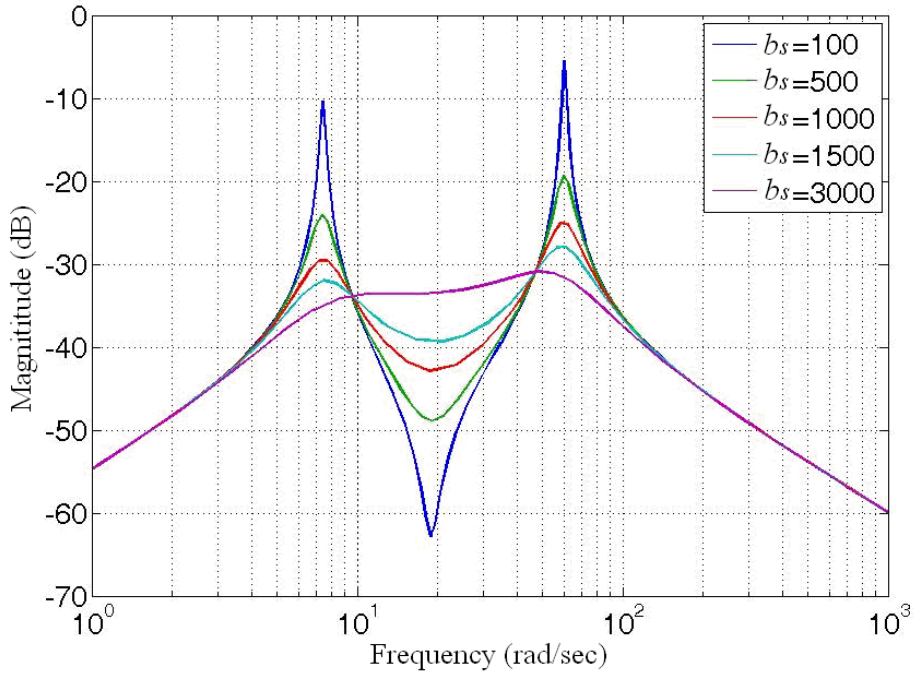

(c) Tire deflection response with varying damping coefficient

Fig. 2-4 Effect of damping coefficient

2.2.2 Effects of damping coefficient

To investigate the effect of damper, the resultant Bode plots for five damping coefficients are demonstrated in Fig. 2-4. It can be seen from the Fig. 2-4 (a), as the suspension damping coefficient decreases, the sprung mass acceleration response will deteriorate at low frequencies, and then improve beyond the body natural frequencies, except for the frequencies around wheel natural frequency. The suspension deflection is improved obviously around two natural frequencies with increased damping coefficient, but it has little influence at other frequencies, as is shown in Fig. 2-4 (b). The effect on tire deflection is illustrated in Fig. 2-4 (c). Reduced tire deflection is obtained between the two natural frequencies with smaller damper. However, the tire deflection responses around two natural frequencies become worse.

2.2.3 Invariant property of active suspension

Considering the quarter-vehicle model of active suspensions, it can be observed that the effects of spring, damper and active force on sprung mass and unsprung mass are equal, but at opposite directions. By adding the two dynamic equations (2-3) and (2-4), the following can be obtained:

$$m_s \ddot{x}_s + m_{us} \ddot{x}_{us} = k_t (x_r - x_{us}) \tag{2-12}$$

The relationship between the transfer function of sprung mass acceleration and suspension deflection to wheel vertical velocity is then derived from equation (2-12), and it is expressed as:

$$\frac{\ddot{x}_s}{\dot{x}_r} = -\frac{m_{us}s^2 + k_t}{m_s s}\frac{x_s - x_{us}}{\dot{x}_r} + \frac{k_t}{m_s s} \tag{2-13}$$

From equation (2-13), it can be observed that the transfer function of sprung mass acceleration is only dependent on the tire stiffness, sprung and unsprung mass at the frequency defined by equation (2-14), and rewritten as equation (2-15).

$$s = \sqrt{\frac{k_t}{m_{us}}} \tag{2-14}$$

$$\frac{\ddot{x}_s}{\dot{x}_r} = \frac{\sqrt{k_t m_{us}}}{m_s} \tag{2-15}$$

Therefore, at this specific frequency, the transfer function of sprung mass acceleration is irrelevant to the active force, which indicates that the response is invariant no matter what kind of control method is applied.

2.2.4 Effects of sprung and unsprung mass

Through the discussion mentioned above, it can be concluded that the sprung and unsprung mass have a significant impact on the characteristic of suspension system. The suspension natural frequencies and the invariant frequency of active suspension are varied with both of its masses. The ratio between sprung and unsprung mass is considered as one of the most important aspects that influence road handling and riding performance.

The unsprung mass is comprised of the mass of wheels, the brake components, parts of the suspension system and other components that are connected directly to the wheels. The rest of the mass that is supported by the suspension is the sprung mass. It includes the mass of the engine, transmission, passenger cabin and various mechanical and electrical components [61]. Hence, the road irregularities are directly reflected by the vibration of unsprung mass and generate significant vertical acceleration to unsprung mass. Therefore, more kinetic energy is transmitted from the road with greater unsprung mass. The resultant vertical force will degrade the contact of wheel and road surface, and deteriorate the road handling capability and driving safety. On the other hand, the sprung mass provides the spring a compressive force to keep good contact between the wheel and road. The contact pressure is enhanced with heavier sprung mass.

The effect of both masses on suspension characteristic can also be investigated by frequency response analysis. From the bode plots in Fig. 2-5, with five increasing sprung masses and in Fig. 2-6 with five increasing unsprung masses, it can be observed that the isolation of vibration is deteriorated with the decrease of sprung mass and with the increase of unsprung mass. On the other hand, the tire deflection is significantly reduced by decreasing the unsprung mass. The results obtained by the bode plots are consistent with the above analysis conclusion. Therefore, higher ratio of sprung mass to unsprung mass is preferred in suspension design.

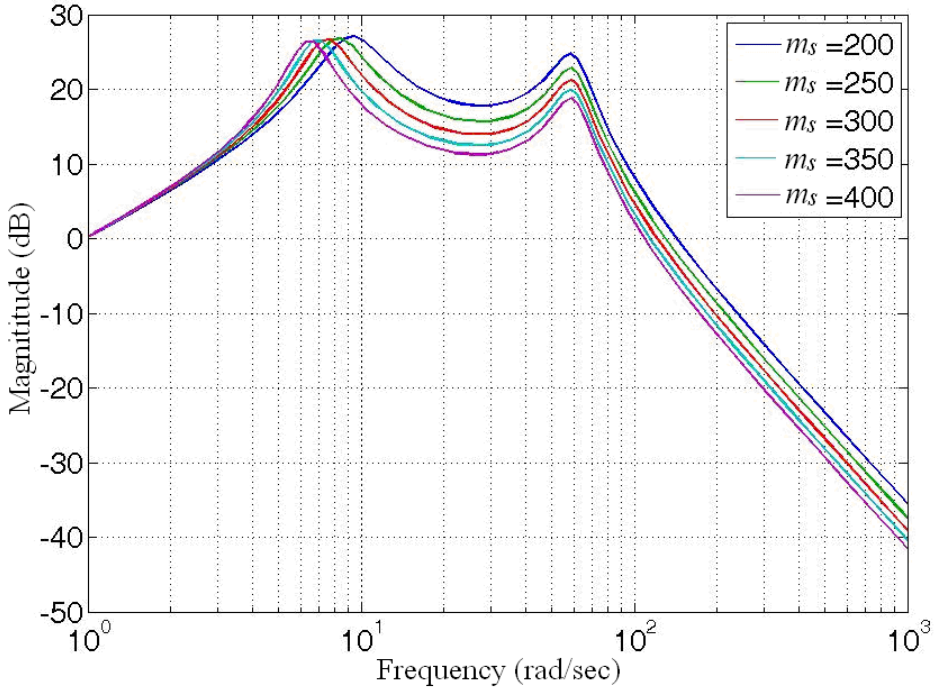

(a) Acceleration response with varying sprung mass

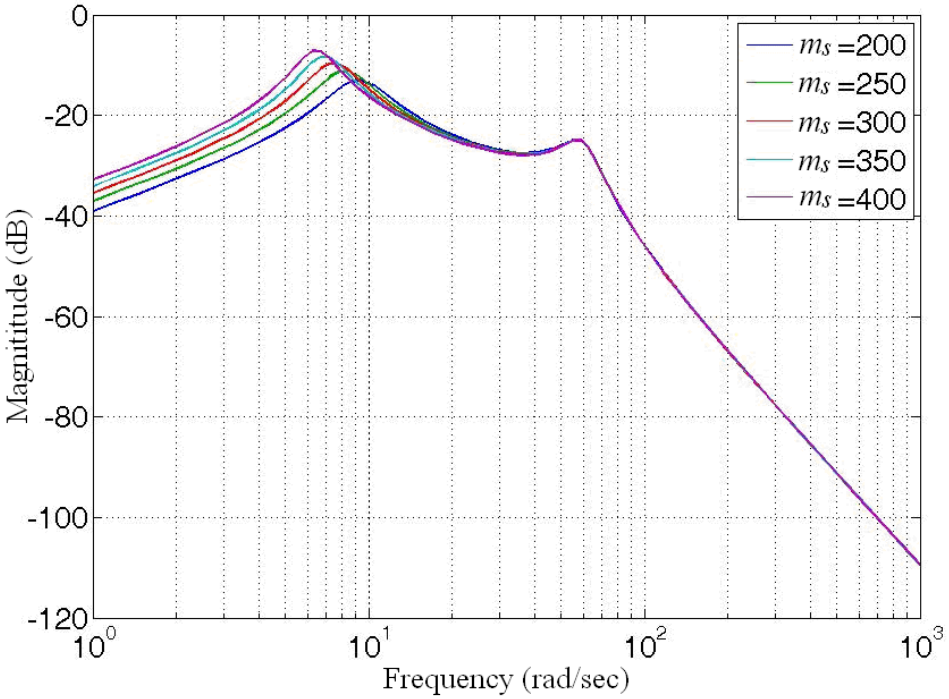

(b) Suspension deflection response with varying sprung mass

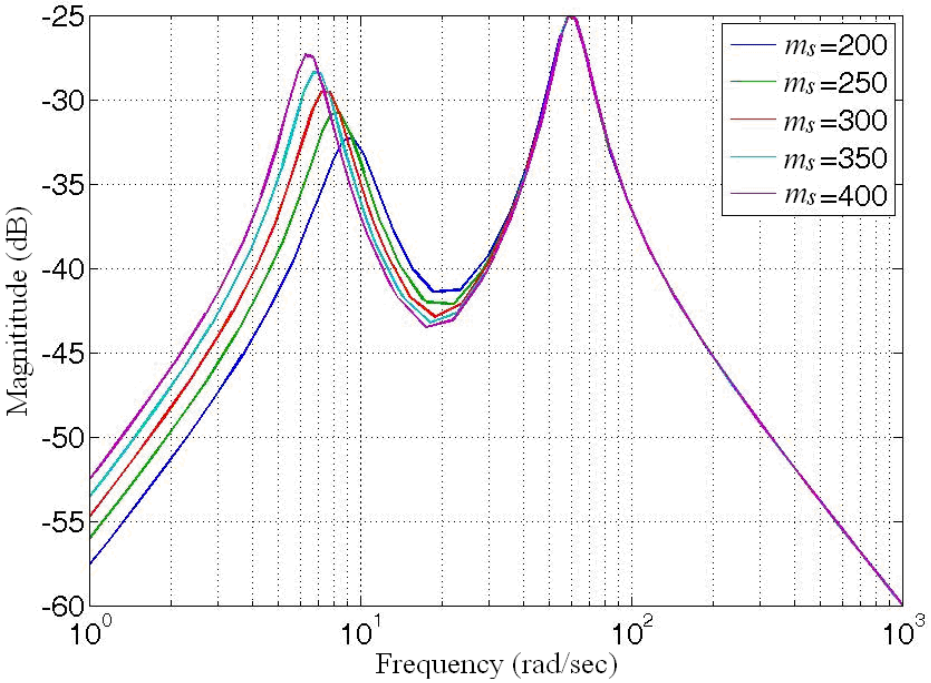

(c) Tire deflection response with varying sprung mass

Fig. 2-5 Effect of sprung mass

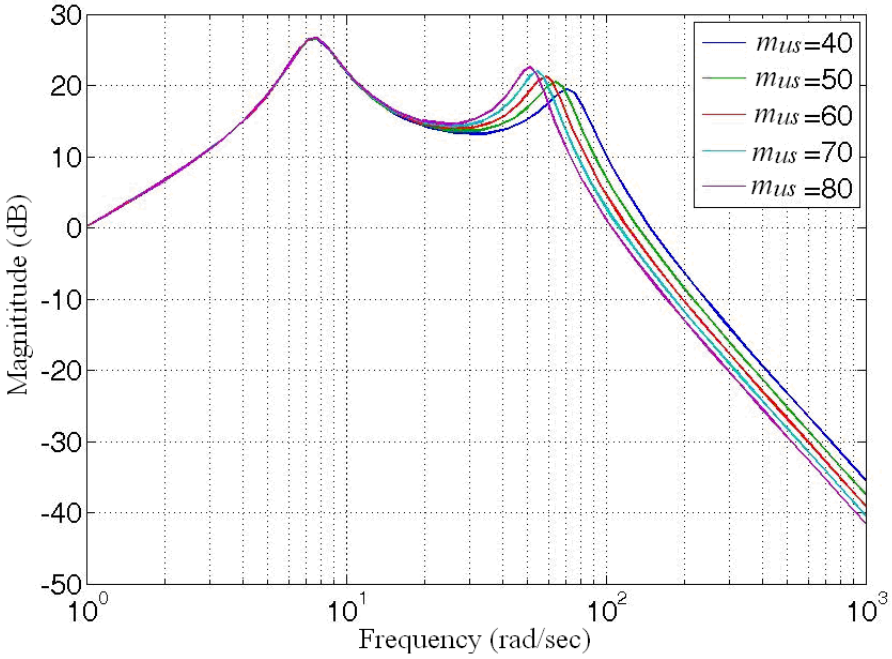

(a) Acceleration response with varying unsprung mass

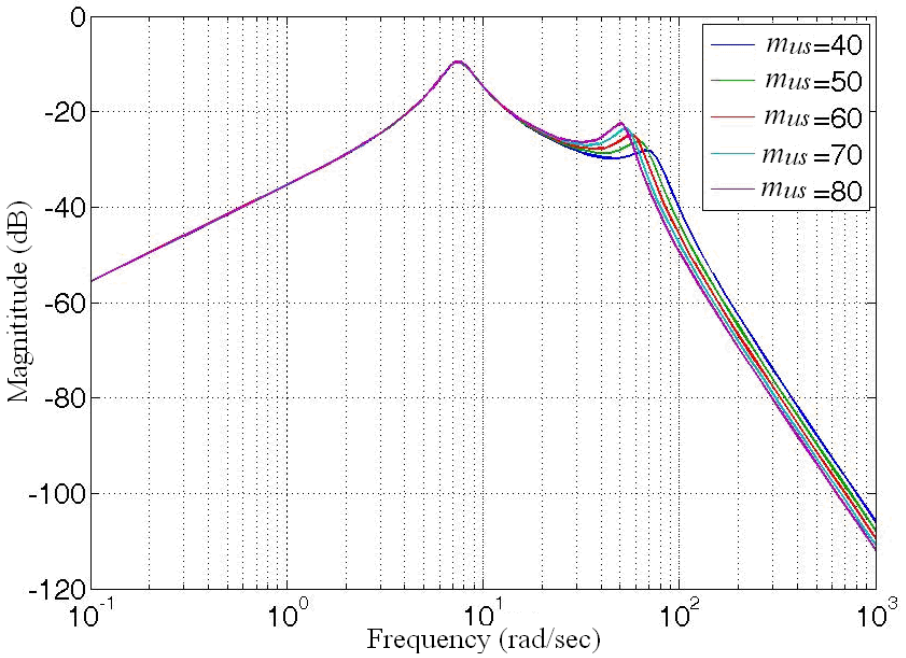

(b) Suspension deflection response with varying unsprung mass

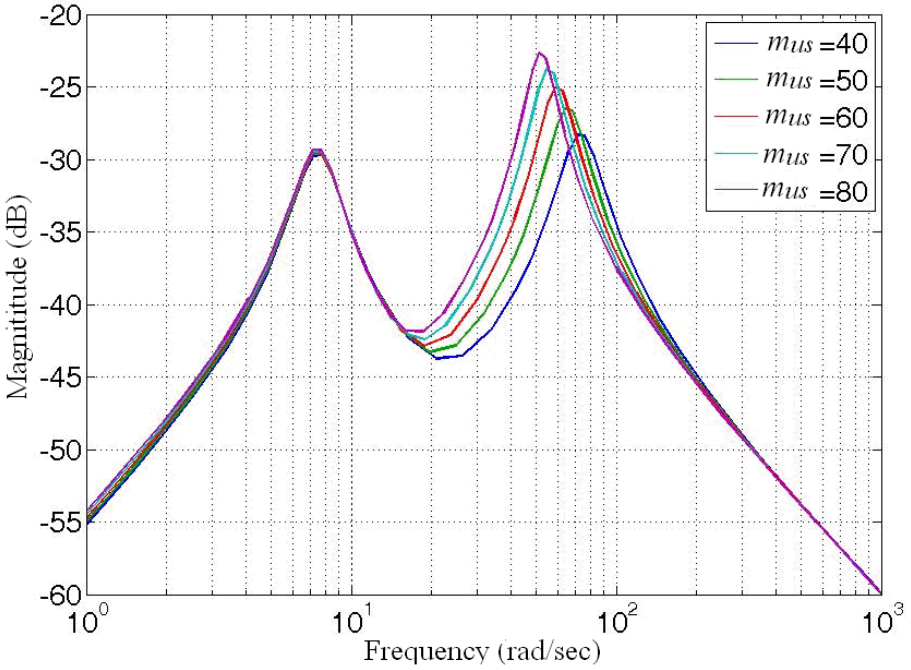

(c) Tire deflection response with varying unsprung mass

Fig. 2-6 Effect of unsprung mass

2.3Design Aspects of the Linear Switched Reluctance Actuator

Before the design of LSRA for active suspension, there are some more parameters need to be identified, such as peak force, continuous force and maximum stroke length. Each parameter has significant influence on the performance of active suspension. Numerical simulations based on the quarter-vehicle model were carried out to obtain the parameters on LSRA design.

2.3.1 Requirements on force and stroke length

The required active force and stroke length are mainly dependent on the vehicle body weight, road irregularities and the expected performance. The vibration magnitude of sprung mass should be controlled within an acceptable range for passenger comfort. Approximate indications that human react to the magnitudes of vibration are presented in ISO2631. The value varies with the duration and the type of activities under vibration by passengers. Moreover, sufficient damping force should be exerted by the actuator when the system is working in regenerative mode.

Maximum stroke is the available travel distance between the sprung and unsprung mass. The value is selected not only to meet the requirements for roll and pitch behavior, but also to absorb the road irregularities. Movement that exceeds the maximum stroke length can lead to serious damage to the actuator and can cause extreme uncomfortable ride to passengers; thus longer stroke is preferred to ensure the function and safety of the suspension. However, too much margin in stroke will extend the length and increase the weight and size of the actuator.

In order to identify the parameters for the design of LSRA in active suspension

system, a LQR optimal controller is conducted and simulated with quarter-vehicle model to obtain the required force. The LQR is a full state feedback controller with an aim to minimize a quadratic cost function [62]. The controller block diagram is shown in Fig. 2-7.

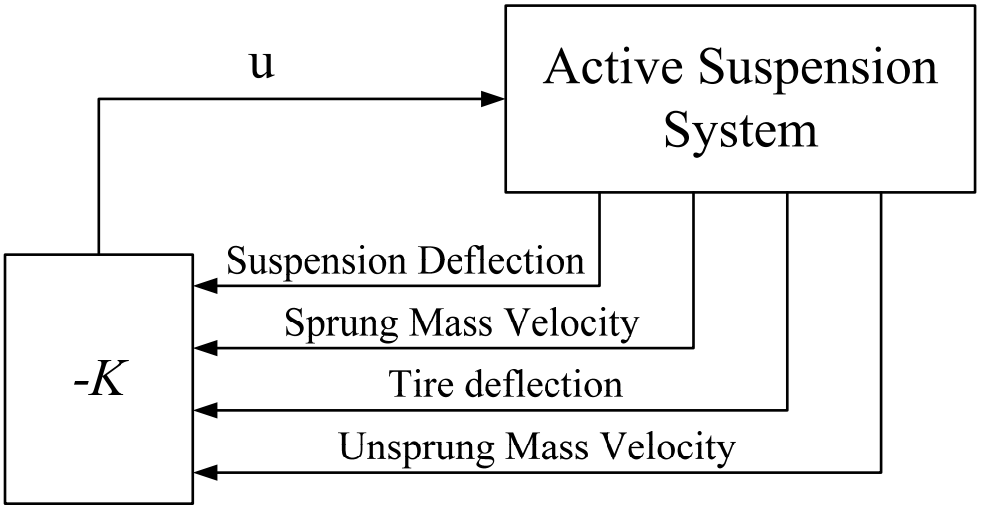

Fig. 2-7 Block diagram of LQR controller

Considering the system state space model in equation (2-5), the quadratic cost function can be defined as:

$$\min J = \frac{1}{2}\int_0^\infty \left(x^T(t)Qx(t) + u^T(t)Ru(t) \right) dt \tag{2-16}$$

then the feedback control that minimizes the cost is

$$u = -KX \tag{2-17}$$

where K is given by

$$K = R^{-1}B^T P(t) \tag{2-18}$$

and $P(t)$ is found by solving the continuous time Riccati differential equation

$$A^T P(t) + P(t)A - P(t)BR^{-1}B^T P(t) + Q = -\dot{P}(t) \tag{2-19}$$

TABLE 2-1
SPECIFICATION OF THE SUSPENSION SYSTEM

Parameters	Value
Sprung mass	300 kg
Unsprung mass	60 kg
Spring Stiffness	18600 N/m
Damping coefficient	1000 N/m/s
Tire stiffness	180000 N/m

Simulations are performed in the Matlab/Simulink environment with the system parameters shown in Table 2-1, which is based on the actual vehicle specification. Responses of sprung mass acceleration to 10 rad/s and 100 rad/s sinuous disturbance are demonstrated in Fig. 2-8 and Fig. 2-9, respectively. Both frequencies of disturbance are approximate to the suspension natural frequencies, which are the most severe working point of active suspension system. It can be observed that the acceleration of sprung mass is reduced significantly to the acceptable range for comfort. The required active force for expected performance is then obtained for the actuator design.

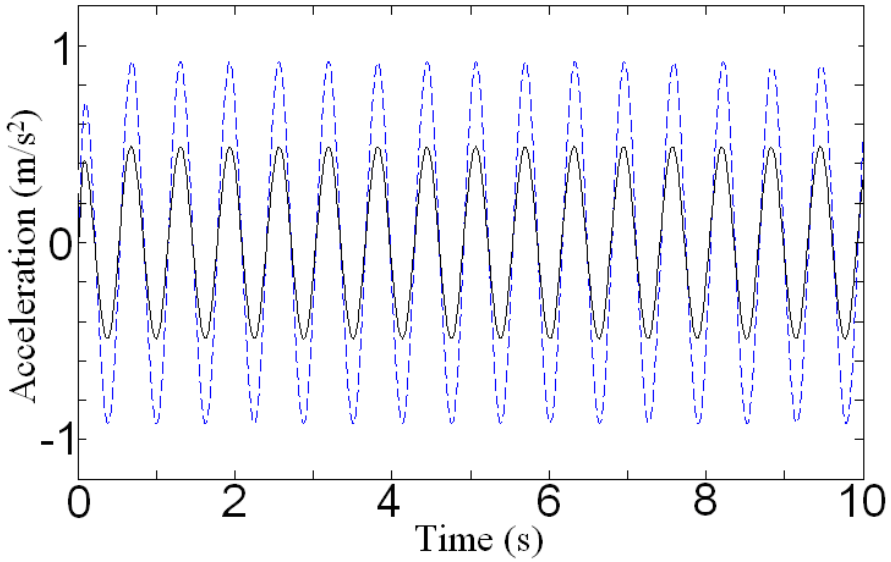

(a) Sprung mass acceleration

(Dashed line: passive, solid line: Active)

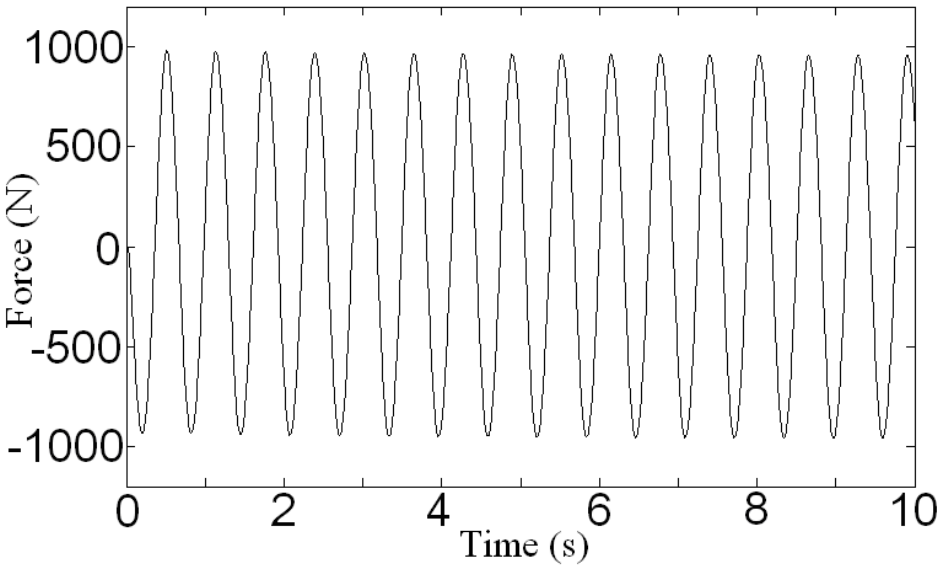

(b) Active force

Fig. 2-8 System responses at 10rad/s disturbance

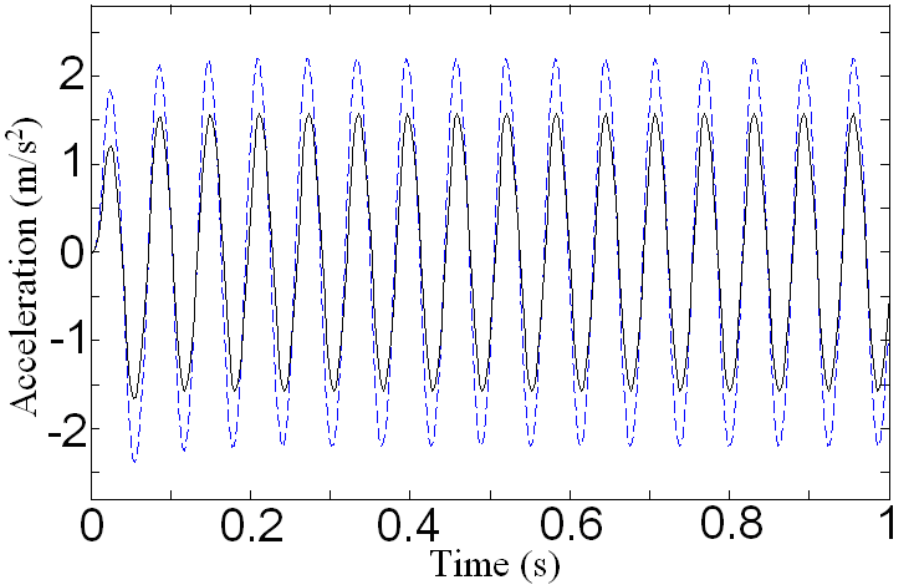

(a) Sprung mass acceleration

(Dashed line: passive, solid line: Active)

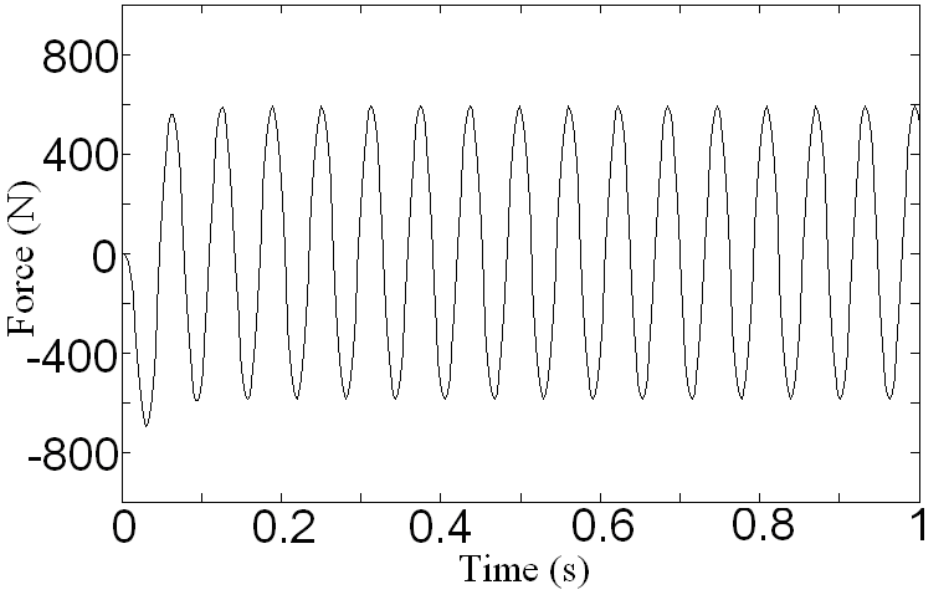

(b) Active force

Fig. 2-9 System responses at 100rad/s disturbance

2.3.2 Volume and weight constraints

The passive suspension system is located in a compact space between the vehicle body and four wheels. Without major modification to the vehicle mechanical structure, the room available for the active suspension strut is limited. The maximum constraint on the size and length of actuator can not be defined exactly for its dependence on the vehicle grade and specific design. Take Benz C-class for example, the maximum length for the suspension strut should be less than 700mm according to the vehicle dimension. After extensive investigation of vehicle suspension, the volume constraint on the LSRA is identified as $300\text{mm} \times 300\text{mm} \times 600\text{mm}$. The additional weight of active suspension system will increase the weight of total vehicle, and hence the fuel consumption. Therefore, the actuator should be designed as light as possible by increasing the force density of the LSRA.

2.4 Summary

In this chapter, the quarter-car model is selected to analyze the parameters of the active suspension system. The effects of spring stiffness, damping coefficient, sprung mass and unsprung mass are investigated through the bode plot. In order to identify the requirements on the design of LSRA in active suspension system, a LQR optimal controller is formulated and simulated with the quarter-car model.

Chapter 3

Preliminary Design of Linear Switched Reluctance Actuator

LSRA is the linear counterpart of rotary switched reluctance motor (RSRM), whose force is generated by the tendency of the translator to align its position with minimum reluctance in the magnetic circuit [63]. The continuous movement is then achieved as the phase windings are sequentially energized with the translator position. By changing the switching position and sequence of excited phase properly, LSRA can be operated at four quadrants.

3.1 Operation Principle

3.1.1 Variation of induction with translator position

The variation of phase inductance determines the dynamic characteristics of LSRA. During the motion of the translator, the inductance of LSRA varies periodically, as illustrated in Fig. 3-1. The inductance of the excited phase reaches the maximum value, $L_{\max}$, when the translator poles are fully aligned with the stator pole. As the translator keeps moving from the aligned position, the phase inductance is decreased, and falls at a minimum value, $L_{\min}$, when the translator poles are fully

unaligned with the stator pole. The mutual inductance has little contribution to the overall effect, and it is neglected in the analysis.

The linear approximation of inductance profile is related to the actuator parameters such as the number of phase and pole, the stator and translator pole width. Two adjacent phases with six translator positions are presented to describe their relationship:

$$x_0 = \frac{1}{2}(w_{ts} - w_{sp}) \tag{3-1}$$

$$x_1 - x_0 = x_3 - x_2 = \min(w_{sp}, w_{tp}) \tag{3-2}$$

$$x_2 - x_1 = \left| w_{sp} - w_{tp} \right| \tag{3-3}$$

$$(x_4 - x_0) = \tau_t = w_{tp} + w_{sp} \tag{3-4}$$

$$(x_5 - x_0) = \sigma = \frac{\tau_t}{N_{ph}} \tag{3-5}$$

where w_{sp} and w_{tp} are the stator and translator pole width, w_{ts} is the translator pole slot, τ_t is the translator pole pitch, σ is the stroke, and N_{ph} is the number of phase. It can be observed that positive force is generated only in the region with increased inductance; thus the phase current should be decreased to zero before the negative force is generated in the region with decreased inductance. Although the overlap region of stator and translator pole contributes no force, it is effective to prevent the current conducting in the region of negative force.

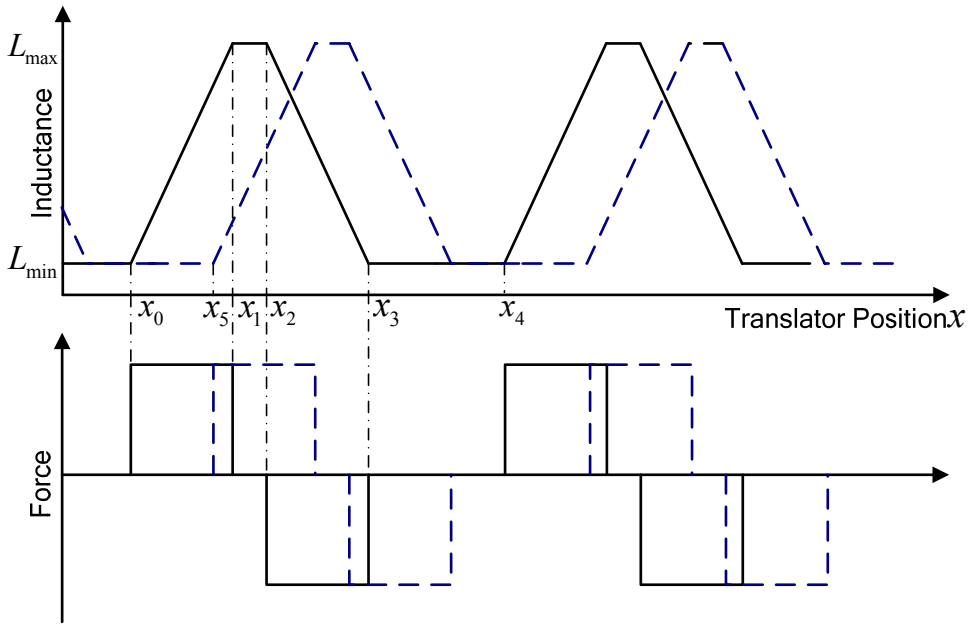

Fig. 3-1 Variation of phase inductance

3.1.2 Equivalent circuit

An equivalent circuit is used to analyze the dynamic performance of a machine. Neglecting the mutual inductance between the phases, the equivalent circuit for one phase of the LSRA is shown in Fig 3-2.

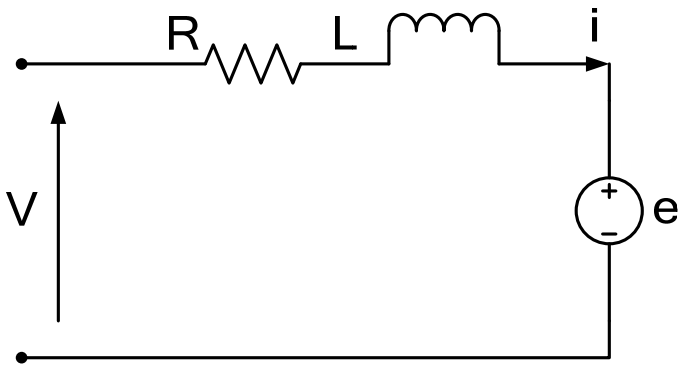

Fig. 3-2 Equivalent circuit

The corresponding voltage equation is given by

$$V = R \cdot i + \frac{d\lambda}{dt} \tag{3-6}$$

$$\lambda = L \cdot i \tag{3-7}$$

$$v = \frac{dx}{dt} \tag{3-8}$$

The overall voltage equation is

$$V = R \cdot i + L \cdot \frac{di}{dt} + v \cdot i \cdot \frac{dL}{dx} \tag{3-9}$$

where V is the applied voltage, i is the phase current, R is the phase resistance, L is the phase inductance, λ is the flux linkage per phase, v is the movement speed, and x is the translator position. The right hand side of equation (3-9) represents the voltage drop in phase resistance, the inductance and the induced EMF, e, respectively.

$$e = v \cdot i \cdot \frac{dL}{dx} \tag{3-10}$$

Then, by multiplied by i on each side of equation (3-9), we know the input electrical power is

$$V \cdot i = R \cdot i^2 + L \cdot i \cdot \frac{di}{dt} + v \cdot i^2 \cdot \frac{dL}{dx} \tag{3-11}$$

Subtracting the energy consumed by resistance, and the rate of change of magnetic stored energy from the input power, the mechanical power is obtained. The rate of change of magnetic stored energy can be derived by

$$\frac{d}{dt}\left(\frac{1}{2} L \cdot i^2\right) = \frac{1}{2} i^2 \cdot \frac{dL}{dt} + L \cdot i \cdot \frac{di}{dt} = \frac{1}{2} v \cdot i^2 \cdot \frac{dL}{dx} + L \cdot i \cdot \frac{di}{dt} \tag{3-12}$$

and the mechanical power is

$$P = F_e \cdot v \tag{3-13}$$

Finally, the dynamic force is thus calculated from above equations

$$F_e = \frac{1}{2}\frac{dL}{dx} \cdot i^2 \tag{3-14}$$

It can be observed that the direction of force is determined by the change of inductance with translator position, and irrespective to the direction of phase current.

3.1.3 Energy conversion principle

The steady-state and dynamic-state performance of LSRA can be evaluated by calculating the energy conversion for one stroke. Consider the energy conversion procedure for one phase as shown in Fig. 3-3. Assuming the translator moves for a distance dx under the action of force F, the mechanical work is

$$dW_m = F_e dx \tag{3-15}$$

If losses are neglected, the amount of electrical energy W_e is transferred into the magnetic field W_f and mechanical work W_m, which can be written as in (3-16)

$$dW_e = dW_f + dW_m \tag{3-16}$$

From the above equations, we can write down

$$dW_f = dW_e - F_e dx = id\lambda - Fdx \tag{3-17}$$

If we define the area between the aligned and unaligned curves as the coenergy W_f', which does not exist physically, we can obtain

$$dW_f'(i,x) = \lambda di + F_e dx = \frac{\partial W_f'(i,x)}{\partial i} di + \frac{\partial W_f'(i,x)}{\partial x} dx \tag{3-18}$$

Therefore,

$$\lambda = \frac{\partial W_f'(i,x)}{\partial i} \tag{3-19}$$

$$F_e = \frac{\partial W_f'(i,x)}{\partial x} \tag{3-20}$$

From the diagram shown in Fig. 3-3, the coenergy for one stroke can be calculated by

$$W_f'(i,x) = \int_0^i (\lambda_a(i,x) - \lambda_u(i,x))di \tag{3-21}$$

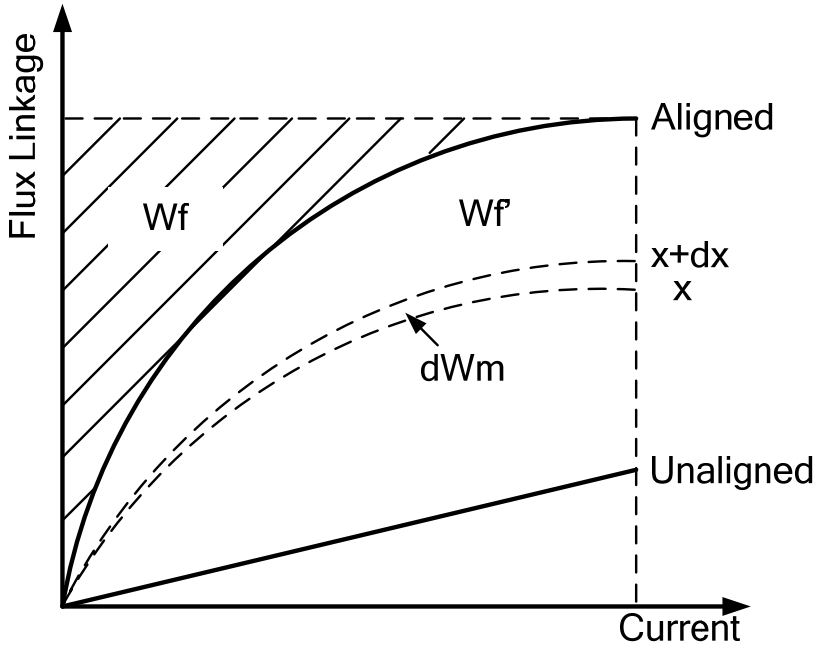

Fig. 3-3 Energy conversion procedures

3.2 Structure of the Proposed LSRA

3.2.1 Design requirements

On the basis of extensive analysis and simulations presented in Chapter 2, the requirements on LSRA design are obtained and summarized in Table 3-1. The requirements are determined to achieve satisfactory performance of riding comfort and road handling quality over a wide range of driving condition. Furthermore, the volume of suspension system is proposed as a critical design constraint for the potential practical application in commercial vehicles.

TABLE 3-1
DESIGN REQUIREMENTS ON LSRA

Parameters	Value
Peak force	1000N
Continuous force	500N
Max. Displacement	100mm
Max. Speed	1m/s
Max. Volume	300*300*600mm

3.2.2 Structure determination

A. Selection of topology

Double-sided structure has the advantage of higher force density than single-sided structure [64], and four double-sided LSRA modules can be arranged in a more compact configuration, because the lateral forces by both sides of the stator are eliminated. Moreover, this elimination is helpful for reducing the acoustic noise during the operation [65]. Lastly, this configuration is easier for heat dissipation due to the good thermal contact of the coil and the actuator frame, which consequently enhances the overload capability of LSRA.

B. Selection of number of phases

A higher number of phases, N_{ph} can alleviates the problem of force dips, and can increase the average force. Meanwhile, it is more efficient to reduce the force ripple during dynamic operation with smaller static force dip, due to the unnecessary peak current in the low torque region. Moreover, higher power density can be obtained by a higher number of phases. On the other hand, the actuator with higher number of phase will have less winding area, increased number of power switching devices and current transducer, which consequently increase the cost of actuator drives.

After considering the above factors, a four-phase topology is chosen by making a compromise. More effective force region overlap between two neighboring phases is ensured by four-phase topology than three-phase topology; hence the force ripple problem can be alleviated, and the reliability is increased with relative simple structure.

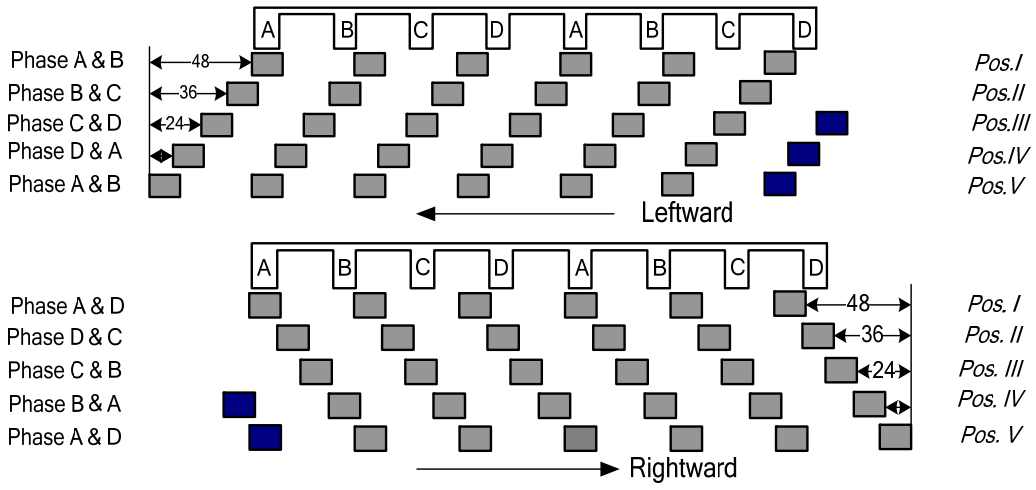

Fig. 3-4 Movement of translator poles

C. Selection of number of pole

The number of stator pole, N_{sp}, is consequently determined at eight for single side, since the actuator has a four phase structure. For the industrial design of rotary switched reluctance motor, the number of rotor pole is fixed at six as a common combination with eight stator poles. However, the situation is not suitable for determining the number of translator pole of LSRA, N_{tp}, which is related to the range of movement. More translator poles can extend the movement distance, but result in a longer and heavier translator.

The operation modes of rightward and leftward movement are demonstrated in Fig. 3-4. Pos. I is defined as the central position, and the operation range of translator is -50mm to +50mm. It can be observed that a positive translator pole is required at the right side if further leftward movement is needed from the Pos. III, and an additional translator pole is required at the left side if further rightward movement is needed from Pos. IV. Therefore, to ensure the normal operation over a range of 100mm, at least eight translator poles are required.

D. Selection of pole width

The pole width of stator, w_{sp}, and translator, w_{tp}, are important parameters for the design of LSRA. The selections have a direct effect on the average force and force ripple of the actuator. Meanwhile, the stator back iron thickness is related to the stator pole width. Larger pole width results in thicker stator back iron, and increased actuator weight. Therefore, the pole width of stator and translator need

to be optimized to improve the characteristics of LSRA. The detailed process for optimization is presented in Chapter 5.

E. Selection of air gap

The length of the air gap g, is also critical to the actuator characteristic, and its determination is irrespective to other actuator parameters. The air gap should be designed as small as is achievable in manufacture, because both the average force and efficiency are inversely proportional to the air gap length [66]. Furthermore, the uniformity of air gap is important to the performance of double-sided LSRA. The lateral force may not be eliminated with nonuniformity in air gap, and cause unexpected resistance force and serious audible noise.

F. Selection of power and voltage level

The selection of power depends on the required force and speed from active suspension system, as is shown in Table 3-1. The power source of LSRA is the battery bank in the vehicle. Therefore, a low voltage supply is more applicable. However, it will result in larger excitation current for the same power level. Thus, a compromise needs to be considered in selecting the voltage level.

3.2.3 Configuration of LSRA

The proposed LSRA consists of four identical double-sided LSRA modules with active stator and passive translator. Fig. 3-5 (a) shows the configuration of double-sided module. Each module is made of four phases with eight pairs of stator

poles and eight translator poles. The translator weight is considerably reduced due to the absence of excitation windings and back iron. The assembly of four LSRA modules is demonstrated in Fig. 3-5 (b). The translators per module are connected into one by a hollow shaft, where the spring is to be placed. There are sixteen coils per phase that connected in series. It can be observed that the cross-sectional area is related to the pole height, stack length, stator pole width and winding dimension.

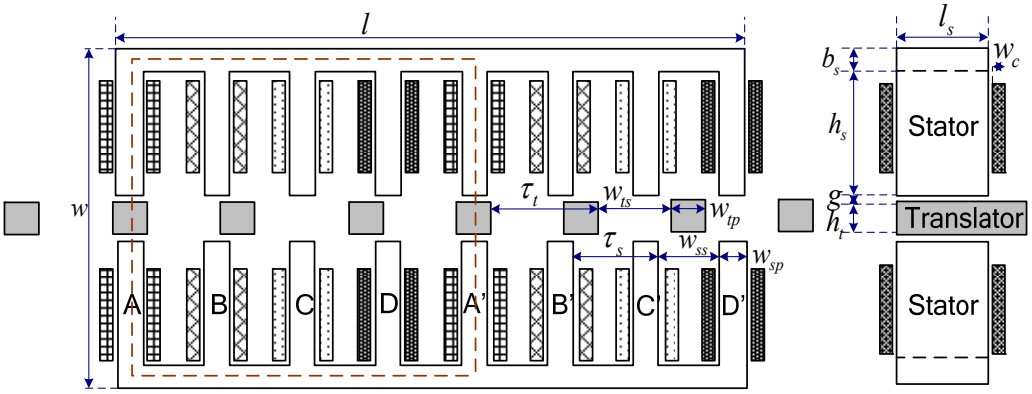

(a) Double-sided LSRA module

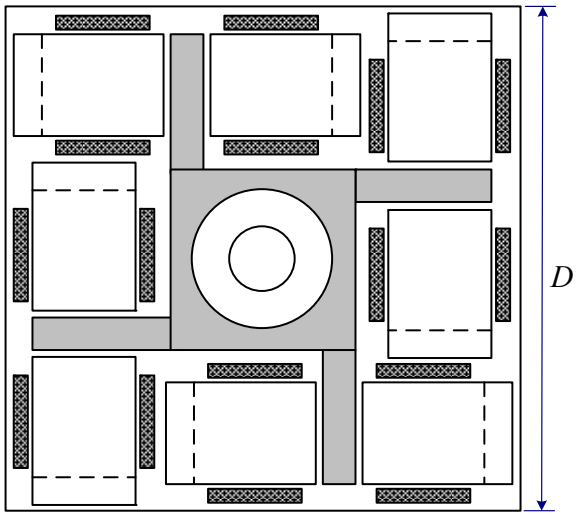

(b) Cross-section of proposed LSRA

Fig. 3-5 Configuration of proposed LSRA

The basic relationship of parameters is given by

$$\tau_t = w_{tp} + w_{ts} \tag{3-22}$$

$$\tau_s = w_{sp} + w_{ss} \tag{3-23}$$

$$l = 7\tau_s + w_{sp} = 8w_{sp} + 7w_{ss} \tag{3-24}$$

$$b_s = w_{sp} \tag{3-25}$$

$$w = 2(b_s + h_s + g) + h_t \tag{3-26}$$

$$D \geq w + l_s + 2w_c \tag{3-27}$$

$$A_c = w_c \times h_c \tag{3-28}$$

where w_{ss} and w_{ts} are the slot width of stator and translator, τ_s and τ_t are the stator and translator pitch, l and l_s are the length of stator and stack, b_s is the thickness of stator back iron, h_s and h_t are the pole height of stator and translator, w and D are the width of double-sided module and proposed LSRA, w_c , h_c and A_c are the winding width, height and area, respectively.

3.3 Magnetic circuit analysis

From the principle of energy conversion, the actuator characteristics can be derived from the flux linkage vs. excitation current at various translator positions. Therefore, it is important to predict the flux linkage characteristics during the design stage. As the flux linkage can be obtained by taking the product of inductance and current, the inductance is calculated instead of the flux linkage in the following content.

Finite element method (FEM) is preferred to calculate the flux linkage characteristics if the actuator dimension and excitation are determined. However, the actuator design variables, such as pole width, height, stack length and etc, can be changeable in the design stage. The process would be complex and time-consuming when FEM is applied. Therefore, analytical calculation based on the geometrical dimensions is a better and faster approach to obtain the flux linkage characteristics, since the relationship between actuator performance and design variables can be expressed analytically. Although the nonlinearity and saturation are not considered during the analytical process, the accuracy for preliminary design is adequate. The performance can be further verified by FEM which considers nonlinearity and local saturation.

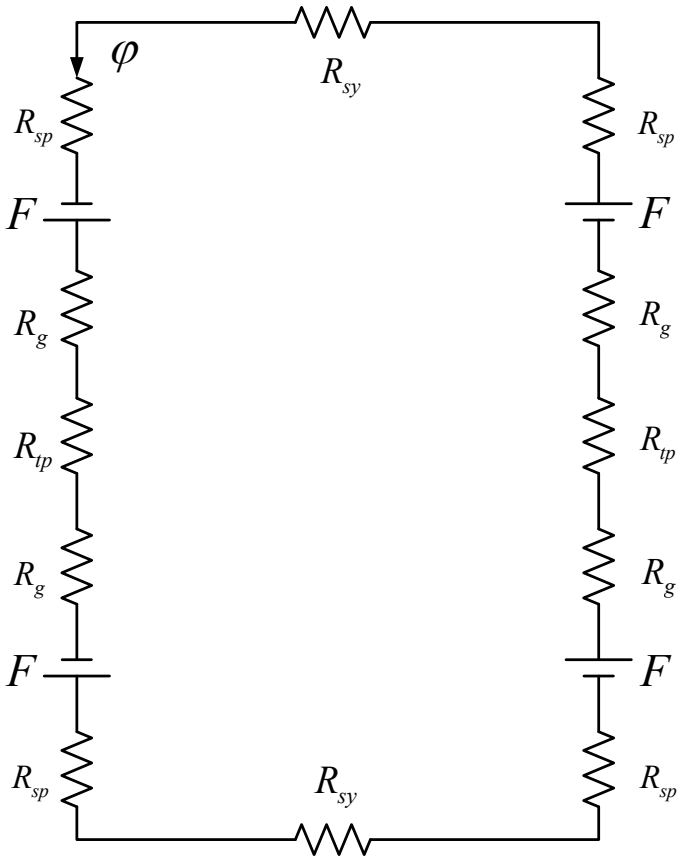

Fig. 3-6 Magnetic equivalent circuit for double-sided LSRA

From the distribution of flux lines, a number of flux paths are assumed for each translator position, and each flux path contributes a part of the total inductance. The inductance of each path can be calculated on the basis of magnetic equivalent circuit, which is illustrated in Fig. 3-6. Each segment of the double-sided module is represented by the corresponding reluctance, R , and the magntomotive force (MMF), F . The equivalent circuit can be further simplified due to the symmetric topology and shown in Fig. 3-7.

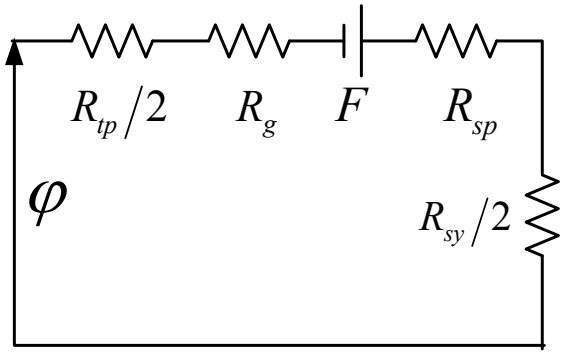

Fig. 3-7 Simplified magnetic equivalent circuit for double-sided LSRA

The reluctance of each segment can be calculated from the magnetic circuit's permeability, effective length and area. The reluctance of the stator pole, translator pole, stator yoke are given by:

$$R_{sp} = \frac{l_{sp}}{\mu_{sp} \cdot A_{sp}} = \frac{H_{sp}}{B_{sp}} \cdot \frac{l_{sp}}{A_{sp}} \tag{3-29}$$

$$R_{tp} = \frac{l_{tp}}{\mu_{tp} \cdot A_{tp}} = \frac{H_{tp}}{B_{tp}} \cdot \frac{l_{tp}}{A_{tp}} \tag{3-30}$$

$$R_{sy} = \frac{l_{sy}}{\mu_{sy} \cdot A_{sy}} = \frac{H_{sy}}{B_{sy}} \cdot \frac{l_{sy}}{A_{sy}} \tag{3-31}$$

The reluctance of the air gap is

$$R_g = \frac{l_g}{\mu_0 \cdot A_g} \tag{3-32}$$

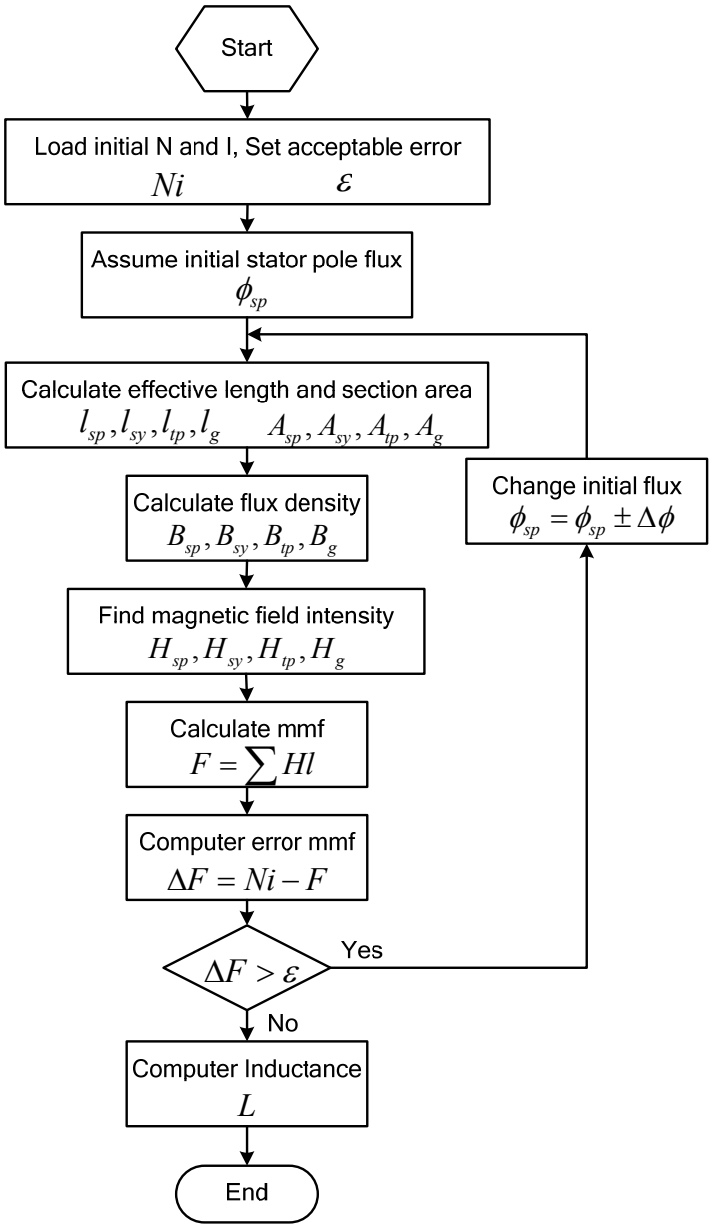

Fig. 3-8 Flow chart of inductance calculation

The Ampere's circuital law is applied to find the magnetic flux of each path through an iterative process. The flow chart for the inductance calculation is shown

in Fig. 3-8. First, an initial value of flux in stator pole, φ_k, is assumed, and the effective length, l_j, and area, A_j, of each segment in path k are calculated. Second, the flux density of each segment, B_j, is calculated by

$$B_j(i,x) = \frac{\varphi_k}{A_j} \tag{3-33}$$

The magnetic field intensity, H_j, is then obtained from the corresponding flux density by using the B-H curve. Third, the applied MMF is compared with the calculated MMF from each segment. The error ΔF_k is then used to adjust the assumed flux iteratively until it is reduced to the predefined value ε.

$$\Delta F_k = f_k(Ni) - \sum H_j l_j < \varepsilon \tag{3-34}$$

After the last iteration, the magnetic flux in stator pole is obtained for the calculation of inductance of path k. Likewise, the inductance of each path is obtained, and the total inductance per phase is the sum of inductance of each path.

$$L_k = \frac{N \cdot \varphi_k}{i} \tag{3-35}$$

$$L = \sum_k L_k \tag{3-36}$$

where L is the total inductance per phase, L_k is the inductance of each flux path.

3.3.1 Calculation of maximum inductance

The maximum inductance of the LSRA is obtained when the translator poles are fully aligned with the stator poles. The magnetic flux paths in the air gap that consider three-dimensional effects are demonstrated in Fig. 3-9. Note that only one

pair of stator and translator pole is showed for simplicity, due to the symmetric distribution of flux paths. It can be observed that each flux path is presented in straight lines and circular arcs. Totally seven flux paths are considered, and the contribution of each path to the maximum inductance is calculated separately.

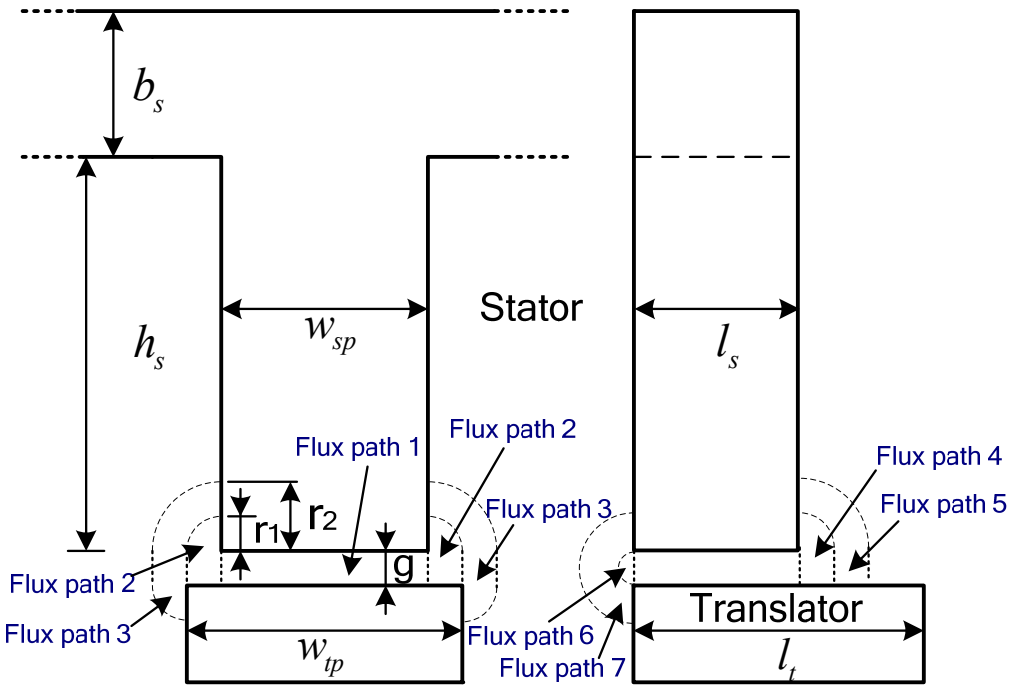

Fig. 3-9 Magnetic Flux paths at fully aligned position

3.3.1.1 Flux Path 1

The flux path 1 is the main flux linkages for the calculation of phase inductance. The effective length l_{sp1} and cross-section area A_{sp1} of the flux path at stator pole are

$$l_{sp1} = h_s + b_s/2 \tag{3-37}$$

$$A_{sp1} = w_{sp} \cdot l_s \tag{3-38}$$

where h_s and w_{sp} are the height and width of stator pole, b_s is the thickness of

stator yoke, and l_s is the stator stack length.

The effective length l_{sy1} and cross-section area A_{sy1} in stator yoke are

$$l_{sy1} = 2\tau_s \tag{3-39}$$

$$A_{sy1} = b_s \cdot l_s \tag{3-40}$$

The effective length l_{tp1} and cross-section area A_{tp1} in translator pole are

$$l_{tp1} = h_t / 2 \tag{3-41}$$

$$A_{tp1} = w_{tp} \cdot l_t \tag{3-42}$$

where h_t , w_{tp} and l_s are the height, width and stack length of translator pole, respectively.

The reluctance of the air gap R_{g1} is given as

$$R_{g1} = \frac{2g}{u_0 \cdot l_s \cdot (w_{sp} + w_{tp})} \tag{3-43}$$

where g is the length of air gap, u_0 is the permeability of free space.

The MMF for flux path 1 is

$$F_1 = N \cdot i \tag{3-44}$$

Hence, the inductance of path 1 can be calculated by

$$L_1 = \frac{N \cdot \phi_1}{i} = \frac{N \cdot (F_1 / (\Re_{sp} + \Re_g + \Re_{tp}/2 + R_{sy}/2))}{i} \tag{3-45}$$

3.3.1.2 Flux Path 2

The effective length and cross-section area of flux path 2 in the stator pole, stator yoke and translator pole are the same as that of flux path 1, and denoted here

as l_{sp2}, A_{sp2}, l_{sy2}, A_{sy2}, l_{tp2}, A_{tp2}, respectively.

The reluctance of the air gap R_{g2} is two reluctances R_{g2_1} and R_{g2_2} in series, which are given as

$$R_{g2\_1} = \frac{1.22 r_1}{u_0 \cdot (0.644 r_1 \cdot l_s)} = \frac{1.89}{u_0 \cdot l_s} \tag{3-46}$$

$$R_{g2\_2} = \frac{2g}{u_0 \cdot l_s \cdot (w_{tp} - w_{sp})} \tag{3-47}$$

$$R_{g2} = R_{21} + R_{22} \tag{3-48}$$

where r_1 is obtained as:

$$r_1 = (w_{tp} - w_{sp})/2 \tag{3-49}$$

The MMF for flux path 2 is

$$F_2 = N \cdot i \tag{3-50}$$

Hence, the inductance of path 2 can be calculated by

$$L_2 = \frac{N \cdot \phi_2}{i} \tag{3-51}$$

3.3.1.3 Flux Path 3

The effective length l_{sp3} and cross-section area A_{sp3} of the flux path at stator pole are

$$l_{sp3} = h_s + b_s/2 - R_1/2 \tag{3-52}$$

$$A_{sp3} = w_{sp} \cdot l_s \tag{3-53}$$

The effective length l_{sy3} and cross-section area A_{sy3} in stator yoke are

$$l_{sy3} = 2\tau_s \tag{3-54}$$

$$A_{sy3} = b_s \cdot l_s \tag{3-55}$$

The effective length l_{tp1} and cross-section area A_{tp1} in translator pole are

$$l_{tp3} = \frac{h_t}{2} - (r_2 - r_1) \tag{3-56}$$

$$A_{tp3} = w_{tp} \cdot l_t \tag{3-57}$$

where

$$r_2 = \frac{h_s}{12} \tag{3-58}$$

The air gap of flux path 3 consists of a half annulus, a cube and a quarter cylinder. The reluctance of each section is derived as

$$\frac{1}{R_{g3\_1}} = \frac{2u_0 \cdot l_s}{\pi} \ln(1 + \frac{r_2 - r_1}{r_1}) \tag{3-59}$$

$$R_{g3\_2} = \frac{g}{u_0 \cdot l_s \cdot (r_2 - r_1)} \tag{3-60}$$

$$R_{g3\_3} = \frac{0.61(r_2 - r_1)}{u_0 \cdot l_s \times 0.322(r_2 - r_1)} = \frac{1.89}{u_0 \cdot l_s} \tag{3-61}$$

The total reluctance R_{g3} is then obtained as

$$R_{g3} = R_{g3\_1} + R_{g3\_2} + R_{g3\_3} \tag{3-62}$$

The MMF for flux path 3 is

$$F_3 = \frac{h_s - r_2/2}{h_s} N \cdot i \tag{3-63}$$

Hence, the inductance of path 3 can be calculated by

$$L_3 = \frac{N \cdot \phi_3}{i} \tag{3-64}$$

3.3.1.4 Flux Path 4

The effective length l_{sp4} and cross-section area A_{sp4} of the flux path at stator pole are

$$l_{sp4} = h_s + b_s/2 \tag{3-65}$$

$$A_{sp4} = w_{sp} \cdot l_s \tag{3-66}$$

The effective length l_{sy4} and cross-section area A_{sy4} in stator yoke are

$$l_{sy4} = 2\tau_s \tag{3-67}$$

$$A_{sy4} = b_s \cdot l_s \tag{3-68}$$

The effective length l_{tp1} and cross-section area A_{tp1} in translator pole are

$$l_{tp4} = h_t/2 \tag{3-69}$$

$$A_{tp4} = w_{tp} \cdot l_t \tag{3-70}$$

The reluctance of the air gap R_{g4} is two reluctances R_{g4_1} and R_{g4_2} in series, which are given as

$$R_{g4\_1} = \frac{2 \times 1.22 r_1}{u_0 \cdot 0.644 r_1 \cdot (w_{tp} + w_{sp})} = \frac{3.78}{u_0 \cdot w_{sp}} \tag{3-71}$$

$$R_{g4\_2} = \frac{2g}{u_0 \cdot (w_{sp} + w_{tp}) \cdot r_1} \tag{3-72}$$

$$R_{g4} = \Re_{g4\_1} + \Re_{g4\_2} \tag{3-73}$$

The MMF for flux path 4 is

$$F_4 = N \cdot i \tag{3-74}$$

Hence, the inductance of path 4 can be calculated by

$$L_4 = \frac{N \cdot \phi_4}{i} \tag{3-75}$$

3.3.1.5 Flux path 5

The effective length and cross-section area of flux path 5 in the stator pole, stator yoke and translator pole are the same as that of flux path 4, and denoted here as l_{sp5}, A_{sp5}, l_{sy5}, A_{sy5}, l_{tp5}, A_{tp5}, respectively.

The reluctance of the air gap R_{g5} is two reluctances R_{g5_1} and R_{g5_2} in series, which are given as

$$\frac{1}{R_{g5\_1}} = \frac{u_0 \cdot (w_{sp} + w_{tp})}{\pi} \ln(1 + \frac{r_2 - r_1}{r_1}) \tag{3-76}$$

$$R_{g5\_2} = \frac{2g}{u_0 \cdot (w_{sp} + w_{tp}) \cdot (r_2 - r_1)} \tag{3-77}$$

$$R_{g5} = R_{g5\_1} + R_{g5\_2} \tag{3-78}$$

The MMF for flux path 5 is

$$F_5 = \frac{h_s - r_2/2}{h_s} N \cdot i \tag{3-79}$$

Hence, the inductance of path 5 can be calculated by

$$L_5 = \frac{N \cdot \phi_5}{i} \tag{3-80}$$

3.3.1.6 Flux path 6

The effective length and cross-section area of flux path 6 in the stator pole, stator yoke and translator pole are the same as that of flux path 4, and denoted here as l_{sp6}, A_{sp6}, l_{sy6}, A_{sy6}, l_{tp6}, A_{tp6}, respectively.

The reluctance of the air gap R_{g6} is given as

$$R_{g6} = \frac{2 \times 1.22g}{u_0 \cdot 0.322g \cdot (w_{sp} + w_{tp})} = \frac{7.58}{u_0 \cdot w_{sp}} \tag{3-81}$$

The MMF for flux path 6 is

$$F_6 = N \cdot i \tag{3-82}$$

Hence, the inductance of path 6 can be calculated by

$$L_6 = \frac{N \cdot \phi_6}{i} \tag{3-83}$$

3.3.1.7 Flux path 7

The effective length and cross-section area of flux path 7 in the stator pole and stator yoke are the same as that of flux path 3, and denoted here as l_{sp7}, A_{sp7}, l_{sy7}, A_{sy7}, respectively.

The effective length l_{tp7} and cross-section area A_{tp7} in translator pole are

$$l_{tp7} = \frac{h_t}{2} - r_1 \tag{3-84}$$

$$A_{tp7} = w_{tp} \cdot l_t \tag{3-85}$$

The reluctance of the air gap R_{g7} is given as

$$\frac{1}{R_{g7}} = \frac{u_0 \cdot (w_{sp} + w_{tp})}{2\pi} \ln(1 + \frac{2r_1 + g}{g}) \tag{3-86}$$

The MMF for flux path 6 is

$$F_7 = \frac{h_s - r_1/2}{h_s} N \cdot i \tag{3-87}$$

Hence, the inductance of path 7 can be calculated by

$$L_7 = \frac{N \cdot \phi_7}{i} \tag{3-88}$$

The total inductance in aligned position is contributed by above seven paths, and given by

$$L_{aligned} = \sum_{1}^{7} L_k \tag{3-89}$$

3.3.2 Calculation of minimum inductance

It can be observed from Fig. 3-10 that the flux path 4, 5, 8 and 9 pass through the free space between stator poles and enclose the path through the stator yoke. Therefore, no reluctance in translator pole is taken into consideration for there flux paths.

At fully unaligned position, all flux paths, except for the flux path 5, have the same effective length l_{syk} and cross-section area A_{syk}, which can be derived as

$$l_{sy1\sim4,6\sim9} = 2\tau_s \tag{3-90}$$

$$A_{sy} = b_s \cdot l_s \tag{3-91}$$

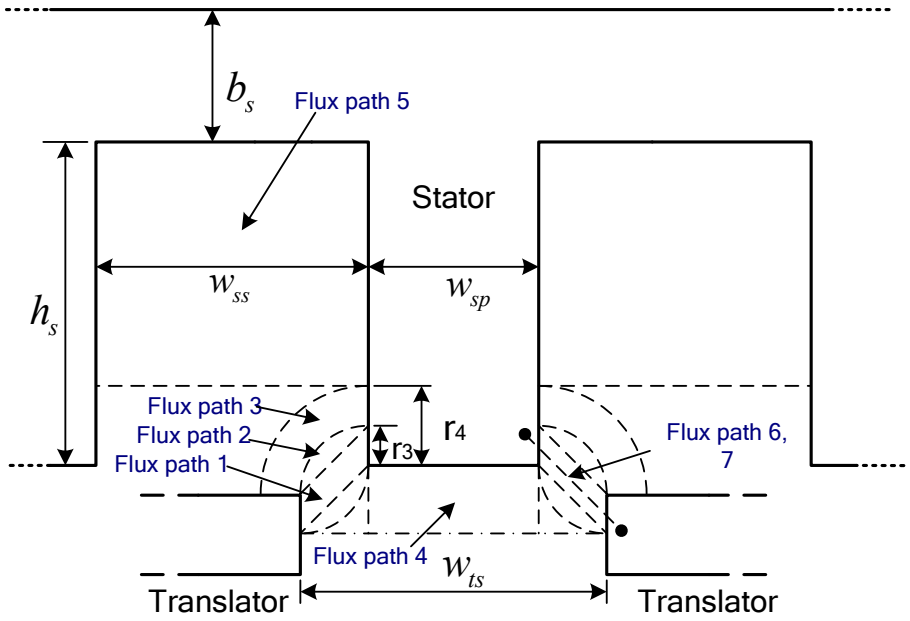

(a)

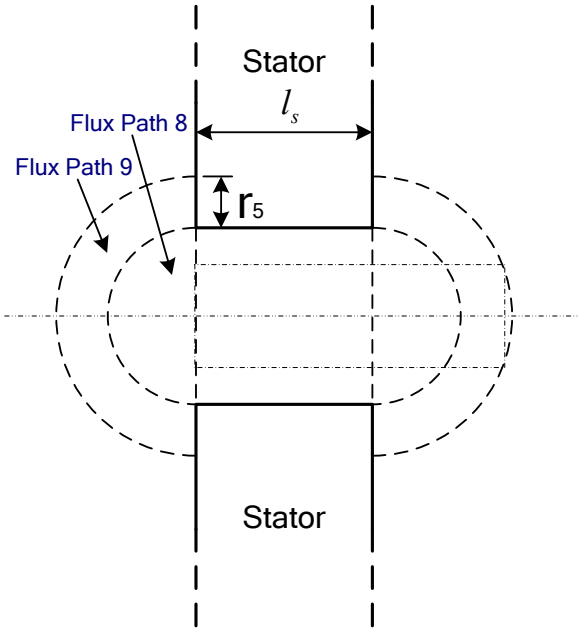

(b)

Fig. 3-10 Magnetic Flux paths at fully unaligned position

3.3.2.1 Flux Path 1

The effective length l_{sp1} and cross-section area A_{sp1} of the flux path at stator pole are

$$l_{sp1} = h_s + b_s/2 - r_2/2 \tag{3-92}$$

$$A_{sp1} = w_{sp} \cdot l_s \tag{3-93}$$

The effective length l_{tp1} and cross-section area A_{tp1} in translator pole are

$$l_{tp1} = r_3/2 \tag{3-94}$$

$$A_{tp1} = w_{tp} \cdot l_t \tag{3-95}$$

The reluctance of the air gap R_{g1} is given as

$$R_{g1} = \frac{\sqrt{2}\,(w_{ts} - w_{sp})/2}{u_0 \cdot l_s \cdot r_3/\sqrt{2}} = \frac{w_{ts} - w_{sp}}{u_0 \cdot l_s \cdot r_3} \tag{3-96}$$

where r_3 is obtained by

$$r_3 = \frac{w_{ts} - w_{sp} - 2g}{2} \tag{3-97}$$

The MMF for flux path 1 is

$$F_1 = \frac{h_s - r_3/2}{h_s} \cdot Ni \tag{3-98}$$

Hence, the inductance of path 1 can be calculated by

$$L_1 = \frac{N \cdot \phi_1}{i} = \frac{N \cdot (F_1/(\Re_{sp} + \Re_g + \Re_{tp}/2 + R_{sy}/2))}{i} \tag{3-99}$$

3.3.2.2 Flux Path 2

The effective length l_{sp2} and cross-section area A_{sp2} of the flux path at stator pole are

$$l_{sp2} = h_s + b_s/2 - r_2 \tag{3-100}$$

$$A_{sp2} = w_{sp} \cdot l_s \tag{3-101}$$

The effective length l_{tp2} and cross-section area A_{tp2} in translator pole are

$$l_{tp2} = h_t/2 \tag{3-102}$$

$$A_{tp} = w_{tp} \cdot l_t \tag{3-103}$$

The reluctance of the air gap R_{g2} is given as

$$R_{g2} = \frac{1.462 \cdot (\frac{w_{ts} - w_{sp}}{2})}{u_0 \left(\frac{0.285 \cdot l_s}{1.462} \cdot (\frac{w_{ts} - w_{sp}}{2}) \right)} = \frac{7.5}{u_0 \cdot l_s} \tag{3-104}$$

The MMF for flux path 2 is

$$F_2 = \frac{h_s - r_2}{h_s} \cdot Ni \tag{3-105}$$

Hence, the inductance of path 2 can be calculated by

$$L_2 = \frac{N \cdot \phi_2}{i} \tag{3-106}$$

3.3.2.3 Flux Path 3

The effective length l_{sp3} and cross-section area A_{sp3} of the flux path at stator pole are

$$l_{sp3} = h_s + b_s/2 - r_4 \tag{3-107}$$

$$A_{sp} = w_{sp} \cdot l_s \tag{3-108}$$

where r_4 is given by

$$r_4 = \frac{2 \cdot w_{ss}}{3} - g \tag{3-109}$$

The effective length l_{tp3} and cross-section area A_{tp3} in translator pole are

$$l_{tp3} = r_3 \tag{3-110}$$

$$A_{tp} = w_{tp} \cdot l_s \tag{3-111}$$

The reluctance of the air gap R_{g3} is given as

$$\frac{1}{R_{g3}} = \frac{2u_0 \cdot l_s}{\pi} \ln(1 + \frac{r_4 - r_3}{r_3}) \tag{3-112}$$

The MMF for flux path 3 is

$$F_3 = \frac{h_s - r_3 - (r_4 - r_3)/2}{h_s} \cdot Ni \tag{3-113}$$

Hence, the inductance of path 3 can be calculated by

$$L_3 = \frac{N \cdot \phi_3}{i} \tag{3-114}$$

3.3.2.4 Flux Path 4

The effective length l_{sp4} and cross-section area A_{sp4} of the flux path at stator pole are

$$l_{sp4} = h_s + b_s/2 \tag{3-115}$$

$$A_{sp4} = w_{sp} \cdot l_s \tag{3-116}$$

The reluctance of the air gap R_{g4} is given as

$$R_{g4} = \frac{(h_t/2) + g}{u_0 \cdot (l_s \cdot w_{sp})} \tag{3-117}$$

The MMF for flux path 4 is

$$F_4 = Ni \tag{3-118}$$

Hence, the inductance of path 4 can be calculated by

$$L_4 = \frac{N \cdot \phi_4}{i} \tag{3-119}$$

3.3.2.5 Flux Path 5

The effective length l_{sp5} and cross-section area A_{sp5} of the flux path at stator pole are

$$l_{sp5} = 2 \times ((h_s - R_2)/2 + b_s/2) \tag{3-120}$$

$$A_{sp5} = w_{sp} \cdot l_s \tag{3-121}$$

The effective length l_{sy5} of the flux path at stator yoke is

$$l_{sy5} = \tau_s \tag{3-122}$$

and the cross-section area A_{sy5} is the same as other paths.

The reluctance of the air gap R_{g5} is given as

$$R_{g5} = \frac{w_{ss}}{u_0 \cdot l_s (h_s - R_2)} \tag{3-123}$$

The MMF for flux path 5 is

$$F_5 = \frac{h_s - (w_{ts} - w_{sp})/2}{h_s} Ni \tag{3-124}$$

Hence, the inductance of path 5 can be calculated by

$$L_5 = \frac{N \cdot \phi_5}{i} \tag{3-125}$$

3.3.2.6 Flux Path 6 and 7

The effective length and cross-section area of flux path 6, 7in the stator pole and translator pole are the same as that of flux path 1, and denoted here as $l_{sp6}, l_{sp7}, A_{sp6}, A_{sp7}, l_{tp6}, l_{tp7}, A_{tp6}, A_{tp7}$, respectively. The reluctances R_{g6} and R_{g7} of the air gap are given as

$$R_{g6} = \frac{1.713 \cdot (\frac{w_{ts} - w_{sp}}{2})}{u_0 \left(\frac{0.393 \cdot r_2}{1.713} (\frac{w_{ts} - w_{sp}}{2}) \right)} = \frac{7.47}{u_0 \cdot r_2} \tag{3-126}$$

$$R_7 = \frac{\frac{\sqrt{2}\pi}{4} \cdot (w_{ts} - w_{sp} + R_2 - r_2)}{u_0 \cdot \frac{r_2}{\sqrt{2}} \cdot \frac{R_2 - r_2}{2}} = \frac{\pi \cdot (w_{ts} - w_{sp} + R_2 - r_2)}{u_0 \cdot r_2 \cdot (R_2 - r_2)} \tag{3-127}$$

The MMF for flux path 6 and 7 are the same as flux path 1.

Hence, the inductance of path 6 and 7 can be calculated by

$$L_6 = \frac{N \cdot \phi_6}{i} \tag{3-128}$$

$$L_7 = \frac{N \cdot \phi_7}{i} \tag{3-129}$$

3.3.2.7 Flux Path 8

The effective length and cross-section area of flux path 8 in the stator pole are the same as that of flux path 4, and denoted here as l_{sp4}, A_{sp4}, respectively.

The reluctance of the air gap R_{g8} is given as

$$R_{g8} = \frac{2 \times 1.22(h_t + 2g)}{u_0 \cdot w_{sp} \cdot 0.322(h_t + 2g)} = \frac{7.58}{u_0 \cdot w_{sp}} \tag{3-130}$$

The MMF for flux path 8 is the same as flux path 4.

Hence, the inductance of path 8 can be calculated by

$$L_8 = \frac{N \cdot \phi_8}{i} \tag{3-131}$$

3.3.2.8 Flux Path 9

The effective length l_{sp9} and cross-section area A_{sp9} of the flux path at stator pole are

$$l_{sp9} = h_s + b_s/2 - r_5 \tag{3-132}$$

$$A_{sp9} = w_{sp} \cdot l_s \tag{3-133}$$

where r_5 is obtained as

$$r_5 = \frac{h_s}{8} \tag{3-134}$$

The reluctance of the air gap R_{g9} is given as

$$\frac{1}{R_9} = \frac{2u_0 \cdot w_{sp}}{\pi} \ln(1 + \frac{r_5}{(h_t/2) + g}) \tag{3-135}$$

The MMF for flux path 9 is the same as flux path 4.

Hence, the inductance of path 9 can be calculated by

$$L_9 = \frac{N \cdot \phi_9}{i} \tag{3-136}$$

The total inductance in aligned position is contributed by above seven paths, and given by

$$L_{unaligned} = \sum_{1}^{9} L_k \tag{3-137}$$

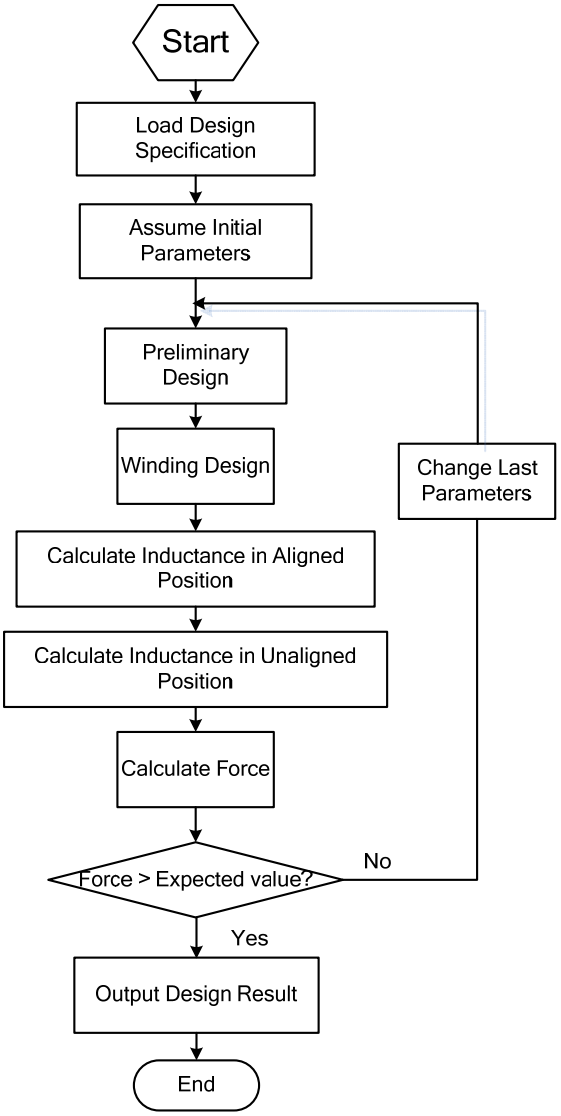

Fig. 3-11 Flowchart of preliminary design

3.4 Preliminary Design Procedure

Based on the requirements from active suspension system, the expected force and outer dimension limitation of LSRA are defined in the first place, then the range of variation in design variables, such as pole width, pole height, stack length, can be derived from the relationship that listed in Section 3.2.3, since the number of phase, stator pole and translator pole are determined after comprehensive consideration.

$$12 \le w_{sp} \le 25 \tag{3-135}$$

$$12 \le w_{tp} \le 32 \tag{3-136}$$

$$\tau_s \le 41 \tag{3-137}$$

$$\tau_t \le 54 \tag{3-138}$$

$$w_c < \frac{w_{ss}}{2} \tag{3-139}$$

$$h_s > h_c = \frac{N \cdot d_c^2}{w_c} \tag{3-140}$$

$$2h_s + l_s \le 240 \tag{3-141}$$

The detailed procedure for preliminary design is demonstrated in Fig. 3-11. The design variables are assumed an initial value at first iteration, and then the winding area is estimated before the inductances at unaligned and aligned position are calculated. The force can be calculated by solving the equation (3-20) when the flux linkage characteristics are obtained. The computed force is then compared with the desired force. If the value does not meet the requirement, some design variables are changed within the acceptable range, and continue the iterative process until the

force is greater than the expected force.

The preliminary specification of LSRA is obtained after the last iteration, as presented in Table 3-2. The accuracy should be further verified by the finite element method due to the limitation of analytical method. It is noted that the result is not the only solution that meet the requirements, and the performance of each qualified solution is varied regarding force ripple or force density. Therefore, it is necessary to determine an optimal specification according to the above criteria.

TABLE 3-2
PRELIMINARY SPECIFICATION OF LSRA

Parameters	Value
Number of module	4
Number of phase	4
Number of stator pole per module	16
Number of translator pole	8
Stator pole pitch	36 mm
Translator pole pitch	48 mm
Stator pole width	12 mm
Translator pole width	14 mm
Stator pole height	49 mm
Stator yoke thickness	12 mm
Stack length	43 mm
Air-gap length	0.8 mm
Number of turns per coil	111
Rated phase current	12A

3.5 Summary

In this chapter, the operation principle of LSRA is summarized to provide the basis for the preliminary actuator design. According to the constraints and requirements from the active suspension system, the configuration of LSRA is proposed. As the actuator performance can be predicted by evaluating the flux linkage characteristics, the inductance at aligned and unaligned positions are

calculated based on the magnetic equivalent circuit through an iterative process. The accuracy of calculated results can be improved as more flux paths are considered at each translator position.

Chapter 4

Longitudinal and transversal end effects analysis of the LSRA

Since the magnetic flux distribution is approximated with the limited flux paths method in the magnetic equivalent circuit, the analytical design results are less accurate than the finite element method (FEM), especially for the unaligned position with omission of leakage flux. Hence, analytical method is suitable for the preliminary machine design and the qualitative understanding on the effects of dimensional changes, and FEM is suitable for the verification on the analytical design results and for the improvement in the performance with optimized design parameters.

Two-dimensional FEM is widely used in predicting the performance characteristics for its simplicity and fast calculation time. Satisfactory results can be ensured for the LSRA with long stack length or with low flux saturation. The prediction accuracy becomes insufficient as the stack length gets shorter, because the transversal end effect, which is ignored in two-dimensional FEM, becomes more dominant in short stack machine [67]. The most accurate prediction results can be obtained by the three-dimensional FEM with the transversal end effect considered.

However, this approach will significantly increase the computation time, especially in calculating the flux linkages of the LSRA [68]. A lot of solutions would be required at a wide range of excitation currents and translator positions. Besides, there is extra longitudinal end effect in the LSRA, due to the finite length of the stator stack [69]. Certain discrepancy is introduced between phases at both ends and the phases in the middle by the variation in flux distribution.

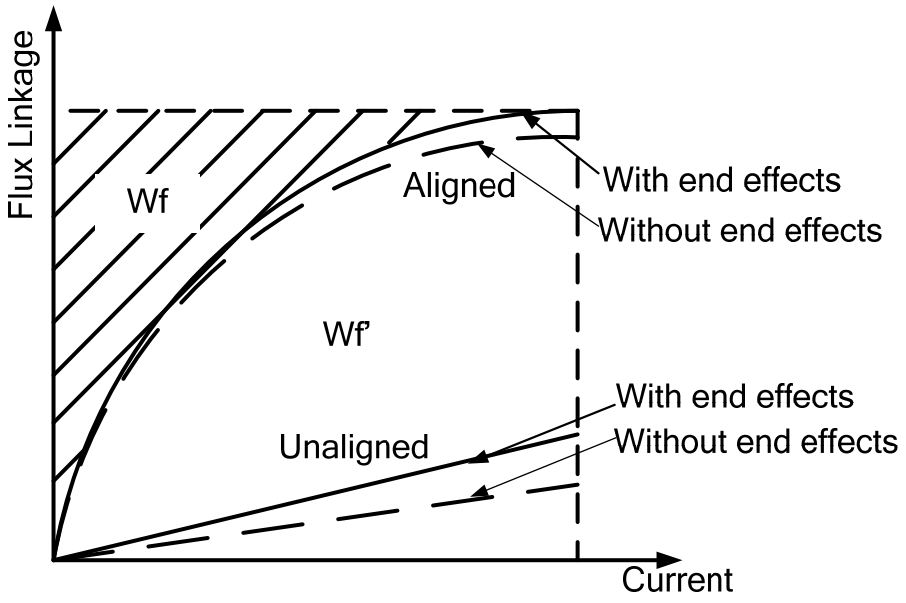

Fig. 4-1 Flux linkage with end effects

The qualitative sketches of flux linkage comparison between the situations with and without end effects are shown in Fig. 4-1. The solid flux linkage curves are calculated by assuming end-effects, and other two curves in dashed lines are calculated by neglecting two end-effects. It can be observed that the omission may reduce the energy conversion area and lowers the performance calculation. Since the longitudinal and transversal end effects would induce errors in estimating the performance characteristics of the LSRA, it is necessary to study their sensitivities to

machine parameters, such as geometric topology, stack length, excitation level and translator position.

4.1 Finite element method

The Ansoft electromagnetic field software is applied to investigate the end effects and to obtain the magnetic characteristics of LSRA with the consideration of saturation and mutual inductance, which are both ignored in the analytical method.

The first step is to build the analytical model of LSRA with specified dimension for finite element method. The three-dimensional model of double-sided LSRA with one phase winding is shown in Fig. 4-2. It can be observed that the stator stack length is quite short relative to the length of stator pitch. Hence, the end effects have to be considered if more accurate prediction is required. The two-dimensional FEA model, as shown in Fig. 4-3, is constructed from the YZ plane cross section of the three-dimensional model. The winding area is represented by rectangles around the stator poles. The translators are aligned with the excited stator poles in both models shown in the figures. By moving the translators along the motion direction, the solutions for flux linkage at different translator positions can be obtained. Next, a confined area around the analytical model is specified for the magnetic field computation. No magnetic flux lines are assumed to cross out of the area.

The second step is to specify the magnetic properties of each part of the model. For the stators and translators which are made of laminated silicon steel, a magnetization B-H curve considering saturation is assigned. For the winding area, material copper is assigned with unitary relative magnetic permeability. The rest of

space in the confined area is assigned as air.

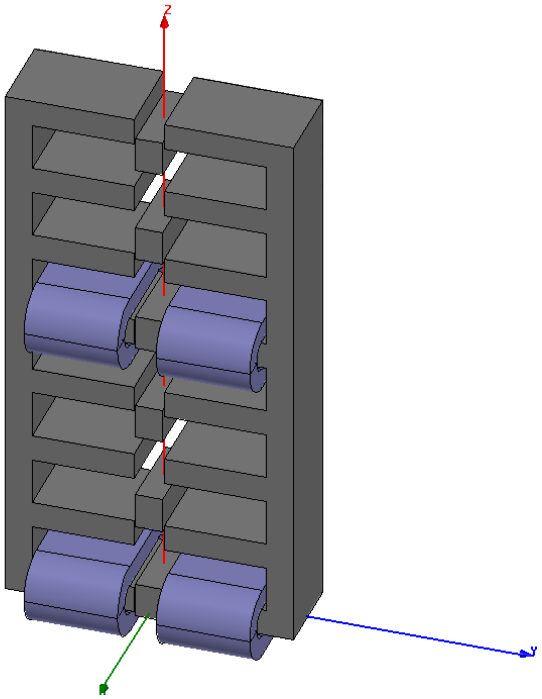

Fig. 4-2 Three-dimensional model of double-sided LSRA

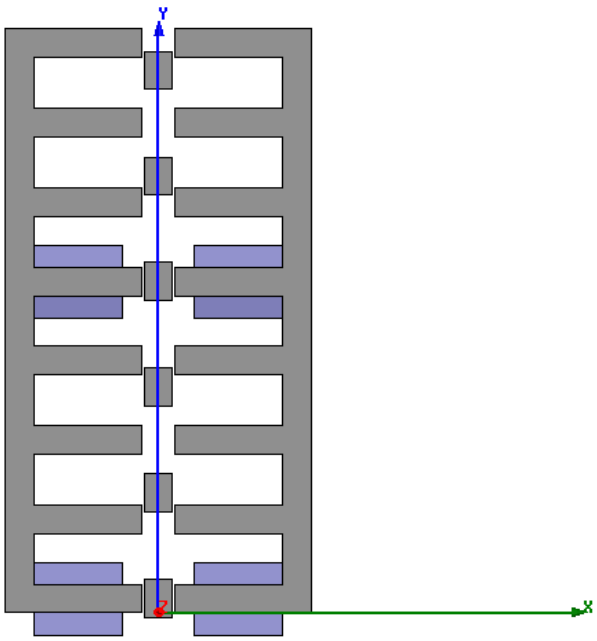

Fig. 4-3 Two-dimensional model of double-sided LSRA

The next step to solve the magnetic field is to add excitation to the windings of each phase. By varying the current density specified to the windings, different magnetic flux can be obtained. The directions of two winding excitations at the same stator side are opposite to ensure consistent flux in LSRA.

When the above settings are finished, a mesh is generated to link the physical description to the following numerical computation [70]. The confined area is separated into many smaller elements.

The magnetic field in two-dimensional analysis can be determined by computing the magnetic vector potential A over the cross section of the LSRA, and obtained by solving the nonlinear Poisson's equation in Cartesian coordinates [71]:

$$\frac{\partial}{\partial x}\left(\gamma\frac{\partial A}{\partial x}\right)+\frac{\partial}{\partial y}\left(\gamma\frac{\partial A}{\partial y}\right)=-J \tag{4-1}$$

where γ is the magnetic reluctance and J is the current density.

Once the magnetic potential is solved, the flux linkage per phase can be calculated by

$$\psi_{2D}=\frac{1}{i}\int_V \vec{J}\,\vec{A}\,dV=\frac{N}{S}\sum_{k=1}^{n}A_k S_k \tag{4-2}$$

where S is the area of phase winding. Note that the computed flux linkage in two-dimensional FEA is just the result for the cross section of LSRA, the total flux linkage equals to the product of the computed value and the stack length [72]:

$$\psi=l_s\cdot\psi_{2D} \tag{4-3}$$

4.2 Longitudinal End Effect

A fundamental difference between a rotary switched reluctance motor (RSRM) and an LSRA is the finite length of the magnetic and electric circuit of the LSRA in the direction of the travelling field [73]. The finite length of stator stack causes an unbalanced phase inductance, which is the so-called longitudinal end effect in LSRA. By applying the two-dimensional FEM, The performance characteristics of phase A at the end and phase B in the middle are obtained and illustrated in Fig. 4-4. There is certain discrepancy between these two phases. This effect must be carefully considered in evaluating the flux linkage per phase in high performance motion control.

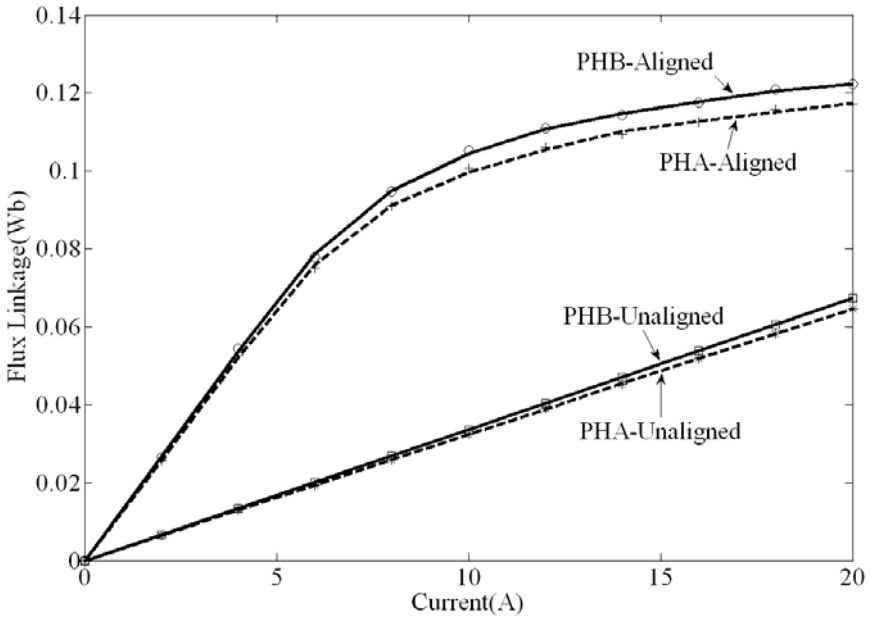

Fig. 4-4 Flux linkage comparison of phase A and phase B

The equivalent circuit approach is very useful for analyzing the cause of the longitudinal end effect. The disparity can be easily derived from the steady-state equivalent circuit. To simplify the analysis, transversal end effect is neglected here.

Hence, two-dimensional FEA is adequate to verify the analysis and determine the sensitivities to machine parameters.

The distribution of the magnetic flux lines of two phases in unaligned position are shown in Fig. 4-5. It is observed that the leakage flux lines of phase B pass through the stator slot to both adjacent stator poles and enclose the path through the stator back iron, while the end phase A has only one adjacent stator pole and the leakage flux lines at this side have to be enclosed with air. The longer is the leakage flux path in stator, the higher is the phase inductance. Therefore, the inductance of phase A is smaller than that of phase B. The same situation happens in the aligned position and the in-between positions.

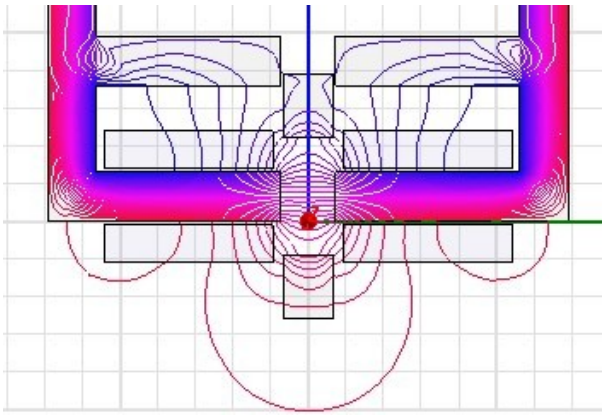

(a) Phase A

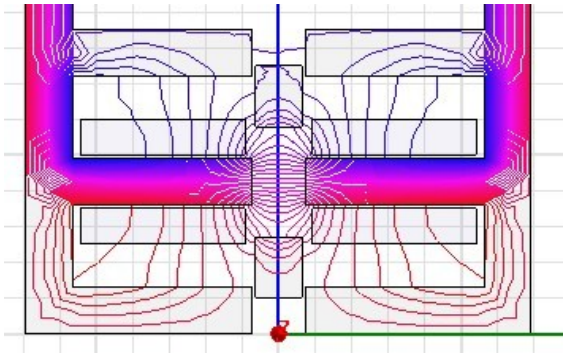

(b) Phase B

Fig. 4-5 Magnetic flux distribution

In order to illustrate the sensitivities to machine parameters, a 2D FEA is used to study the longitudinal end effect. The inductance variation with excitation and translator position of per phase are calculated and compared.

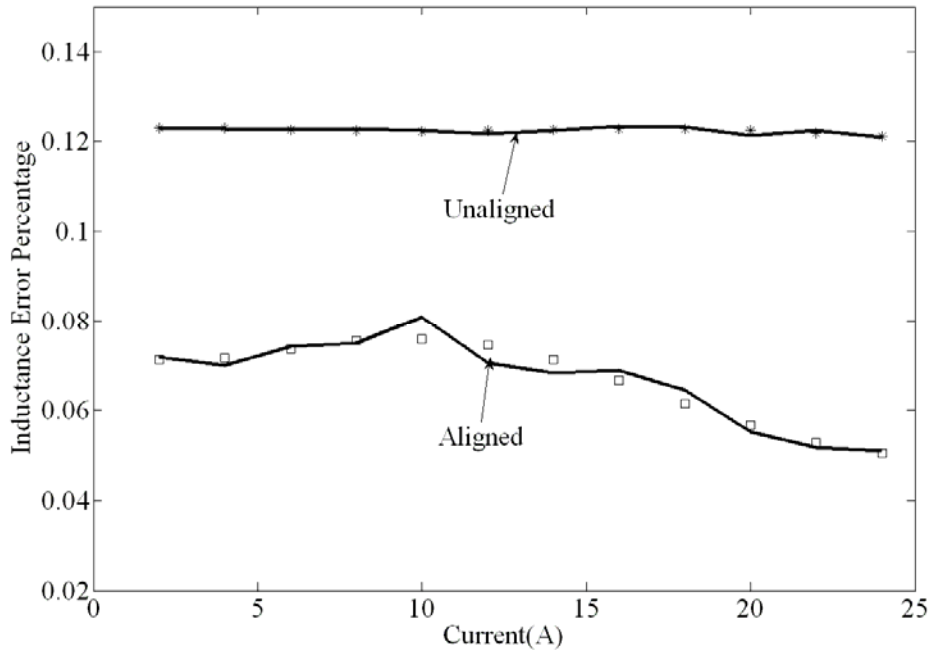

Fig. 4-6 Percentage variation of Inductance error with excitation current

4.2.1 Inductance variation with excitation current

Fig. 4-6 shows the error percentage of inductance between phase A and phase B. It is basically constant in the unaligned position. It can be observed that the inductance of phase A, over the excitation range, can be decreased by up to 13%, owing to the longitudinal end effect. The error percentage of inductance in aligned position is slightly decreased as the excitation current is increased. Owing to the small air-gap in aligned position, the error in aligned position remains small over the whole of the excitation range.

4.2.2 Inductance variation with translator position

The variation of error percentage with translator position under rated excitation is illustrated in Fig. 4-7. Zero axial position represents the fully unaligned position. It can be seen that the error percentage reached a peak value near the unaligned position, and then gradually decreased as the translator pole moves into alignment with the excited stator pole. This is due to the fact that when the poles are not saturated the leakage flux decreases as the pole overlap increases.

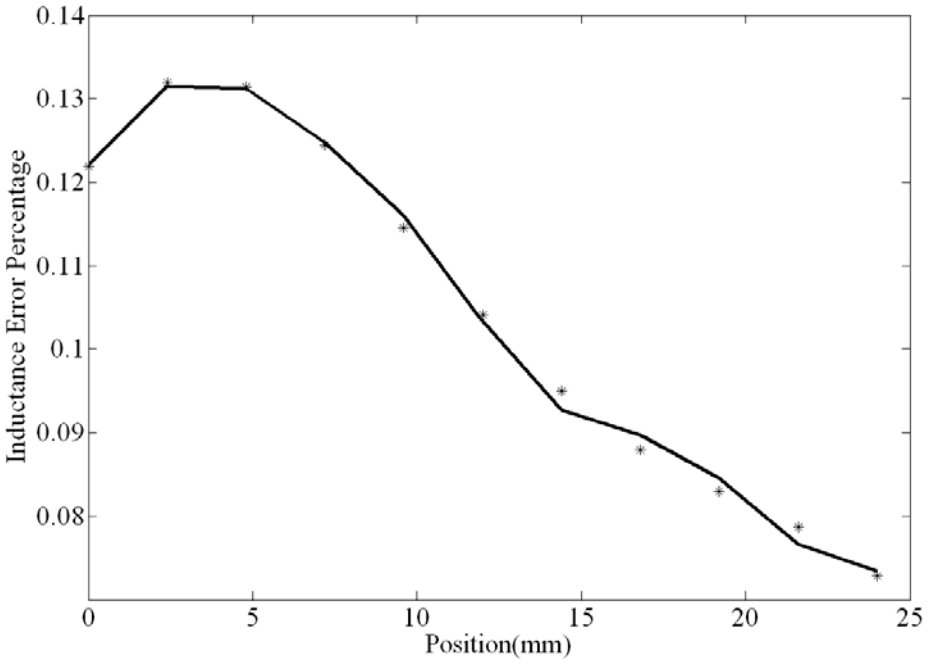

Fig. 4-7 Percentage variation of inductance error with translator position

4.2.3 Solutions

The longitudinal end effect causes an unbalanced phase characteristics and brings a certain discrepancy in predicting the actuator performance. The easiest way to compensate the decrease of inductance of the end phase is to add an extra pair of stator poles at both ends of the stator. However, this solution may increase the length of stator and is not suitable for an application that has limited space.

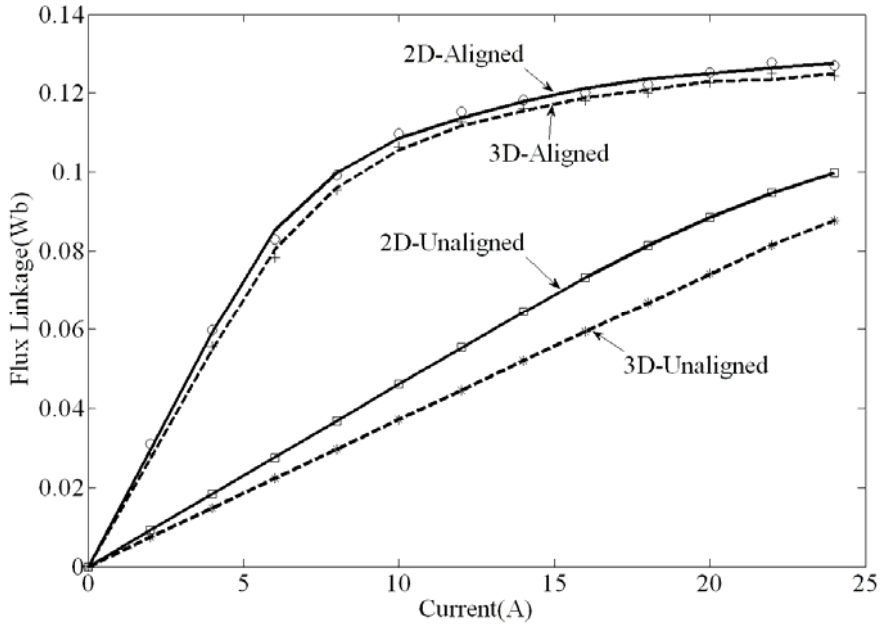

Fig. 4-8 Flux linkage comparison of 2D and 3D FEA

4.3 Transversal End Effect

2D FEA is widely used to verify the design and to predict the performance, for its simplicity and fast computation. However, all practical machines are three-dimensional. A two-dimensional model based analysis is inadequate in many cases due to the omission of transversal end effects. It can be observed from Fig. 4-8

that the values of flux linkage are underestimated by 2D FEA; hence a reduced energy conversion area is obtained. Therefore, it is necessary to identify the relationships between 2D and 3D FEA results and determine the sensitivity of transversal end effects to actuator parameters.

There are three different causes that contribute to the transversal end effects: axial fringing, end-winding flux and anisotropy of lamination [74]. Axial fringing exists at both ends of the machine stack, and magnetic flux tends to bulge out axially from the stator pole ends into the translator pole ends. The inductance in unaligned position is considered to be increased by 20-30% owing to the fringing effect [75]. As the phase coil is shaped like a race ring, there is conductor region that extends beyond both stack ends. The end winding inductance may account for a significant percentage of the phase inductance, especially for machine of short stack length, or long-pitched windings.

Besides the flux flowing in the plane of the laminations, there is flux flow normal to the laminations which bring significant eddy current loss. Its effective permeability is thought to be much less than that of flux in the plane laminations. Therefore, the anisotropy and directional permeability have to be considered in finite element analysis. The three-dimensional solution can be corrected by specifying a packing factor, while the two-dimensional analysis requires a more complex method by scaling the original B-H curve according to the packing factor [76].

In order to identify the transversal end effect and analyze its sensitivity to actuator parameters, three-dimensional FEA was carried out and compared with the results from two-dimensional FEA solutions. The transversal end effect is proved to

be highly dependent on the translator position, excitation level and stack length.

4.3.1 Flux Linkage

The variation of error percentage in flux linkage at aligned and unaligned positions with excitation current is demonstrated in Fig. 4-9. In the unaligned position, the error between 2D and 3D FEA is almost constant at 20% during low excitation, and begins to decrease in saturation region. This is because, at low excitation, the reluctance of air-gap at unaligned position accounts for most of the magnetic circuit reluctance. While in the aligned position, the error percentage is gradually decreased as the excitation increases. This is due to the fact that the permeability of iron core is high at low excitation, and hence the end winding has greater impact on the flux linkage of phase winding.

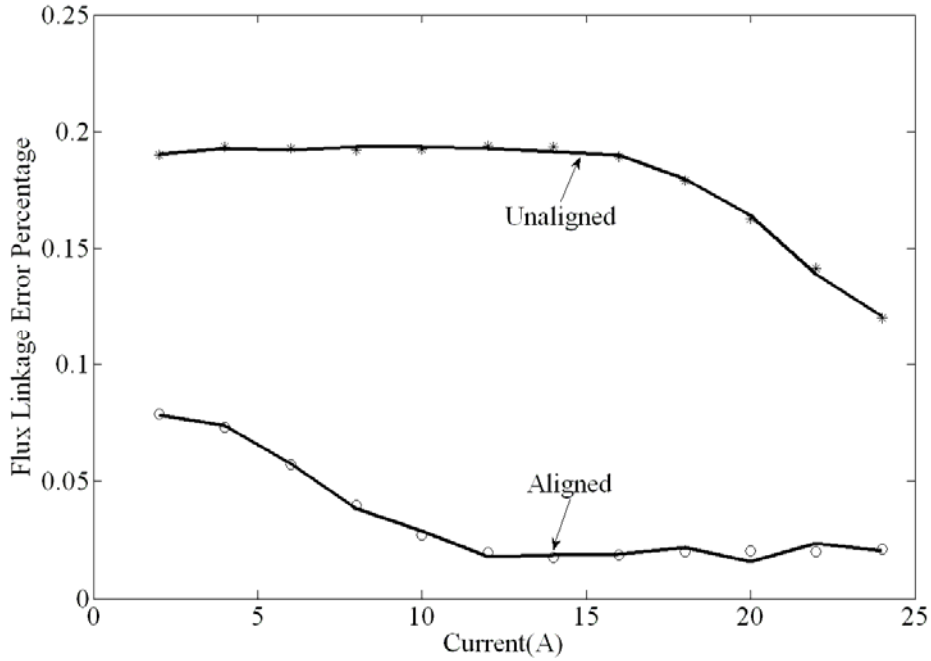

Fig. 4-9 Percentage variation of flux linkage error with excitation current

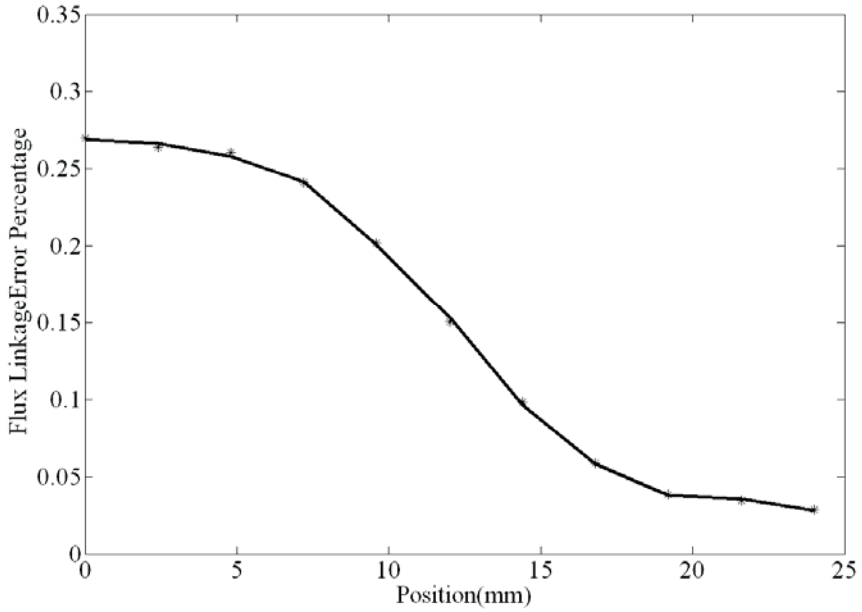

Fig. 4-10 Percentage variation of flux linkage error with translator position

Fig. 4-10 illustrates the variation of error percentage with translator position due to the transversal end effect. The error percentage of flux linkage is maximal at more than 25% in unaligned position, then decreases as the overlap of the poles increases, and reaches the lowest value in the fully aligned position. This is because the saturation is getting severe as translator pole moves into alignment, and the permeability of magnetic core is reduced gradually. Therefore the end winding flux is reduced.

4.3.2 Stack Length

The error incurred in 2D FEA is considered to be highly dependent on the stack length owing to the transversal end effect. Fig. 4-11 illustrates the variation of error percentage in flux linkage as the stack length increases. It can be observed that

significant error incurred at unaligned position when the stack length is very short and the accuracy is improved obviously as the stack length is getting longer. This is due to the fact that the end winding is dominant in the phase winding conductor when the stack length is short. The error percentage at aligned position is slightly deceased and maintains at a relatively low rate.

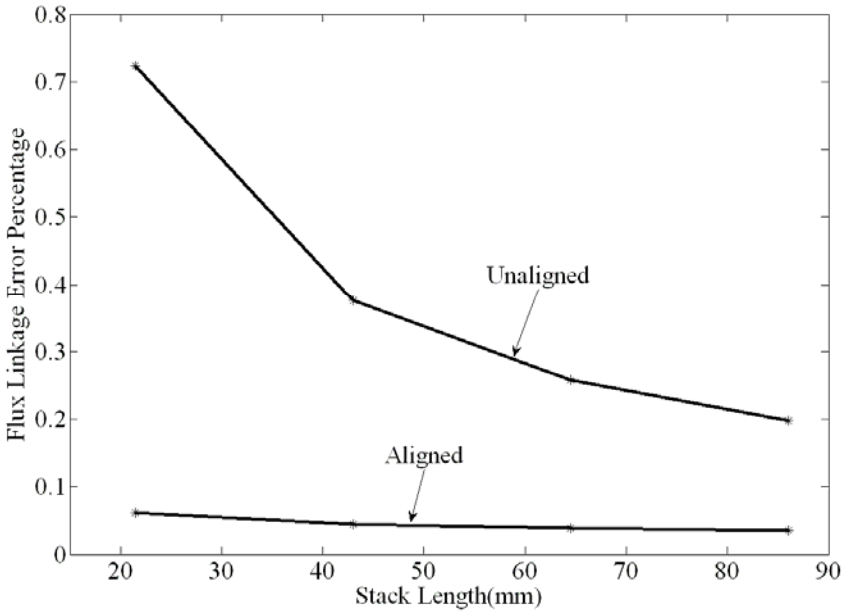

Fig. 4-11 Percentage variation of flux linkage error with stack length

4.3.3 Translator Stack Length

In some applications, the stack length of the translator is longer than that of the stator, resulting in a variation in the distribution of transversal flux. The unequal axial length is hard to be reflected in 2D FEA solutions and incurs a certain error in the performance prediction. The trend of impact can be examined by modeling the transversal cross section to obtain the variation of end winding inductance. As shown in Fig. 4-12, the inductance is gradually increased as the translator stack

extents beyond the stator stack. This is because the end winding flux links more with the translator and the variation of end fringing distribution. Therefore, the error in flux linkage owing to the unequal stack length is increased as the translator stack length is getting longer.

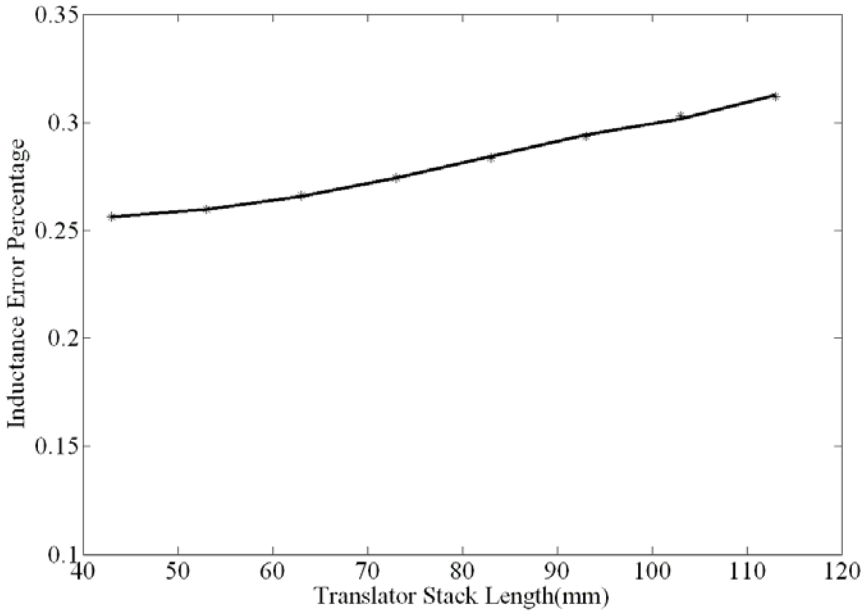

Fig. 4-12 Percentage variation of inductance error with translator stack length

4.3.4 Static Force

It can be observed from Fig. 4-13 that at high excitations and towards alignment a higher value of static torque was predicted by 2D model solutions. This is due to the fact that in positions close to alignment the radial component of flux produced by end windings may be more dominant than tangential component.

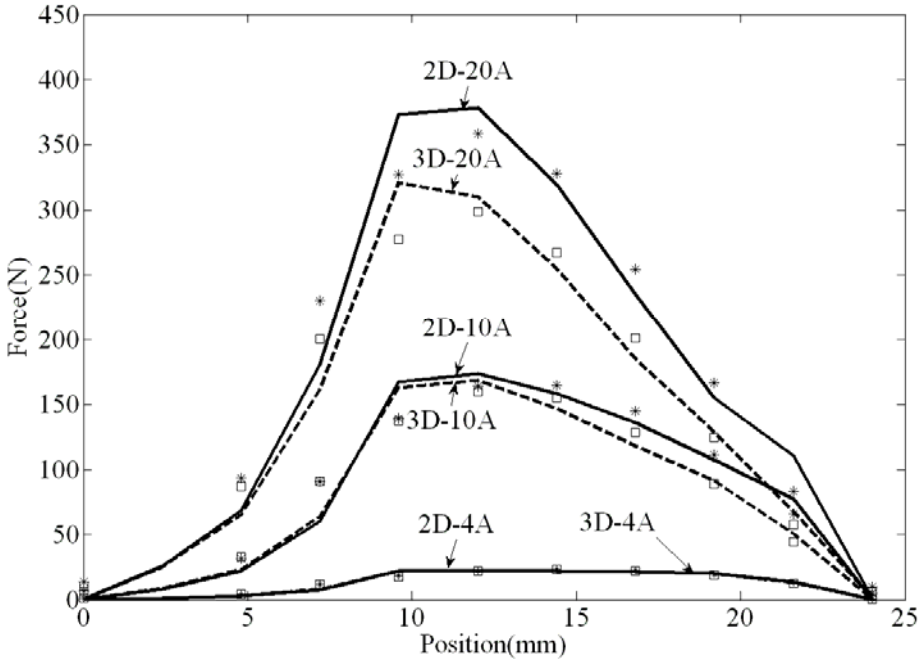

Fig. 4-13 Static force comparison of 2D and 3D FEA

4.4 FEM Verification

Since the discrepancies between two-dimensional and three-dimensional FEM are analyzed, the preliminary design by analytical method in the previous chapter is just verified by two-dimensional FEM to save the computation time. The flux linkages and forces under excitation currents ranging from 2A to 24A are obtained, and the translators are varied from fully unaligned position to fully aligned position at a step of 2mm, as shown in Fig. 4-14 and Fig. 4-15. It is observed that the characteristics of preliminary design meet the requirements from the active suspension system. The flux density and distribution of flux lines at fully unaligned position, intermediate position and fully aligned position are demonstrated in Fig.

4-16 and Fig.4-17, respectively. All figures are obtained under the excitation current of 12A. It can be observed that the flux density in stator poles is increasingly high as the translator poles move towards the aligned position, and there is severe local saturation in the pole tips at the intermediate position where a small portion of stator and translators poles are overlapped. The situation can be observed more explicitly from the distribution of flux lines in Fig. 4-17 (b).

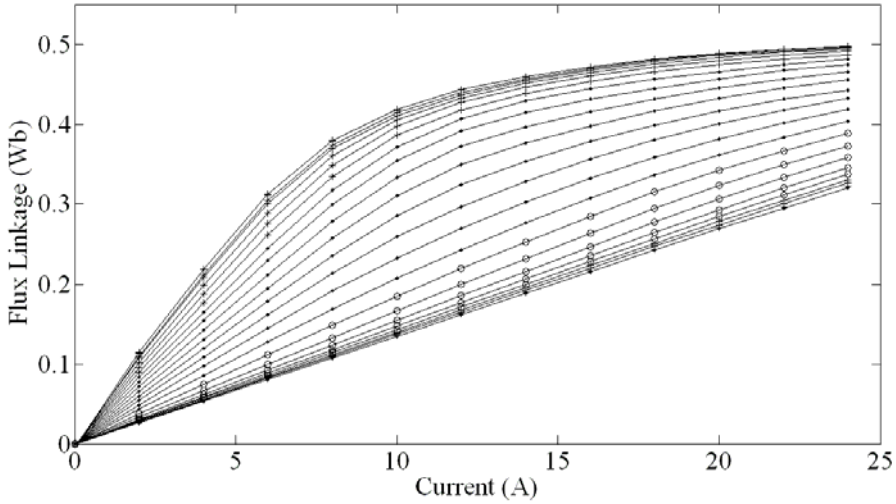

Fig. 4-14 Flux linkage characteristics

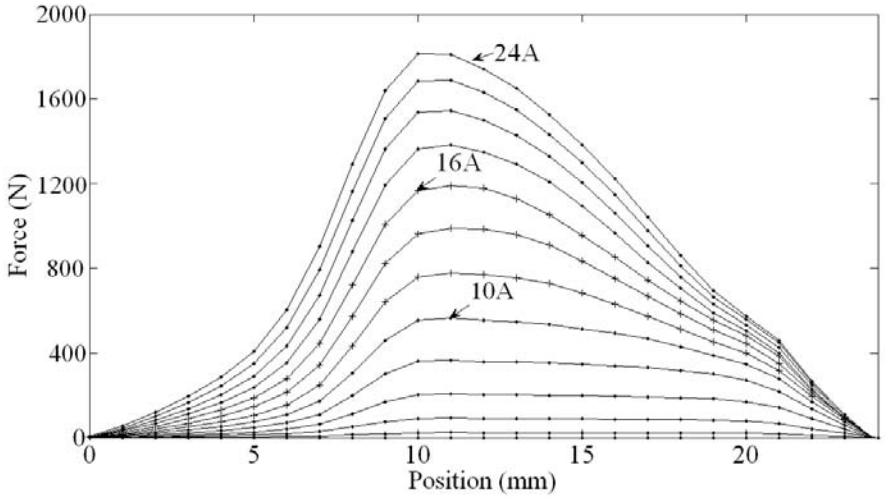

Fig. 4-15 Force characteristics

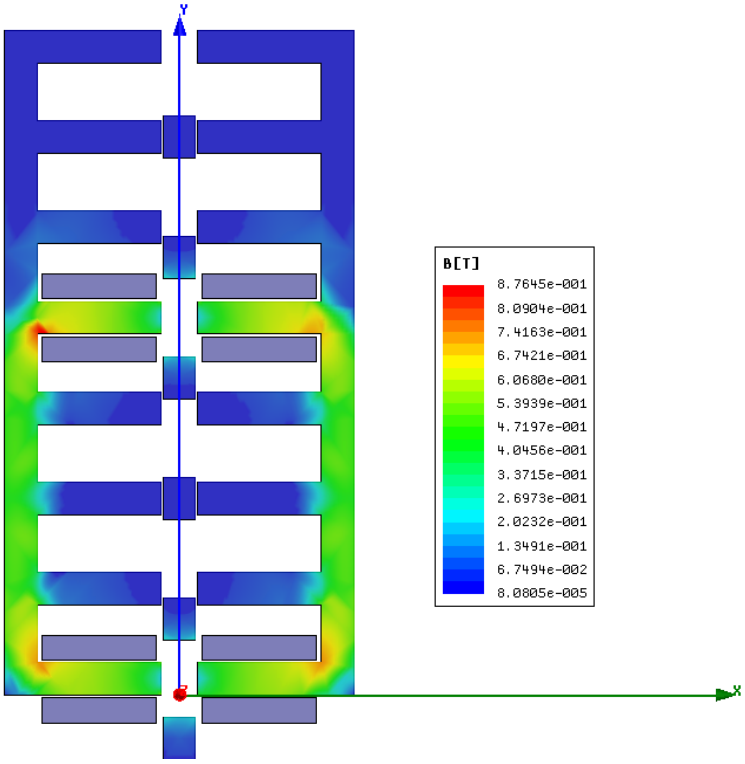
Y
X
B[T]
8.7645e-001
8.0904e-001
7.4163e-001
6.7421e-001
6.0680e-001
5.3939e-001
4.7197e-001
4.0456e-001
3.3715e-001
2.6973e-001
2.0232e-001
1.3491e-001
6.7494e-002
8.0805e-005

(a)

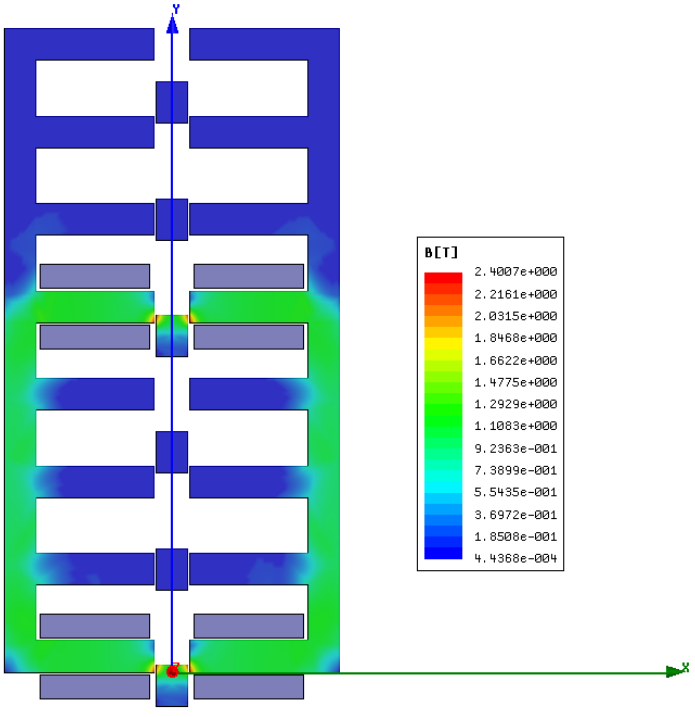
Y
X
B[T]
2.4007e+000
2.2161e+000
2.0315e+000
1.8468e+000
1.6622e+000
1.4775e+000
1.2929e+000
1.1083e+000
9.2363e-001
7.3899e-001
5.5435e-001
3.6972e-001
1.8508e-001
4.4368e-004

(b)

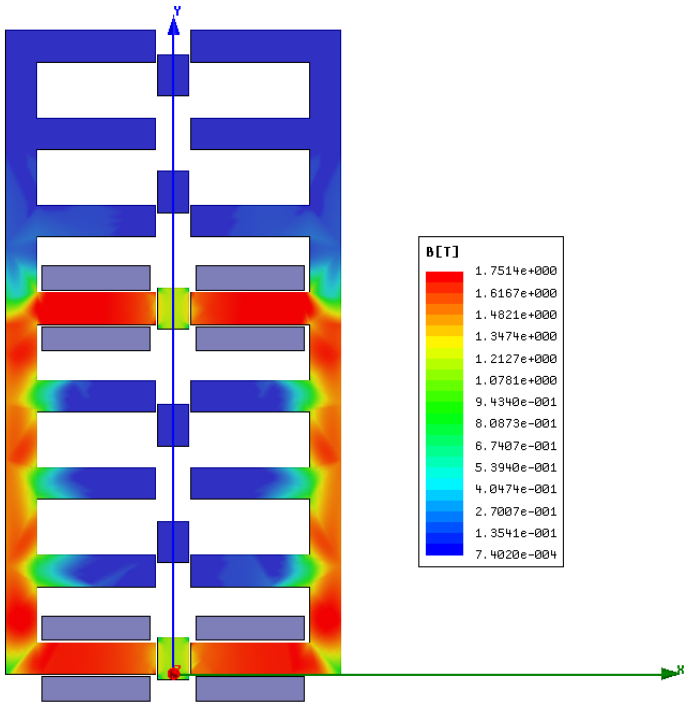

(c)

Fig. 4-16 Flux density (a) Unaligned position (b) Intermediate (c) Aligned

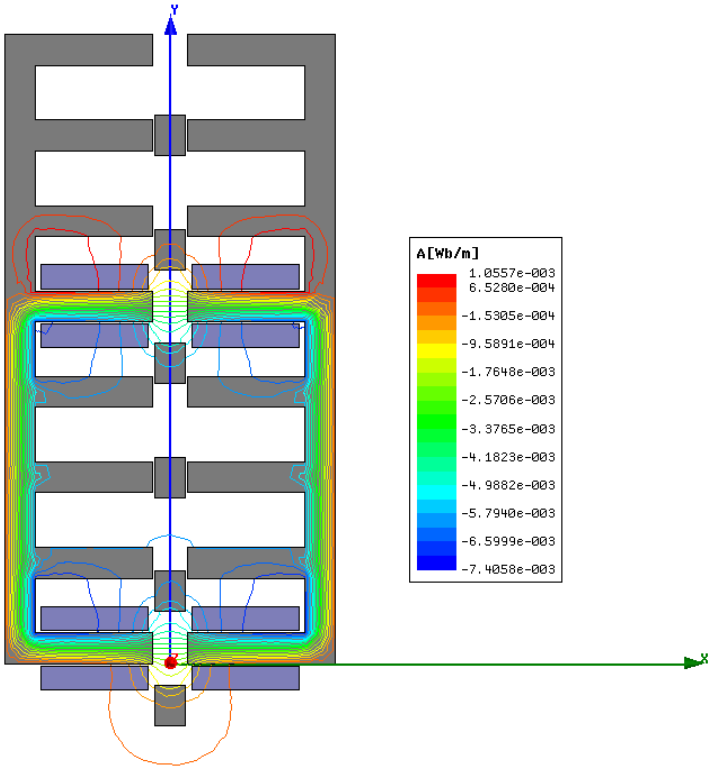

(a)

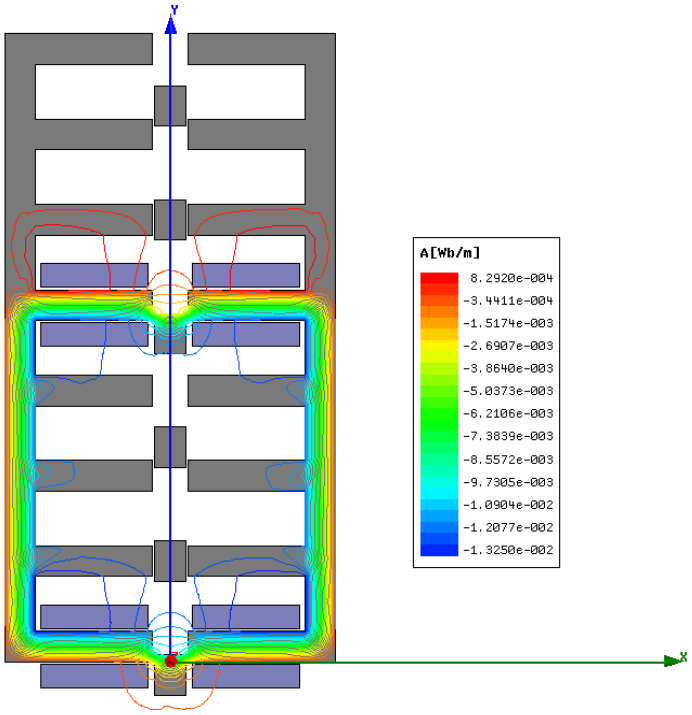

(b)

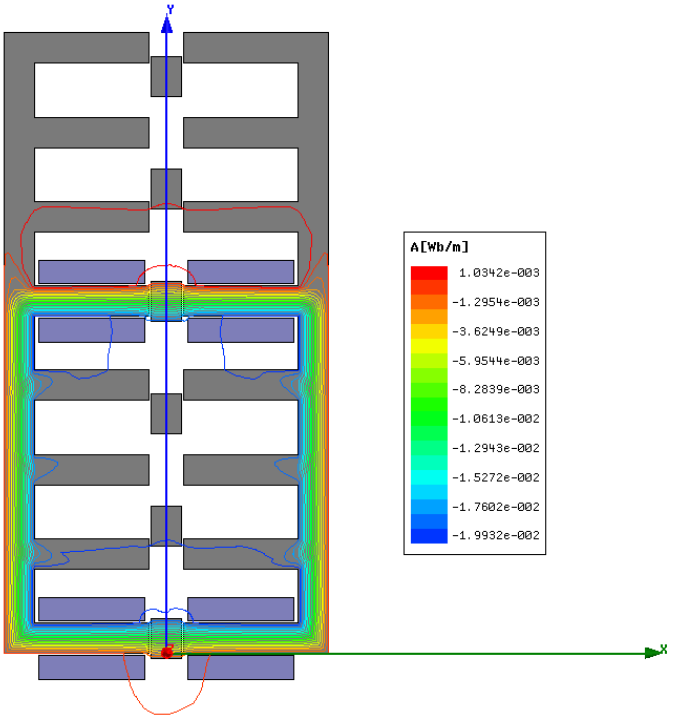

(c)

Fig. 4-17 Flux lines (a) Unaligned position (b) Intermediate (c) Aligned

4.5 Summary

The impact of longitudinal end effect in LSRM is investigated in this chapter. A simple but practical solution is presented to compensate the phase imbalance introduced by the longitudinal end effect. Sensitivity analysis to machine parameters of both end effects is carried out by using two and three-dimensional FEM. The results obtained from FEM present the variation of estimation error with excitation current at different translator position. By understanding the impact of both end effects, the verification of preliminary design will be more accurate and less time-consuming, and the operation performance of LSRM can be further improved.

Chapter 5

Multi-objective optimization of the LSRA

Linear switched reluctance actuator (LSRA) is considered as an attractive alternative to other types of high performance actuators in active suspension system (ASS), due to its simple and robust structure, high reliability and fast dynamic response. However, it suffers from the disadvantage of high force ripple and resultant acoustic noise [77]. The problem is more severe in direct-drive servo system. For the application in ASS, the force ripple would cause significant impact on the ride comfort. Therefore, the configuration of LSRA should be optimized to achieve reduced force ripple and higher average force in a compact volume before it is applied in ASS.

There are two major approaches to reduce the force ripple: geometry design optimization and control technology improvement [78]. The geometry optimization is realized by adjusting the stator and translator pole structures. It is considered as the most effective way to alleviate the inherent problem. Various methods have been studied and reported in previous literatures, but the practical limitation is seldom taken into consideration. The control method is optimized by changing the control

parameters, such as turn-on and turn-off positions, and excitation current. However, this approach would also reduce the average force as the force ripple is minimized [79].

This chapter describes a multi-objective optimization method for the double-sided LSRA to obtain higher average force, reduced force ripple and higher average force per core volume. The effects of stator and translator pole width on three objectives above are investigated by using finite element analysis (FEA). Then the optimal combinations of stator and translator pole width under various suspension volume limitations are obtained. Practical constraints, such as actuator volume limitation, winding area, are considered in the optimization procedure.

5.1 Design Optimization Aspects

5.1.1The optimization Criterions:

Three criterions are selected as optimization objectives, which are the average force, the force ripple and the average force per core volume. The force characteristic of the LSRA can be evaluated by considering the energy conversion procedure. If there is only one phase energized at a time, the instantaneous force can be obtained by

$$F_{inst} = \frac{\partial W_{co}(i,x)}{\partial x} \tag{5-1}$$

where W_{co} is the coenergy, which is proportional to the area between two magnetization curves.

$$W_{co}(i,x) = \int_0^i (\lambda_{x+dx}(i,x) - \lambda_x(i,x))di \tag{5-2}$$

Then we can obtain the average force by integrating the instantaneous force over one cycle as

$$F_{ave} = \frac{1}{\tau}\int_0^{\tau} F_{inst}\,dt \tag{5-3}$$

where τ represents one translator pole pitch.

It can be observed from Fig.5-1, the minimum force occurs at the intersection point of two successive phases. The force dip is then defined as the difference between the maximum and minimum force.

$$F_d = F_{\max} - F_{\min} \tag{5-4}$$

Hence, we can define the force ripple as

$$F_R = \frac{F_d}{F_{\max}} \times 100\% \tag{5-5}$$

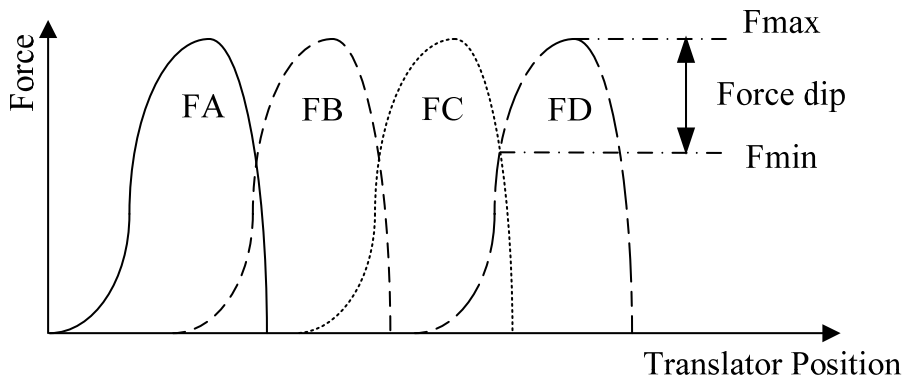

Fig. 5-1 Force ripple characteristic

The actuator core volume V_{core} is calculated by

$$V_{core} = V_s + V_t \tag{5-6}$$

where V_S represents the volume of stator core and V_t represents the volume of

translator core, then the average force per core volume can be obtained by

$$FV = \frac{F_{ave}}{V_{core}} \tag{5-7}$$

Assuming the density of core material is D, we can further obtain the average force per translator core mass as

$$FM = \frac{F_{ave}}{V_t \cdot D} \tag{5-8}$$

5.1.2 The Constraints

The stator and translator pole width is critical to the actuator performance, and they are selected as the optimization variables. According to the feasible triangle of rotary switched reluctance motor derived by Lawrenson [80], the corresponding constraints on stator and translator pole width in LSRA are obtained. The combinations of the pole width are limited in the triangle of ABD, as is shown in Fig.5-2.

Thus, the range of stator pole width is

$$\frac{l}{N_{ph} \cdot N_{tp}} < w_s < \frac{(N_{ph} - 2) \cdot l}{N_{ph} \cdot N_{tp}} \tag{5-9}$$

and the range of translator pole width is

$$\frac{l}{N_{ph} \cdot N_{tp}} < w_t < \frac{l}{N_{tp}}(1 - \frac{1}{N_{ph}}) \tag{5-10}$$

Moreover, the translator pole width should be valued larger than or at least equal to the stator pole width [81], expressed as

$$w_{tp} \geq w_{sp} \tag{5-11}$$

where w_{sp} and w_{tp} represent the stator and translator pole width, respectively.

In addition to the constraints by feasible triangle shown in Fig. 5-2, the stator pole width is limited by the available suspension volume. It is due to the fact that with a fixed stator pole pitch, the available winding area and thus the available magnetic motive force (MMF) are decreased with the increase of stator pole width. In order to accommodate the coil, the stator pole height has to be extended, which consequently enlarge the volume of LSRA according to the configuration.

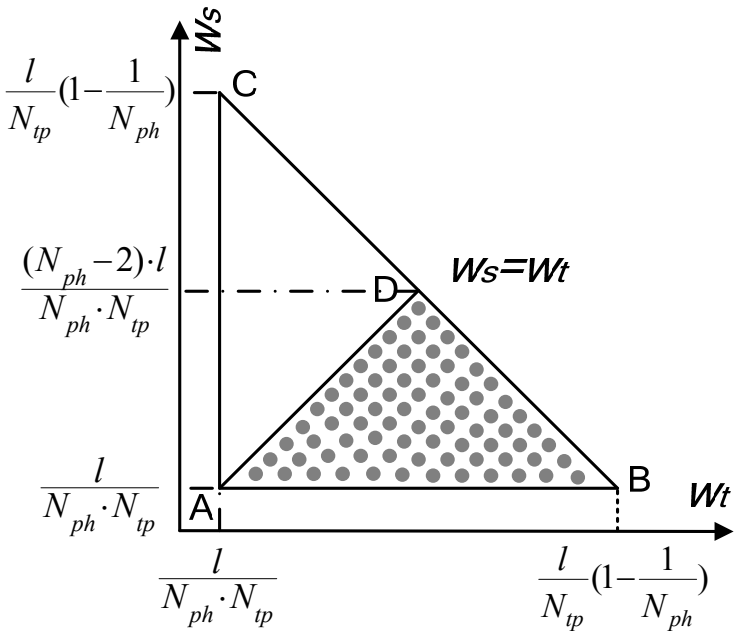

Fig. 5-2 The Feasible Triangle of the LSRA

5.2 Effect analysis of pole width

5.2.1 Effects of stator pole width

In order to analyze the effects of both pole widths, 2D FEM with end effects correction is conducted. The effects of stator pole width on average force, force

ripple and average force per core volume are illustrated in Fig. 5-3. It can be observed from Fig. 5-3(a), (b) that the average force and force ripple are improved significantly with the increase of stator pole width. For various translator pole widths, the variation of effects shows slight differences at different stator pole width ranges, but follows the same trend. It means better performance can be obtained with wider stator pole at fixed translator pole width, if the average force per core volume is not taken into consideration.

Fig. 5-3(c) shows the core volume variation with the increase of stator pole width. The core volume increases more significantly than the average force. It can be observed from Fig. 5-3(d) that the average force per core volume turns out to be decreasing with the increase of stator pole width. It means the LSRA with narrower stator pole has higher force density. Therefore, a compromise among three objectives is needed during the optimization procedure of stator pole width.

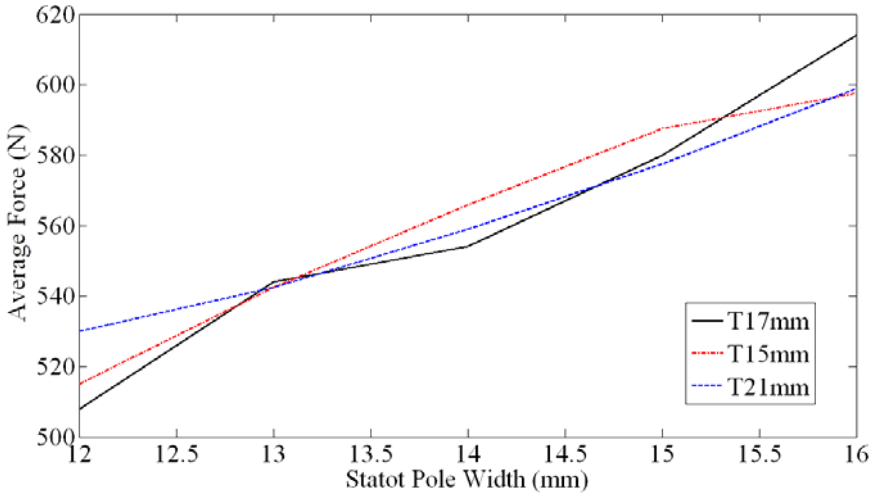

(a)

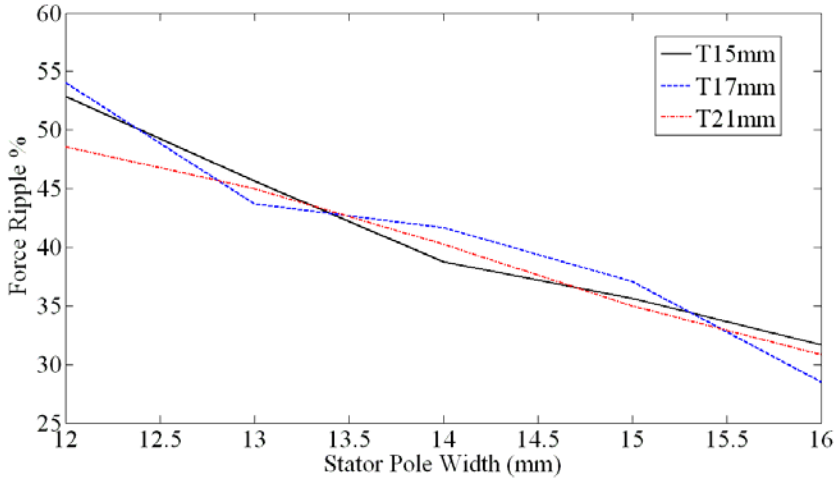

(b)

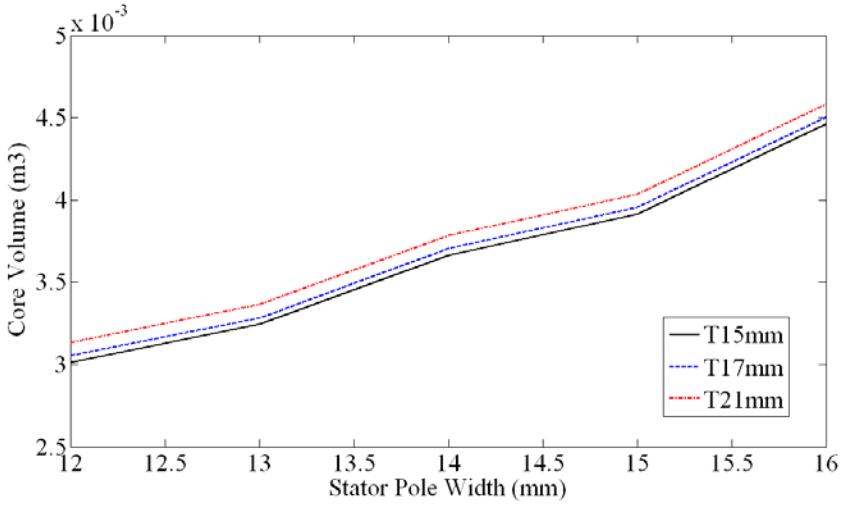

(c)

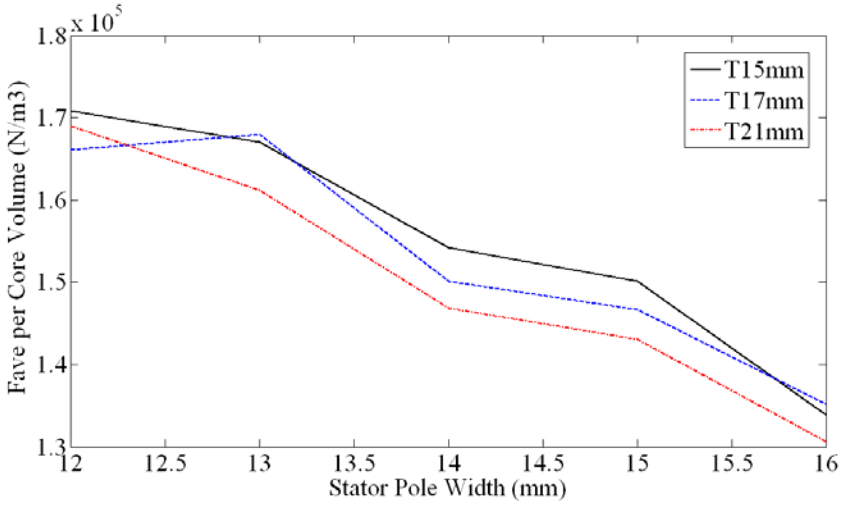

(d)

Fig. 5-3 Effects of stator pole width

5.2.2 Effects of translator pole width

To adjust the translator pole width is considered to be easier than to change the stator pole width, because it is irrespective to the space limit, MMF [82]. However, the impact on actuator performance is less evident than the stator pole width.

Fig. 5-4 depicts the effects of translator pole width on average force, force ripple and average force per core volume. Compared with the effects of stator pole width, there is no evident trend for each objective with the increase of translator pole width. It can be observed from Fig. 5-4(a), (b) that the average force and force ripple fluctuate slightly around a specific value, which is mainly determined by the stator pole width. For various stator pole width, the effects of translator pole width exhibit different characteristics. Take average force for instance, for a specific translator pole width at 17mm, the value of average force reaches a peak when the stator pole width is 16mm, whereas it decreased to the lowest point when the stator pole width is 14mm.

As shown in Fig. 5-4(c), the core volume invariably but slightly increases with the increase of translator pole width. It is because the volume of translator accounts for a small proportion of the core volume. Moreover, the influence of translator pole width on suspension volume can be negligible.

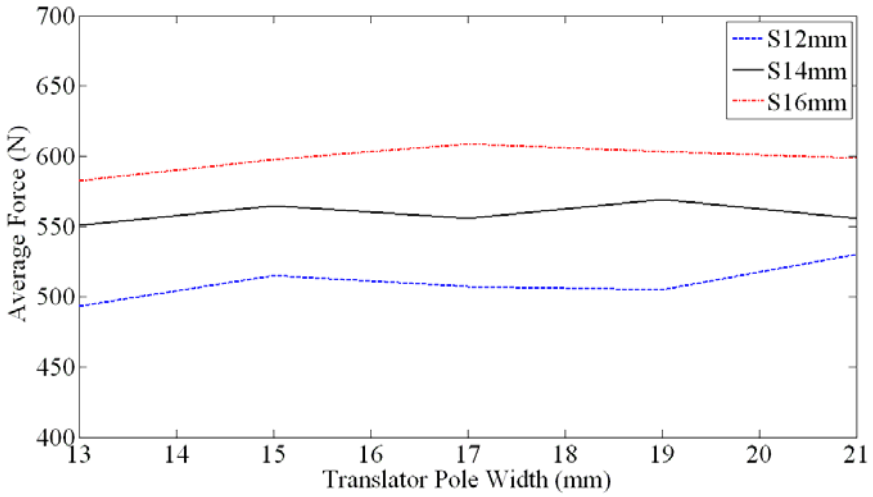
S12mm
S14mm
S16mm
Average Force (N)
700
650
600
550
500
450
400
13
14
15
16
17
18
19
20
21
Translator Pole Width (mm)

(a)

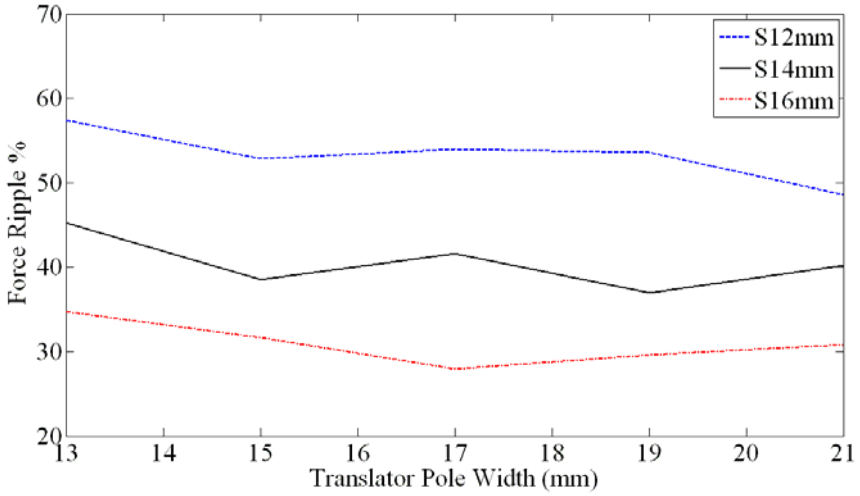
S12mm
S14mm
S16mm
Force Ripple %
70
60
50
40
30
20
13
14
15
16
17
18
19
20
21
Translator Pole Width (mm)

(b)

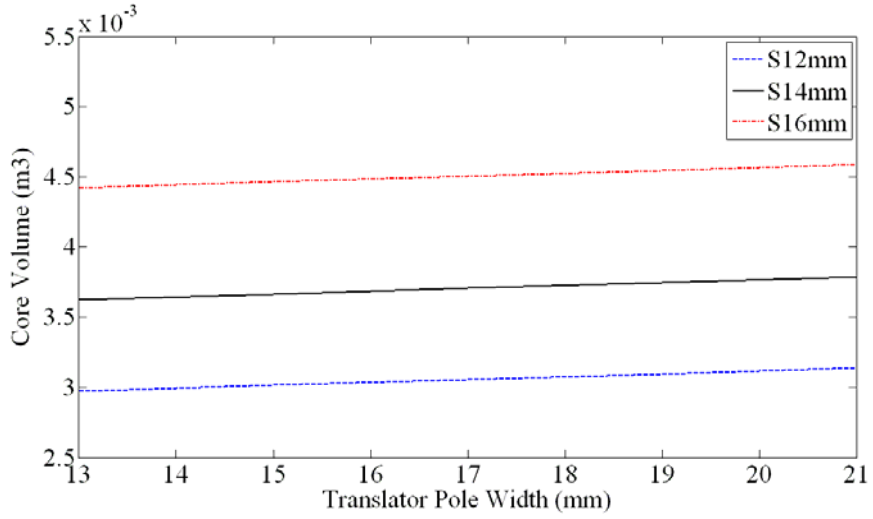
x 10-3
S12mm
S14mm
S16mm
Core Volume (m3)
5.5
5
4.5
4
3.5
3
2.5
13
14
15
16
17
18
19
20
21
Translator Pole Width (mm)

(c)

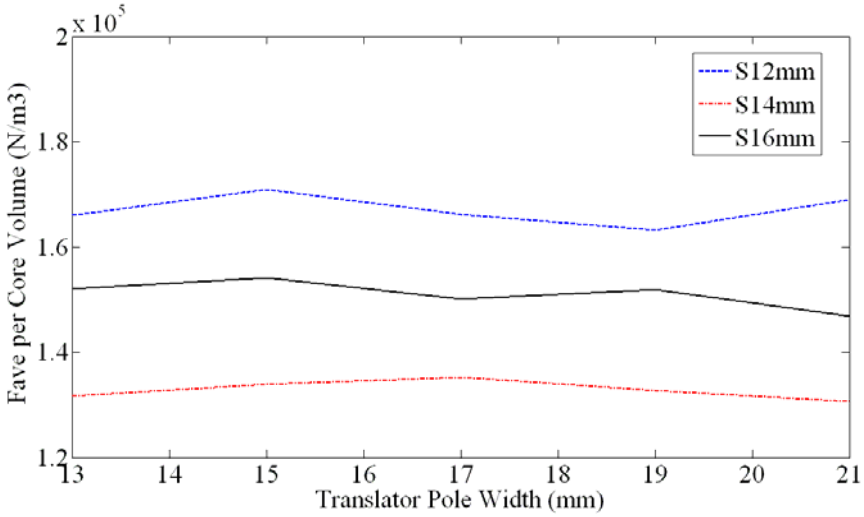

(d)

Fig. 5-4 Effects of translator pole width

5.3Multi-objective Optimization

5.3.1 Optimization function with multiple objectives

The design objective of LSRA in active suspension system is to achieve high average force, low force ripple and high force density. However, the optimal values of stator and translator pole width are varied to achieve each single objective, as is discussed in Section 5.2. There is no single pair of stator and translator pole width to simultaneously maximize the average force, minimize the force ripple and maximize the average force per core volume.

Therefore, a multi-objective function that contains three objectives is proposed. The priority of each objective is realized by introducing the weight factor. The objective function is adjustable to meet different requirements by modifying the individual weight factor of each objective. The multi-objective function can be expressed as

$$F_{obj} = w_F \frac{F}{F_m} - w_R \frac{FR}{FR_m} + w_V \frac{FV}{FV_m} \tag{5-12}$$

$$w_F + w_R + w_V = 1 \tag{5-13}$$

$$F_m = \max\{F\} \tag{5-14}$$

$$FR_m = \max\{FR\} \tag{5-15}$$

$$FV_m = \max\{FV\} \tag{5-16}$$

where F_{obj} is the multi-objective function, w_F, w_R and w_V denote the weight factor of the average force, force ripple and average force per core volume, respectively. F_m, FR_m and FV_m denote the base value of corresponding objective.

It can be observed that the value of objective function depends on the ratio of individual objective value to its base value and weight factor, and it becomes larger with the increase of average force and force density and decrease of force ripple. Thus, the optimization function with multiple objectives can be given by

$$F_{opt}(w_s, w_t) = \max\{F_{obj}\} \tag{5-17}$$

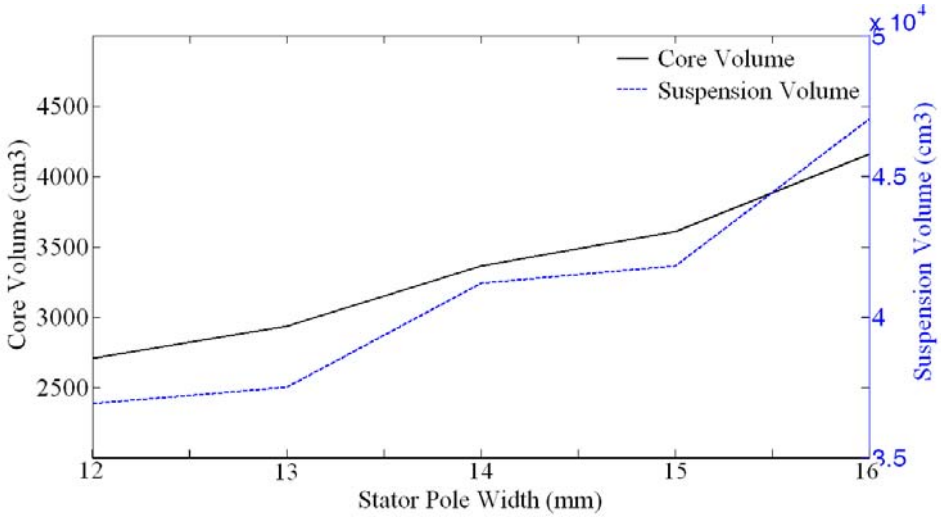

Fig. 5-5 Suspension volume

5.3.2 Optimization under constraints on suspension volume

The primary requirement for the design of the LSRA is the volume of active suspension unit. It must be compact enough to fit into the corner between the vehicle body and the wheel. Based on our measurements, the maximum space available for the suspension is no more than 300mm×300mm×600mm. As we discussed before, the suspension volume depends on the selection of stator pole width of the LSRA. Therefore, to meet the volume constraint, the value of stator pole width should be less than 16mm, as is shown in Fig. 5-5. If the limitation of suspension volume is further reduced to 250mm×250mm×600mm, the upper limit of stator pole width is reduced to 13mm. The translator pole width is considered to have little impact on suspension volume, but influences the core volume and weight of the LSRA.

5.3.3 Results of multi-objective optimization

Various combinations of weight factor are implemented during the optimization procedure. By adjusting the weight factor, we can decide which objective has high priority in optimization. Fig. 5-6 illustrates the variation of objective function with equal priority to three objectives. Three weight factors are assigned to 1/3 in this optimization. The change of objective function with priority in average force is shown in Fig. 5-7. The weight factor of average force is assigned to 0.7, which occupies 70 percent proportion of the total weight. It can be observed that the distribution of objective function is different from the results of that with equal priority. Fig. 5-8 shows the variation of objective function with priority in force ripple. Also, 70 percent of proportion of the total weight is assigned to this objective.

Similar distribution of objective function with average force is presented, but the value is different. The result of objective function with priority in average force per core volume is demonstrated in Fig. 5-9. The weight factor of force density accounts for 70 percent in the optimization. The distribution of objective function is totally different with the previous objective functions. It means the optimal value of stator and translator pole width varies with the different combination of weight factor. In another way, the optimal structure of LSRA depends on the priority of optimization objective.

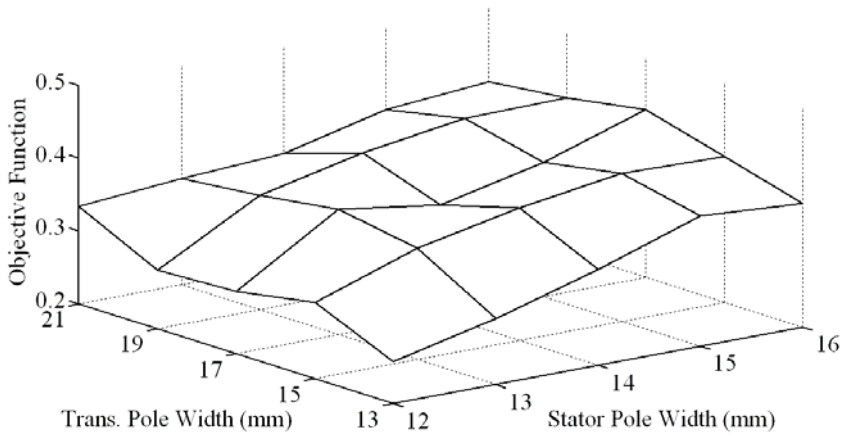

Fig. 5-6 Objective function with equal priority

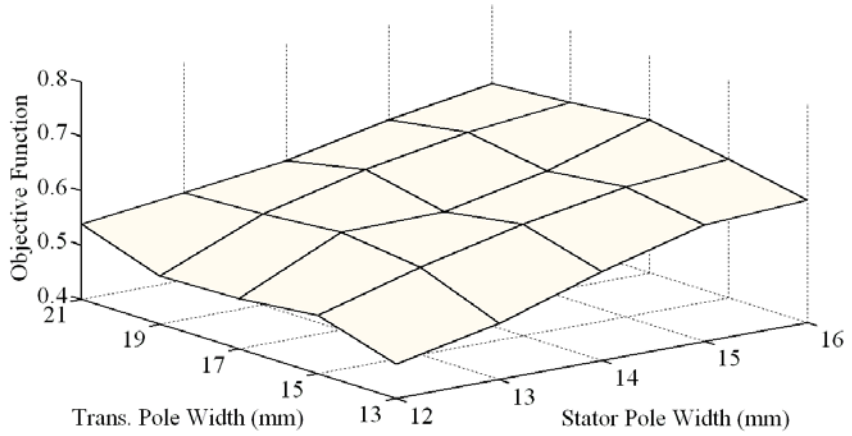

Fig. 5-7 Objective function with priority in average force

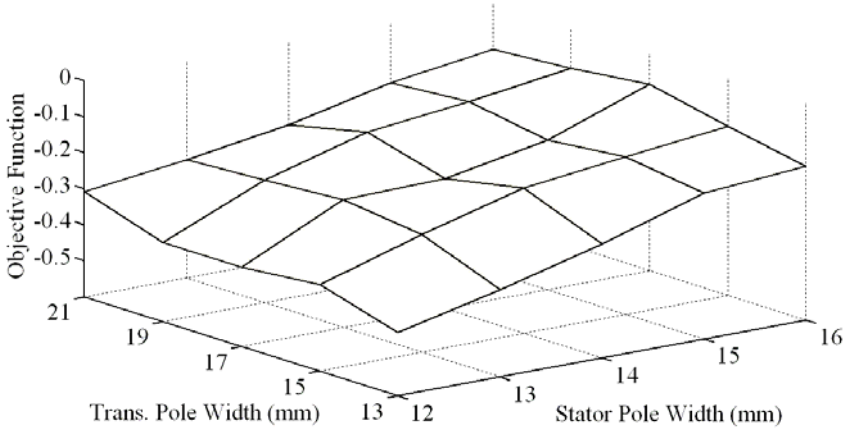

Fig. 5-8 Objective function with priority in force ripple

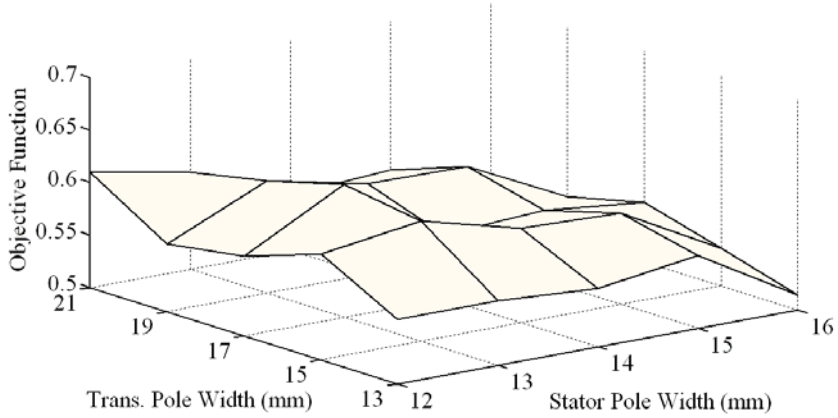

Fig. 5-9 Objective function with priority in force density

The results of optimal stator and translator pole width with various weight factors are presented in Table 5-1. It can be observed that the optimal stator and translator pole width are 13mm and 17mm respectively, when the average force per core volume is considered to have high priority in optimization. Apart from this situation, the optimal stator and translator pole width are 16mm and 17mm respectively. The same optimal pole widths are obtained when three objectives have the same priority and high priority to average force or force ripple. One can decide on the most appropriate set by considering which objective is the most important criteria you want to achieve based on the practical situation. We assume that three objectives have the same priority during the optimization process of our first prototype.

TABLE 5-1
OPTIMAL POLE WIDTH PAIR AT VARIOUS WEIGHT FACTORS

Weight factor	Optimal w_s	Optimal w_t
w_F=1/3, w_R=1/3, w_V=1/3	16 mm	17 mm
w_F=0.7, w_R=0.2, w_V=0.1	16 mm	17 mm
w_F=0.1, w_R=0.7, w_V=0.2	16 mm	17 mm
w_F=0.1, w_R=0.2, w_V=0.7	13 mm	17 mm

TABLE 5-2
OPTIMAL POLE WIDTH PAIR AT VARIOUS VOLUME LIMITATIONS

Volume Limitation	Optimal w_s	Optimal w_t
300*300*600	16 mm	17 mm
270*270*600	15 mm	19 mm
250*250*600	13 mm	17 mm

Table 5-2 shows the optimal stator and translator pole width according to various suspension volume limitations. All the results are obtained with equal priority to

three objectives. It can be observed that the optimal pole widths are changed with the volume limitation. Hence, the determination of suspension volume is critical in the preliminary design of LSRA. The results of average force, force ripple and average force per core volume at three optimal pole width pairs and three regular pole width pairs are demonstrated in Table 5-3.

TABLE 5-3
RESULTS OF OBJECTIVES AT VARIOUS POLE WIDTH PAIRS

w_s	w_t	F (N)	FR %	FV (N/m3)
13 mm	17 mm	551.6	43.7	167927
16 mm	17 mm	609	27.9	135190
15 mm	19 mm	592.5	34.3	148299
12 mm	13 mm	493.5	57.4	165958
16 mm	21 mm	599	30.8	130618
14 mm	17 mm	556	41.6	150077

5.4Experimental Verification

5.4.1 Prototype of LSRA

In order to verify the design optimization and actuator performance, a prototype of proposed LSRA was manufactured, as is shown in Fig. 5-10. The optimized parameters of the proposed LSRA are summarized in Table 5-4 and the rest parameters remain unchanged. It can be observed that the value of stator and translator pole width is 13mm and 17mm, respectively, which are the optimal values under volume constraint at $250\text{mm} \times 250\text{mm} \times 600\text{mm}$.

TABLE 5-4
OPTIMIZED SPECIFICATIONS OF LSRA

Parameters	Value
Stator pole width	13 mm
Translator pole width	17 mm
Stator pole height	49 mm
Stator yoke thickness	13 mm

(a) Stator

(b) Translator

(c) Final assembly

Fig. 5-10 Prototype of optimized LSRA

5.4.2 Flux linkage and force measurement

The experimental setup for static characteristic measurement of the LSRA is illustrated in Fig. 5-11. The flux linkage and force of each phase are measured at a step of 2mm during one stroke. The excitation current for test ranges from 0A to 24A. The simulation and experimental results of flux linkage and force profiles are demonstrated in Fig. 5-12 and Fig. 5-13, respectively. The position is set to 0mm when the stator and translator are fully unaligned. It can be observed that the measured flux linkage and force have a close agreement with the results from FEA. The discrepancy is mostly less than 10%, and the maximum error is not more than 25% for certain positions. The discrepancy is primarily introduced due to manufacturing and measurement error.

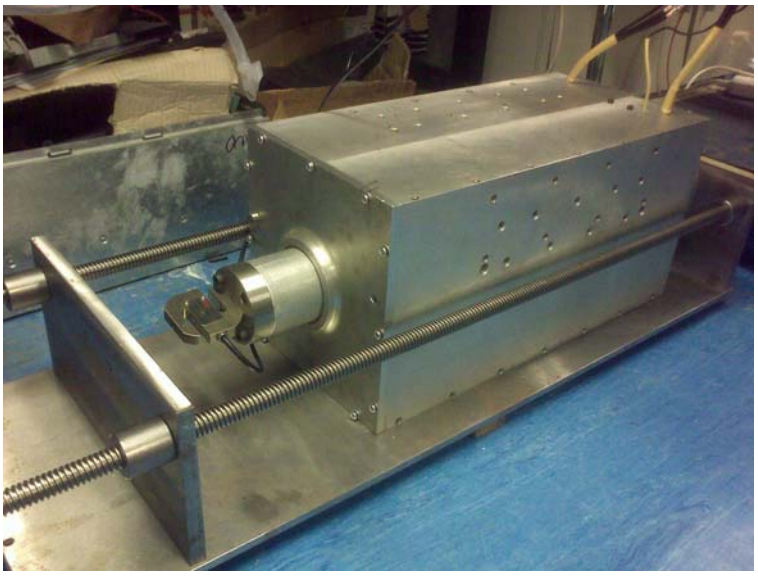

Fig. 5-11 Experimental setup

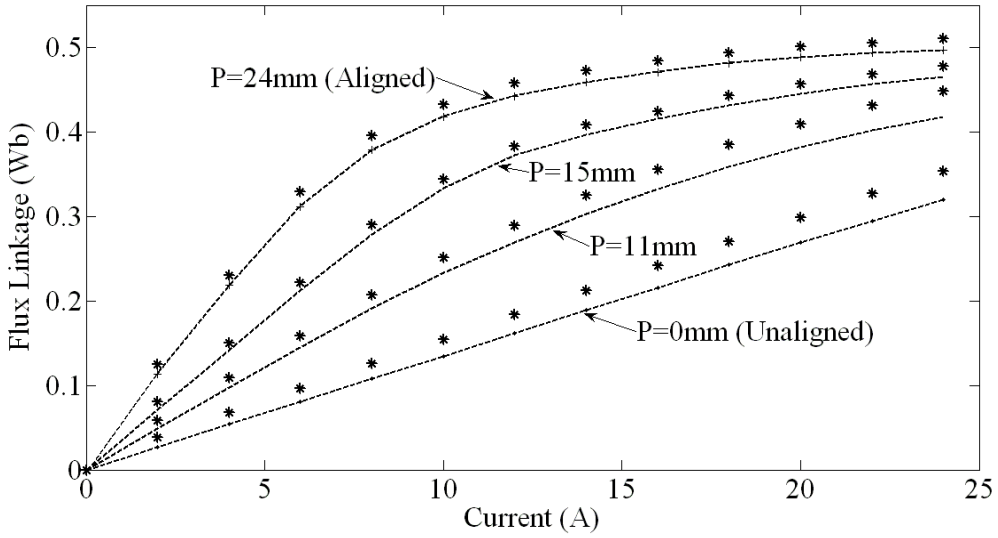

Fig. 5-12 Flux linkage characteristics (Dotted line: FEA, Solid line: Measured)

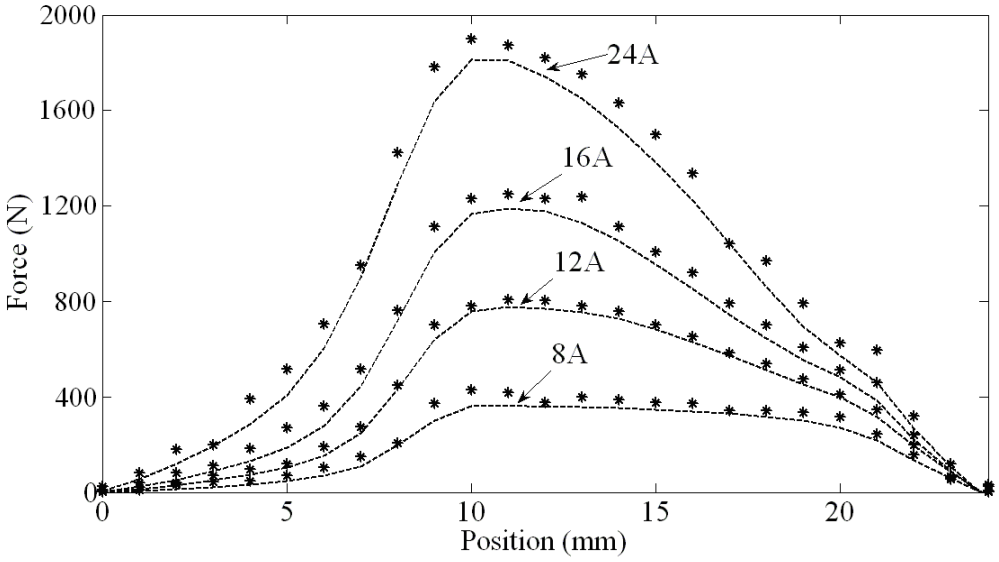

Fig. 5-13 Force profiles (Dotted line: FEA, Star: Measured)

5.5Summary

Based on the requirements from the active suspension constraints, three criterions, such as average force, force ripple and average force per core volume, are proposed to evaluate the performance of the LSRA. Therefore, a multi-objective optimization method is applied to obtain the optimal dimension of the LSRA. The stator and translator pole width are selected as optimization variables. Various combinations of weight factor in optimization objective function are analyzed and compared. With different priority to three objectives and under different volume constraints, the optimal values of stator and translator pole width are changed. Finally, an optimized LSRA was prototyped and tested to verify the multi-objective design optimization. The experimental results keep a good agreement with the simulations.

Chapter 6

Direct Instantaneous Force Control

Linear switched reluctance actuator (LSRA) based electromagnetic active suspension system has the advantages of robust structure, low cost, high reliability and fast dynamic response. Moreover, LSRA can be operated in regenerating mode. The kinetic energy, which is dissipated as heat in passive suspensions, can be recovered back to the power source or provided to other instruments under certain circumstances. The regenerative power can compensate for the energy consumption, and improve the overall efficiency of the active suspension system.

However, the inherent force ripple of LSRA will degrade the performance of active suspensions, especially the passenger ride comfort. Therefore, a high performance control technique for force ripple minimization is critical for the active suspension system. The energy consumption is another important issue, especially for the potential application of active suspensions in electric vehicle, which has a direct impact on the travel range. The problem can be improved by reducing the copper loss during operation.

LSRA has been studied in many applications, such as automation machine [83] and elevator [35]. Most applications are concerned with position control [84], whereas the control objective in active suspension system is to track the force demand that generated from the suspension controller. There are primarily two types

of techniques for force control. The first method is regarded as the indirect method; the required force is converted to equivalent current demand, and the output force is controlled by regulating the excitation current [85, 86]. The second method is to use direct instantaneous force control (DIFC). The instantaneous force is used as the control variable, and it directly counteracts the force error. In this way, a faster dynamic response and a better force ripple elimination capability can be obtained.

This chapter presents an improved DIFC which incorporates force distribution function (FDF), instantaneous force estimation, hysteresis force control and on-line determination of switching positions. FDF is considered as an effective way to alleviate the problem of force ripple, when there is an overlap of effective force region between adjacent phases. The estimated forces are not only used as feedback in hysteresis force control, but can also be used to improve the FDF. Since the primary goal of LSRA control is precise traction of force demand and force ripple minimization, the operational efficiency is subjected to the force dynamics. In the premise of ensuring acceptable force ripple, the energy efficiency of both motoring and regenerating mode is optimized by on-line adjusting the turn-on and turn-off position as the variation of force demand.

6.1 Four-quadrant Operation of LSRA

6.1.1 Operation Mode

The equivalent circuit is always used to analyze the dynamic performance of LSRA, and helpful for understanding the operation. If phase winding is excited after the unaligned position, where the variation of phase inductance is

positive, $dL/dx > 0$, the LSRA operates in motoring mode. If phase winding is excited after the aligned position, where the variation of phase inductance is negative, $dL/dx < 0$, the LSRA operates in regenerating mode. The variation of inductance and force with translator position in four-quadrant operation are illustrated in Fig. 6-1. Considering the motion direction, four-quadrant operation is achieved by regulating the excitation sequence and switching position of each phase.

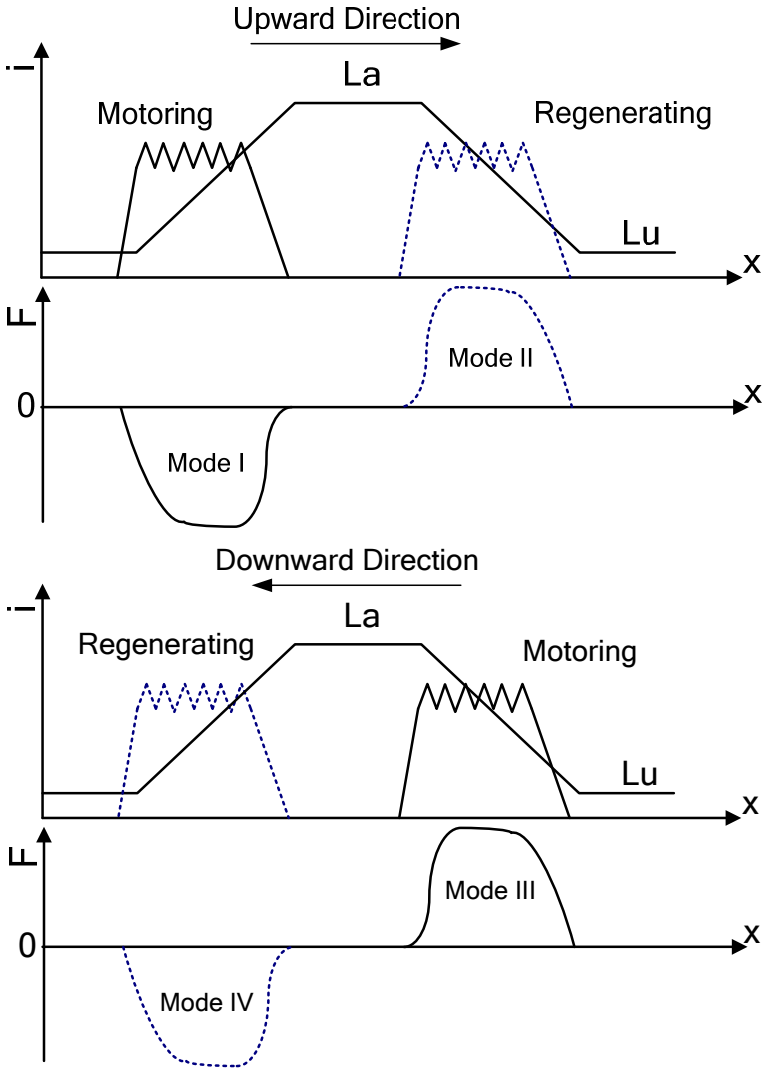

Fig. 6-1 Four-quadrant Operation

The switching condition of four operation modes depends on the suspension deflection and relative velocity of sprung and unsprung mass, as is shown in Table 6-1. For example, the suspension deflection and the relative velocity become positive as the wheel is falling into a sunken obstacle. In order to reduce the downward acceleration of sprung mass, an active stretching force is needed to support the sprung mass, and to prevent it from falling. The actuator operates at motoring mode during this stage. After the wheel reaches the bottom and moves upward, the relative velocity turns negative. A damping force is generated by the actuator, and the mechanical energy can be recovered by operating in regenerating mode. The similar situation happens with negative suspension deflection for raised obstacle.

TABLE 6-1
SWITCHING CONDITIONS OF OPERATION MODE

Suspension Deflection $x_s - x_{us}$	Relative Velocity $\dot{x}_s - \dot{x}_{us}$	Active Force F	Operation Mode
$x_s - x_{us} > 0$	$\dot{x}_s - \dot{x}_{us} \geq 0$	Stretch	Motoring
	$\dot{x}_s - \dot{x}_{us} < 0$		Regenerating
$x_s - x_{us} < 0$	$\dot{x}_s - \dot{x}_{us} \geq 0$	Contraction	Regenerating
	$\dot{x}_s - \dot{x}_{us} < 0$		Motoring
$x_s - x_{us} = 0$	$\dot{x}_s - \dot{x}_{us} = 0$	Null	Standby

The stator and translator of LSRA are connected to the unsprung and sprung mass, respectively. Hence, the regenerative energy is captured when there is a relative movement between the sprung and unsprung masses due to the road irregularities. The experimental setup of quarter-car model with the proposed LSRA is demonstrated in Fig. 6-2. Two accelerometers are attached to the sprung and

unsprung mass, respectively. By further integrated the acceleration, velocity of both masses can be obtained. The information is applied to calculate the required force that LSRA should exert.

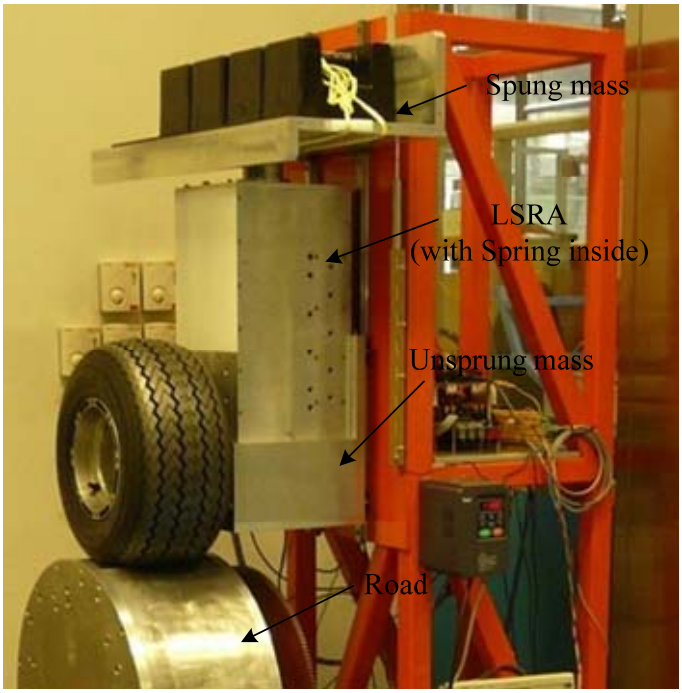

Fig. 6-2 Experimental setup of quarter-vehicle model

6.1.2 Optimization Criteria

Although the force ripple is the dominant criterion of LSRA control for suspension application; other operation criteria (e.g. the efficiency) is also critical for the system performance. The efficiency has a direct impact on the energy consumption of vehicles, especially for the electric vehicles. Therefore, to obtain a high performance active suspension system, the force ripple and operation efficiency are selected as the optimization criteria in this chapter.

For the simplicity of calculation, the force ripple defined in this chapter is the

ratio of force dip to the peak force, as defined by equation (5-5).

Copper loss is the energy dissipated by the resistance of phase winding, and contributes to large decrease of the actuator efficiency. Copper loss increases as the square of the rms phase current I_{rms} , which is given by

$$Pcu = N_{ph} I_{rms}{}^2 R \tag{6-1}$$

Hence, it is justified to examine the efficiency by the value of rms phase current.

6.2 Direct Instantaneous Force Control

The proposed DIFC scheme for LSRA is composed of force estimation unit, force distribution function, hysteresis force controller and on-line determination unit of switching positions. The structure of this scheme is shown in Fig. 6-3. The force distribution function is implemented to distribute the total force demand among four phases. The force reference per phase is varied with the translator position, but the sum of four individual values is equivalent to the total force demand at any position. Before the incoming phase is energized, the actuator force is contributed by the outgoing phase with the reference of total force demand. The force references of the remaining three phases are determined as zero. When entering the effective force region of the incoming phase, the force demand of outgoing phase is slowly reduced following the given function, and that of the incoming phase is increased accordingly. The total force demand is distributed between these two adjacent phases

until the outgoing phase is turned-off. The rest of the two phases are turned-off during this stage. By this means, four individual phase demands are generated, and then compared with the estimated force of corresponding phase respectively. The switching signals are then generated by the hysteresis controller in accordance to the force errors and driving sequence. Although the acceptable force ripple can be achieved within a wide range of switching positions, the efficiency can be improved by optimizing the turn-on and turn-off positions. Moreover, the optimal switching positions are varied with the force demand and movement speed. The selection of optimal value can be realized by the on-line determination scheme.

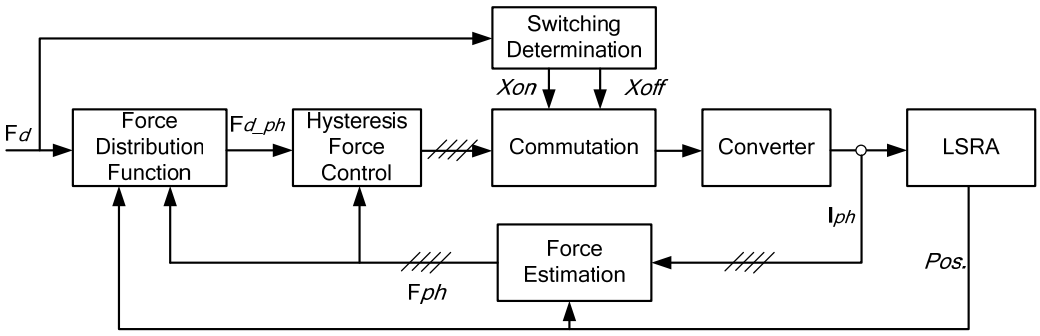

Fig. 6-3 Structure of the DIFC

6.2.1 Force estimation

The accuracy of force estimation directly affects the performance of the DIFC. However, the nonlinearity and discontinuous mode of operation make the relationship between the force and excitation current too complex to express in an analytical equation. The force depends not only on the excitation current, but also on the translator position as well. Therefore, the look-up table and neural network are the most practical way to on-line estimate the instantaneous force, and the look-up

table is more favorable in real-time application due to the less computation time [51][87-89].

In this chapter, the measured force characteristics as a function of excitation current and translator position are used to develop the look-up table, as is presented in Fig. 6-4. By ignoring the mutual coupling effects and minor error between phases induced from manufacturing, the characteristic of single phase is used to decrease the size of look-up table [90-92]. Furthermore, the negative force value can be omitted from the table and predicted from the symmetrical positive force. The interpolation algorithm is used to estimate the rest values that among the measured points stored in the look-up table.

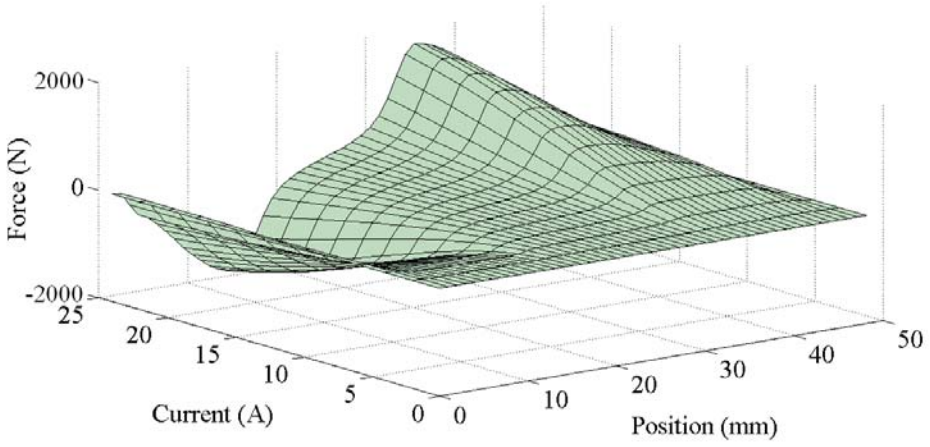

Fig. 6-4 Force characteristics

6.2.2 Force distribution function

The effective force regions of neighboring phases are overlapped to ensure the two-phase excitation simultaneously during the phase commutation. It makes the force distribution function (FDF) an effective way to reduce the force ripple. By

distributing the force demand between two neighboring phases, the phase force is individually regulated and varied smoothly with the translator position.

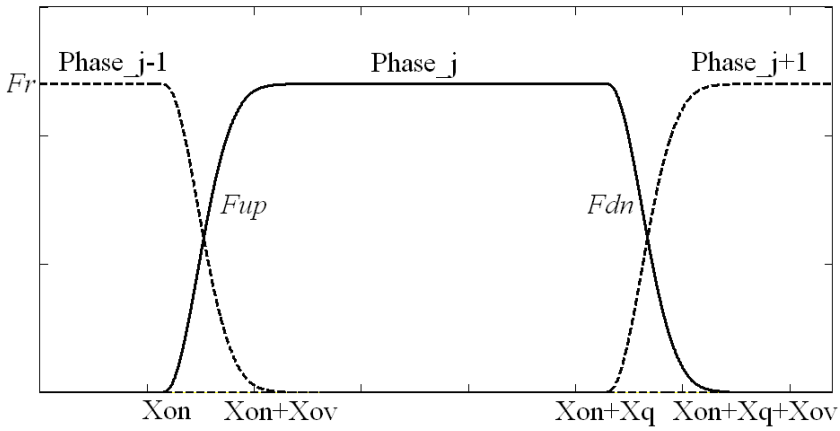

Fig. 6-5 Typical profile of exponential FDF

Since there is no unique option for distribution function, a great many FDFs, such as linear, cubic, sinusoidal and exponential function, have been proposed and studied by previous researchers [93-96]. Among these four FDFs, the exponential FDF is considered to be a better choice for improving both the efficiency and speed range [97]. The typical profile of exponential FDF is shown in Fig. 6-5, and can be expressed by The FDFs mentioned above can be expressed by

$$FDF_j(x)=\begin{cases} 0 & 0 \le x \le x_{on} \\ F_{up\_j}(x) & x_{on} \le x \le x_{on}+x_{ov} \\ F_r & x_{on}+x_{ov} \le x \le x_{on}+x_q \\ F_{dn\_j}(x) & x_{on}+x_q \le x \le x_{on}+x_q+x_{ov} \\ 0 & x_{on}+x_q+x_{ov} \le x \le x_p \end{cases} \tag{6-2}$$

where x_{on} denote the turn-on position, x_{ov} is the overlap region, x_q and x_p are the stroke and translator pole pitch, F_r is the total force demand, $F_{up\_j}(x)$ and $F_{dn\_j}(x)$ represent the function of rising portion and the declining

portion, which can be written as

$$F_{up\_j}(x) = F_r\left[1-\exp(\frac{-(x-x_{on})^2}{x_{ov}})\right] \tag{6-3}$$

$$F_{dn\_j}(x) = F_r\left[\exp(\frac{-(x-x_{on}-x_q)^2}{x_{ov}})\right] \tag{6-4}$$

Based on the force estimator, an adaptive exponential FDF is proposed to reduce the force ripple of LSRA. During the overlap period, the distribution function of outgoing phase is the same as exponential function, whereas the force demand of incoming phase is adaptively varied with the difference between total force demand and estimated force of outgoing phase. Therefore, the phase commutation is coordinated to certain extend and the force ripple minimization is ensured in a wider range of switching position.

The proposed FDF can be expressed as

$$FDF_j(x) = \begin{cases} 0 & 0 \le x \le x_{on} \\ F_{up\_j}(x) & x_{on} \le x \le x_{on}+x_q \\ F_{dn\_j}(x) & x_{on}+x_q \le x \le x_{on}+x_q+x_{ov} \\ 0 & x_{on}+x_q+x_{ov} \le x \le x_p \end{cases} \tag{6-5}$$

$$F_{up\_j}(x) = F_r - F_{est\_j-1} \tag{6-6}$$

$$F_{dn\_j}(x) = F_r\left[\exp(\frac{-(x-x_{on}-x_q)^2}{x_{ov}})\right] \tag{6-7}$$

where F_r is the total force demand, F_{est_j-1} is the estimated force of outgoing phase, F_{up_j} and F_{dn_j} denote the rising and declining distribution function of incoming phase, respectively.

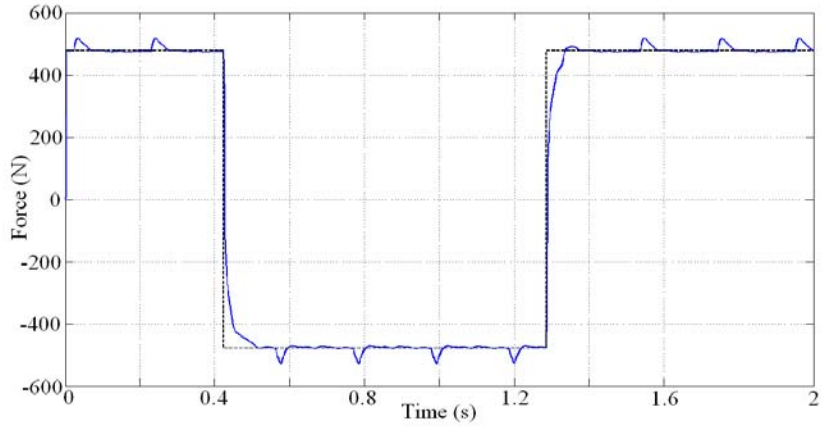

(a)

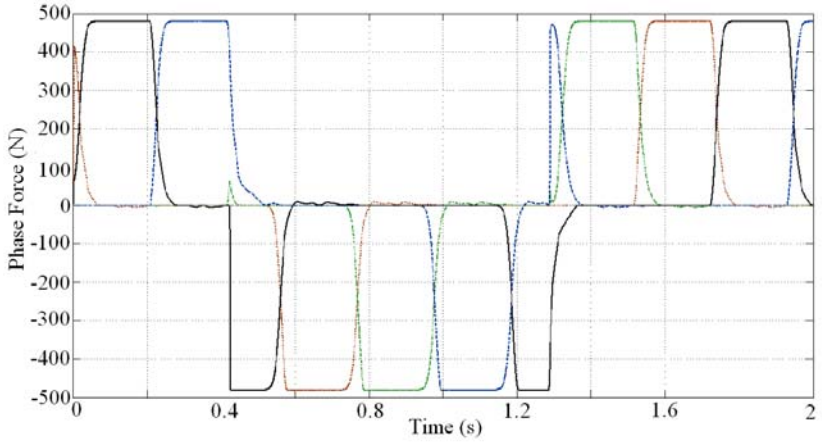

(b)

Fig. 6-6 Motoring operation with exponential FDF (a) Force trajectory response (b) Phase force

In order to verify the effectiveness of proposed FDF, a number of simulations are performed in the Matlab/Simulink environment. The model of LSRA is constructed based on the measured flux linkage and force characteristics. Both motoring and regenerating mode are simulated, because four-quadrant operation of LSRA is required in active suspension application. The performances of exponential and proposed FDF in motoring operation are demonstrated in Fig. 6-6 and 6-7,

respectively. It can be observed that the force profile is significantly improved with the proposed FDF. The force reference is tracked with no force ripple during the commutation. Two simulations are performed under the same force demand and switching positions. Fig. 6-8 and 6-9 illustrate the performances of exponential and proposed FDF in regenerating operation. It can be seen that significant force ripple is generated with the exponential FDF due to the low overlap region of neighboring phases, whereas the force profile is still smooth during the commutation when proposed FDF is applied.

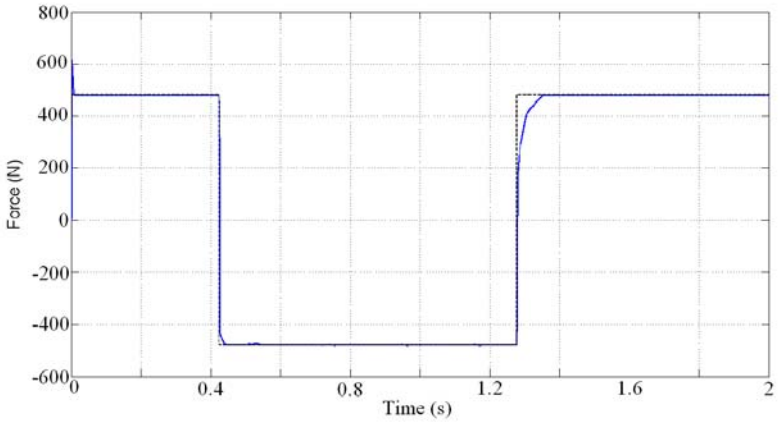

(a)

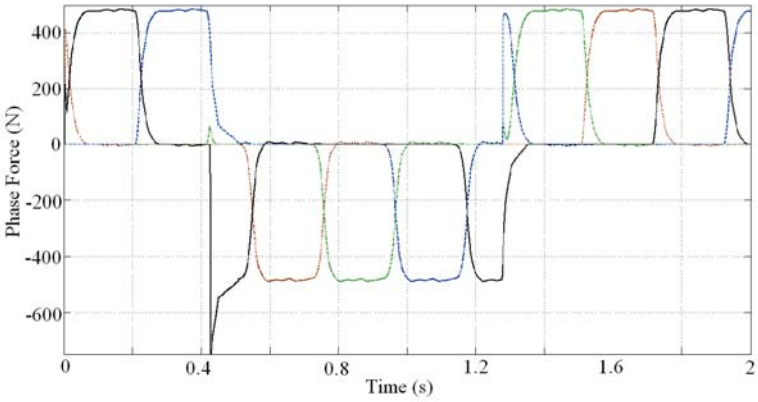

(b)

Fig. 6-7 Motoring operation with proposed FDF (a) Force trajectory response (b) Phase force

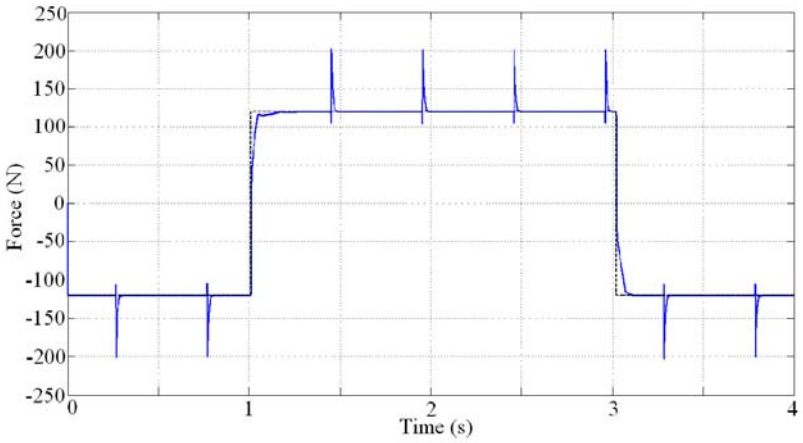

(a)

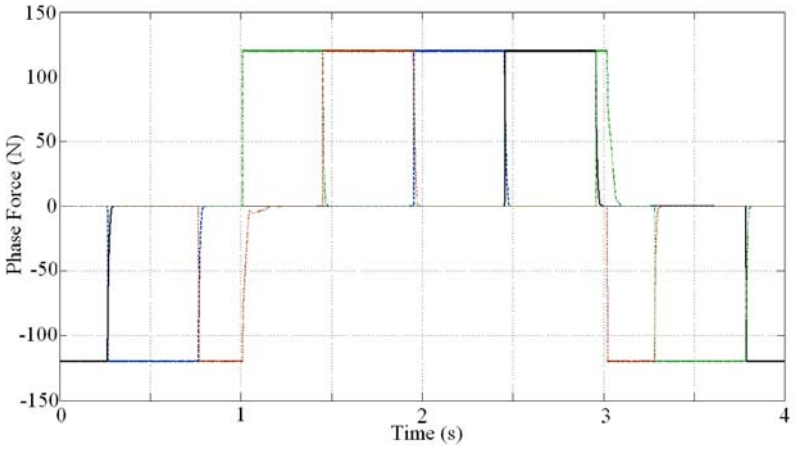

(b)

Fig. 6-8 Regenerating operation with exponential FDF (a) Force trajectory response (b) Phase force

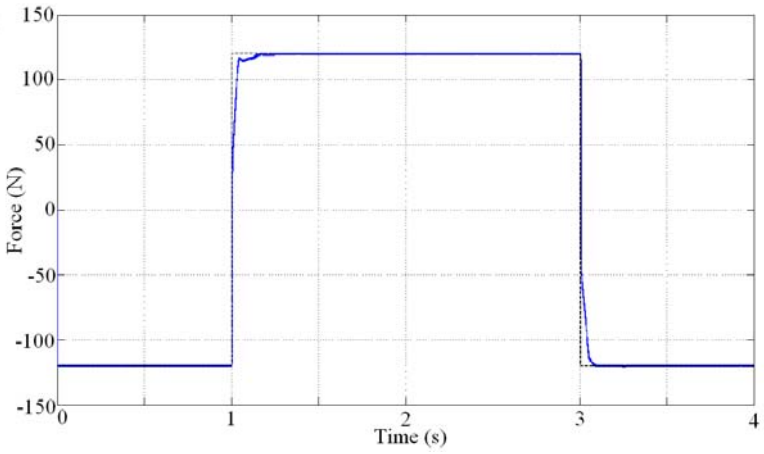

(a)

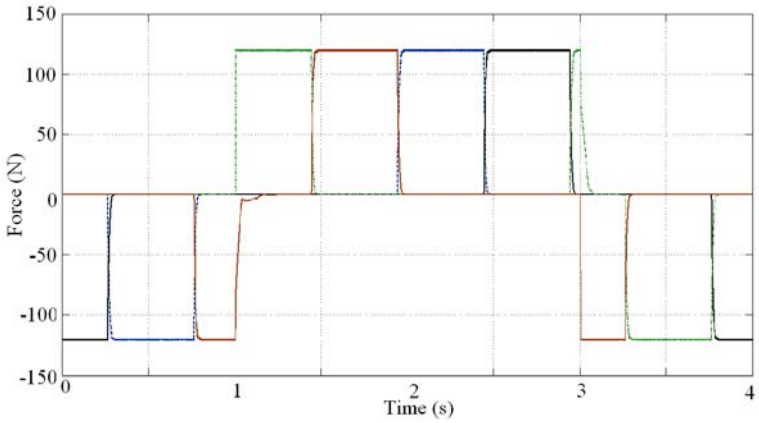

(b)

Fig. 6-9 Regenerating operation with proposed FDF (a) Force trajectory response (b) Phase force

6.2.3 Hysteresis force controller

The total force demand is distributed to four individual force references for each phase, and compared with the estimated phase force, respectively. Thereby, the individual force of each phase is regarded as a control variable, instead of the total force. The control signals were generated by a hysteresis force controller, in response to the errors between the force reference and the estimated value of the corresponding phase. The phase commutation is considerably simplified by the

separated force control algorithm. Because of the presence of mutual coupling when two adjacent phases are excited, the flux distribution and magnetic saturation are different from that of single-phase excitation mode, as well as the ability of force output. Certain discrepancy between the estimated force and actual force is introduced by ignoring the effect of mutual coupling. Since the force of each phase is estimated and controlled separately in this control method, the error could be increased during commutation where two phases are excited simultaneously. However, this minor discrepancy is ignored for most practical purpose.

To improve the tracking accuracy and minimize the force ripple, a relative high bandwidth hysteresis controller is needed in DIFC. However, it will increase the switching losses and sensitivity to signal noise. There is a trade-off in determine the hysteresis band. The force dynamics for the magnetizing, freewheeling and demagnetizing states and noise immunity margin should be carefully examined. It is practical to alter and optimize the hysteresis band by comparing the experimental results.

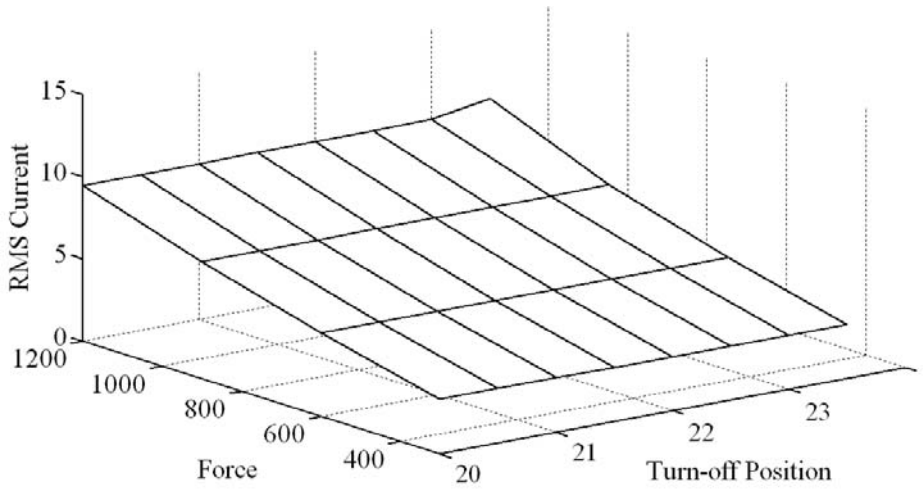

Fig. 6-10 Effects of turn-off position

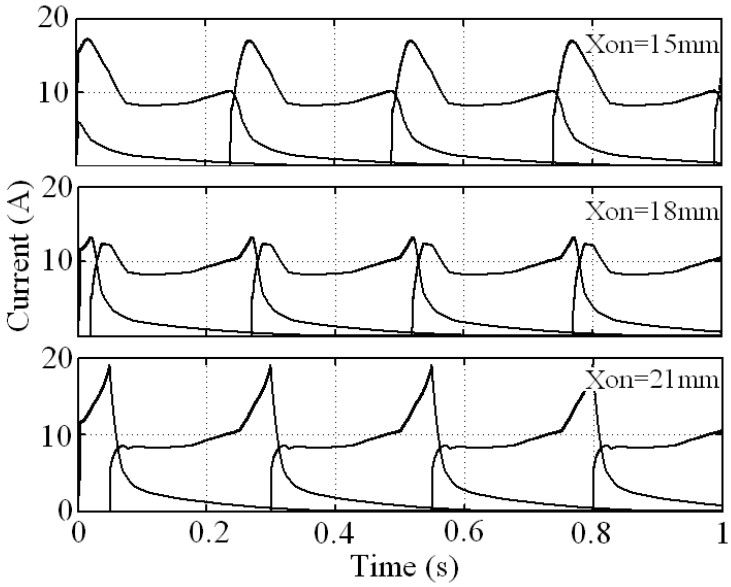

Fig. 6-11 Current profile at different turn-on position

6.2.4 Switching parameters optimization

Although the force ripple minimization is achieved over a wider range of switching parameters, the efficiency can be considerably different for the various selection of switching positions. Therefore, the turn-on and turn-off positions can be optimized to improve the operation efficiency based on the force demand and motion speed. Because LSRA is basically operated below the base speed in active suspension system, the impact of speed is not considered in this chapter.

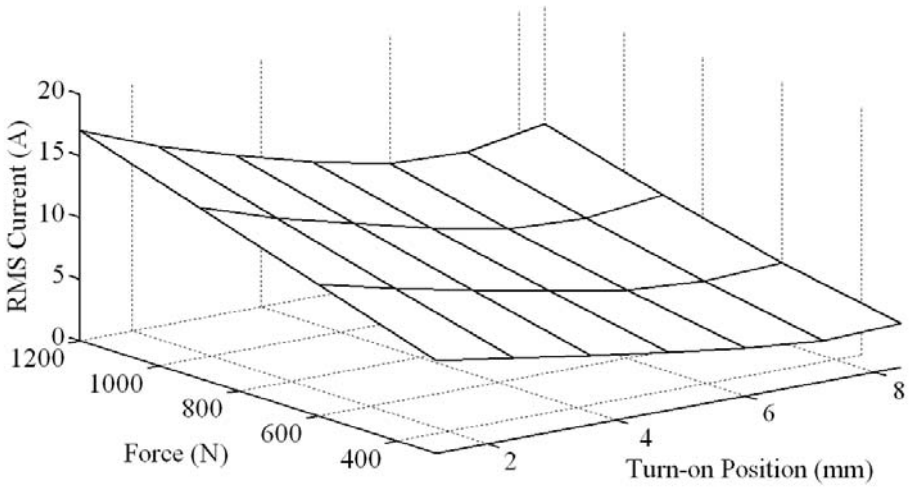

Fig. 6-12 Effects of turn-on position

For motoring operation, it can be observed from Fig. 6-10 that the rms phase current is insensitive to the change of turn-off position. Thus, the efficiency is decided by the selection of turn-on position. The optimal value is determined as the excitation current is built up when entering the effective force region. Certain advance or delay will result in increased peak and rms current, as is shown in Fig. 6-11. Also, the advance turn-on position will extend the conductive region, thus increase the rms current. The optimal turn-on position can be obtained from Fig. 6-12. It can be observed that the turn-on position with the lowest rms current is advanced gradually with the increase of force demand. It is because that more time is required to build up higher phase current.

For regenerating operation, the aim is to keep the force profile smooth during commutation and reduce the force ripple; hence the improvement of efficiency is subject to the primary objective, which is different from the control strategy of other switched reluctance generator. It can be observed from Fig. 6-13 that both switching

positions contribute to the rms phase current. The efficiency is basically increased with the decrease of turn-on and turn-off positions. Although the lowest rms current is obtained when the phase is turned-off at 36mm, the force ripple is deteriorated because of the lack of overlap region of neighboring phases.

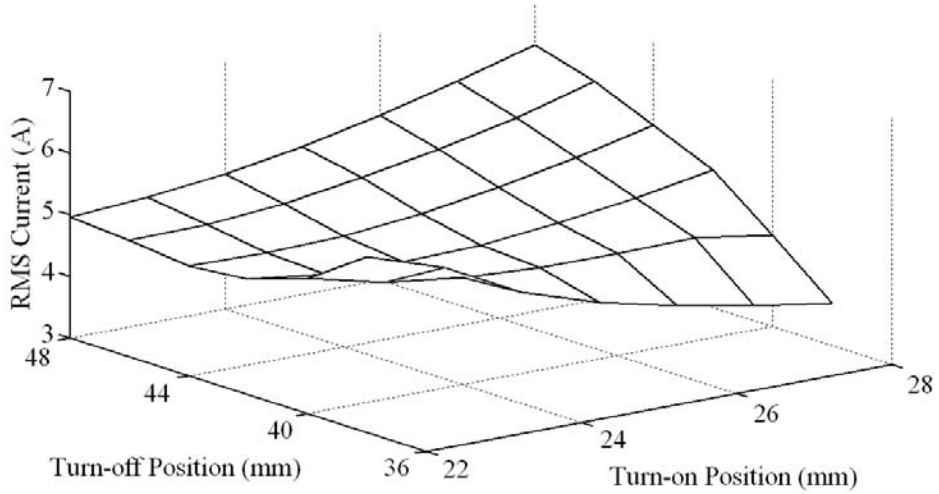

Fig. 6-13 Effects of switching positions

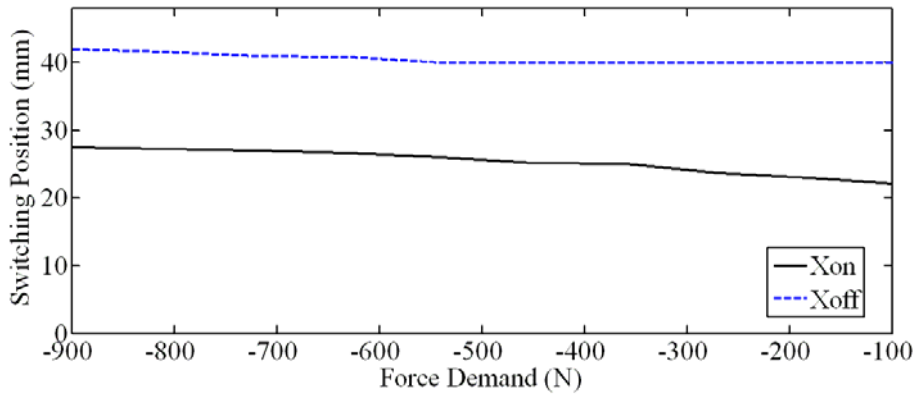

Fig. 6-14 Optimal switching positions in regenerative operation

As demonstrated in Fig. 6-14, the optimal turn-on position in regenerative operation is increased as the growth of force demand. The turn-off position remains constant at low force demand, and then increases to ensure an adequate overlap region as the force demand getting larger.

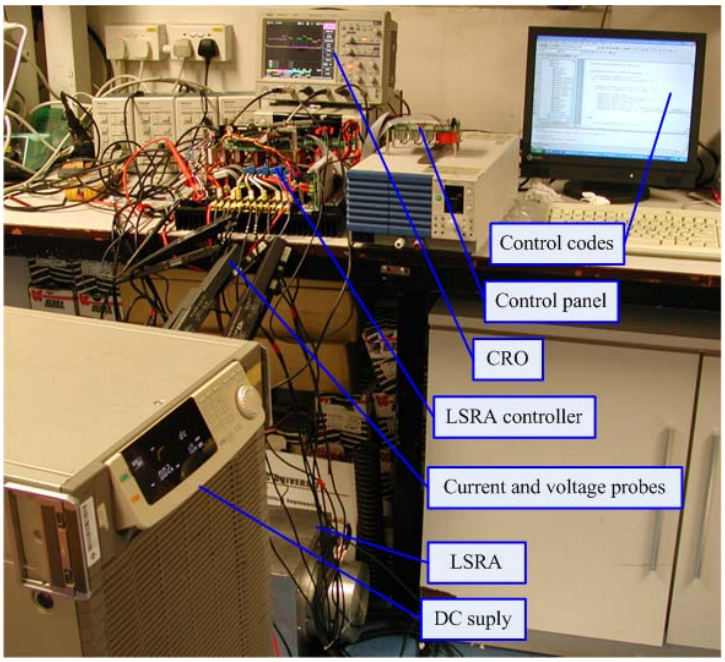

Fig. 6-15 Experimental setup

6.3 Experimental Results

The performance of DIFC strategy has been experimentally verified based on the dSPACE DS1104 controller board. The laboratory set-up with the LSRA, asymmetric bridge converter and dSPACE controller is shown in Fig. 6-15. An LVDT position sensor was installed inside the LSRA to measure the translator position. In order to obtain the static force profile and construct the force estimator, a load cell was implemented to measure the force in a step of 2mm under the excitation current from 2A to 20A. The LSRA is placed vertically when testing with

load and the regenerative operation mode. The external force can be varied with the different weight attached to the translator.

First, to compare the performance of proposed adaptive FDF, the experimental results with exponential FDF and without FDF are illustrated in Fig. 6-16 and 6-17, respectively. The control method without FDF means that the force of two neighboring phases is regulated indirectly by comparing the total force during commutation. The experimental force and current profile with adaptive FDF is shown in Fig. 6-18. Three experiments were carried out at both motoring and regenerating mode under the same external force and switching positions. The external force for regeneration is exerted by the gravity of translator itself and the load attached to it. The translator is first controlled in motoring operation to move upward, and then move downward by the effect of gravity. Meanwhile, the LSRA is operated in regenerative mode and produces an upward force. The operation mode changes between the mode I and mode IV. Hence, the sigh of force both in motoring and regenerating is negative. It can be observed that the force profile of exponential FDF is significantly deteriorated during phase commutation at both operation modes, although the rms current is relative low. The force ripple without FDF is reduced, but at a cost of high peak and rms phase current. The peak current is as much as 50% larger than that of the exponential FDF. In contrast, the force ripple minimization is achieved by the application of adaptive FDF with higher efficiency. It can be observed that the rms current is low and flat without huge current peak. Because the force characteristics under low excitation current are relatively flat between 8mm and 22mm, which is the operating region of generating mode, there is no need of

much higher phase current at both turn-on and turn-off positions for a low force demand. Hence, the phase current seems flat top in generating mode.

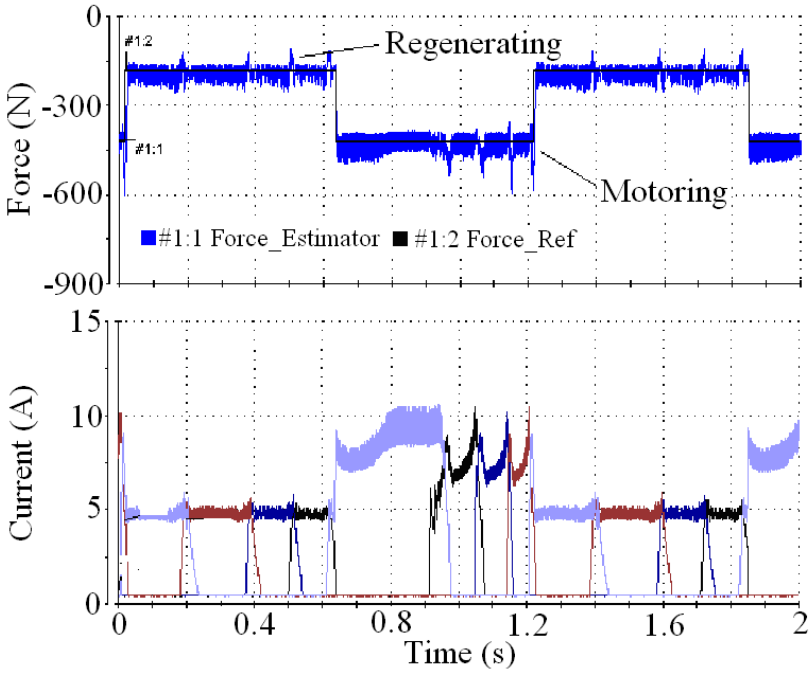

Fig. 6-16 Estimated force and measured current profiles with exponential FDF

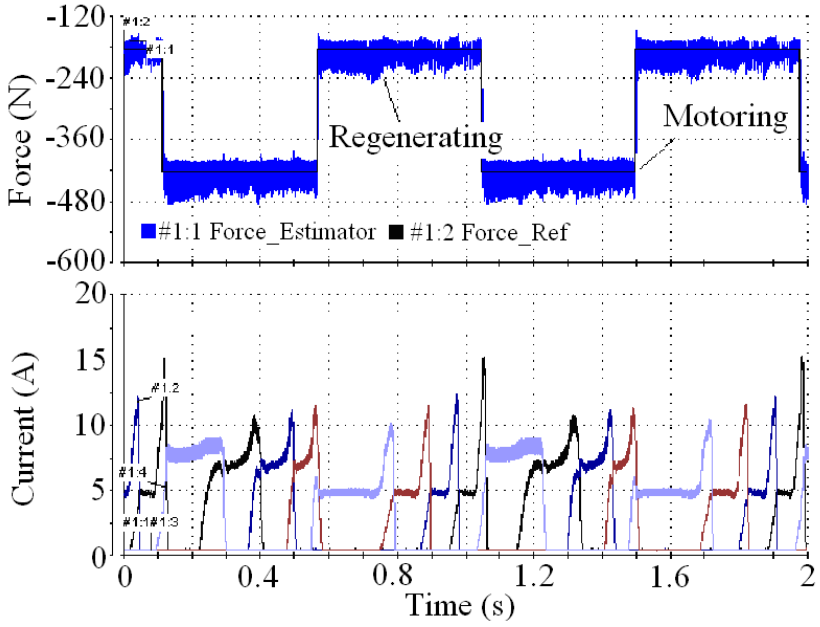

Fig. 6-17 Estimated force and measured current profiles without FDF

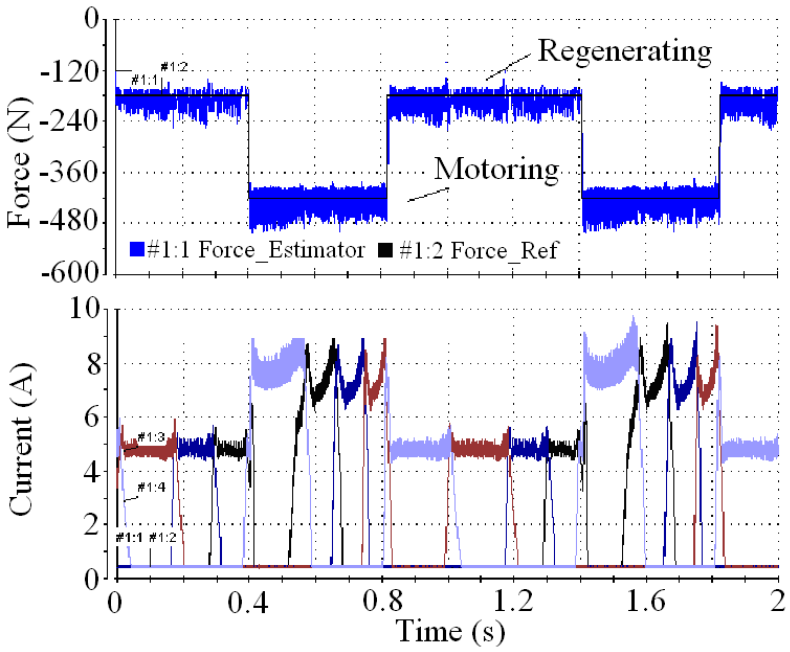

Fig. 6-18 Estimated force and measured current profiles with adaptive FDF

Further experimental tests are conducted to verify the commutation optimization process. The LSRA is placed horizontally and controlled to move back and forth continuously. The operation mode is changed between the mode I and III. Therefore, the force profile oscillated between positive and negative. Several combinations of switching parameters were implemented under a variation of force demand. The experimental results of total force, phase force and excitation current with different switching positions are demonstrated in Fig. 6-19 and 6-20.

It can be observed that the force profiles of two switching conditions have similar shapes with reduced force ripple, whereas the rms force current with advance turn-on position is much greater than that with optimal turn-on position. Fig. 6-18 and 21 illustrate the optimal response at a different force demand. The experimental

results are consistent with the theoretical analysis and simulation results. Therefore, it is much practical to change the switching parameters under different operation conditions.

Fig. 6-22 compares the operation efficiencies under optimal and normal switching positions over a wide range of force demand. Since the force ripple minimization is the primary objective, the comparison of efficiency is conducted among the situations with acceptable force ripple. It can be observed that the operation efficiency is improved considerably by optimizing the switching parameters, and the efficiencies under both modes are enhanced as the force demand increased.

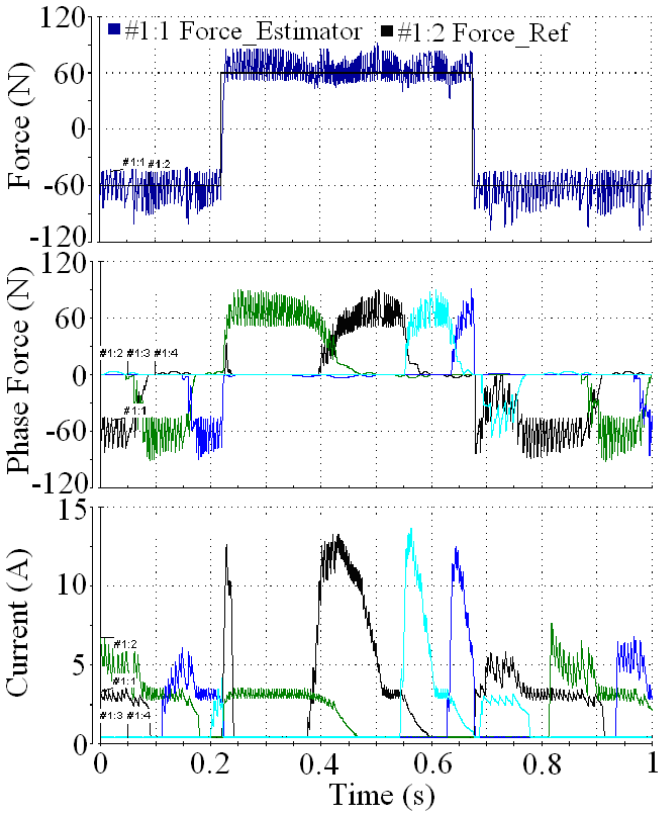

Fig. 6-19 Experimental results with advance turn-on position

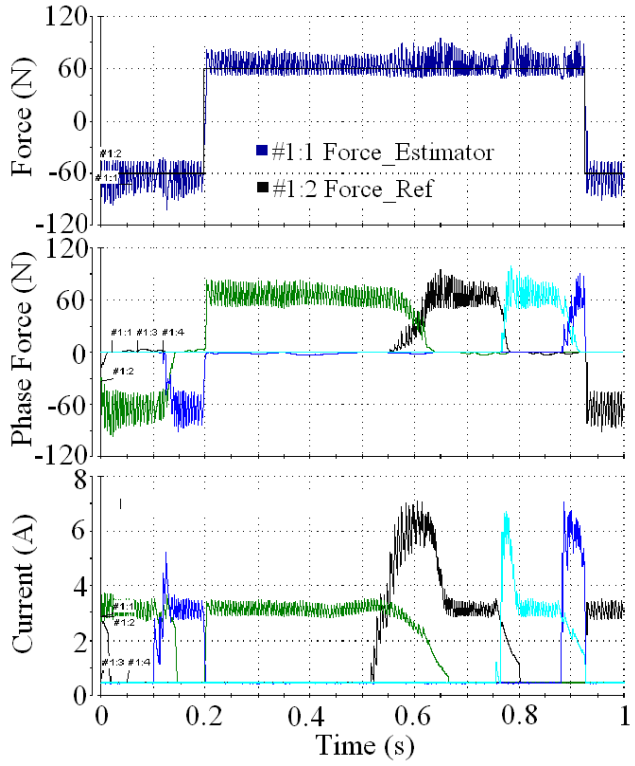

Fig. 6-20 Experimental results with optimal turn-on position

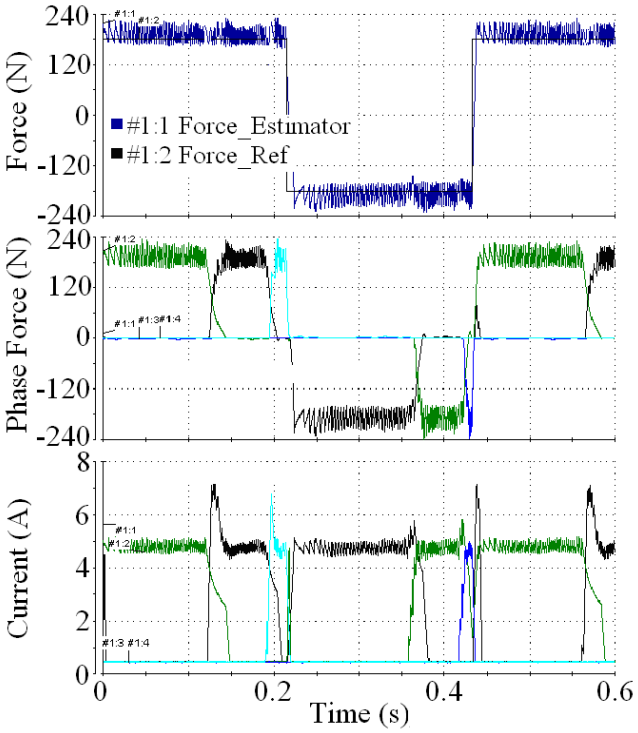

Fig. 6-21 Experimental results with higher force demand

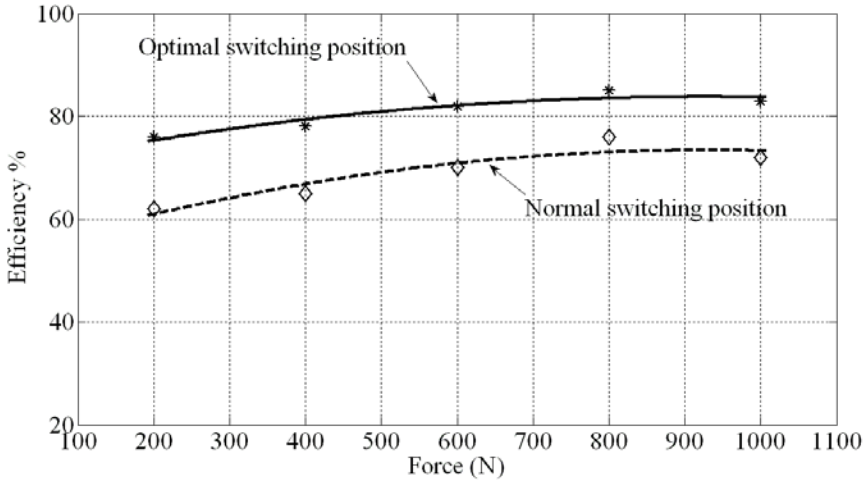

Fig. 6-22 Efficiency improvement with switching position optimization

6.4 Summary

For the application in active suspension system, an improved direct instantaneous force control is investigated for the four-quadrant operation of the LSRA. This control strategy is composed of instantaneous force estimation, force demand distribution, hysteresis force control and commutation optimization. An adaptive force distribution function is proposed to minimize the force ripple during phase commutation. Efficiency is then improved by on-line optimization of switching parameters, in the premise of ensuring minimum force ripple. The effectiveness of proposed strategy is verified by both simulation and experimental results.

Chapter 7

Conclusions and Suggestions for Further Research

In this thesis, the design, optimization, fabrication and control of a novel linear switched reluctance actuator are proposed for the application in vehicle active suspension system. The objective is to develop a high performance actuator with low cost and robust structure. Attempts to improve the force density and reduce the force ripple are made during the design and control stages. This chapter concludes the major contributions of this thesis with suggestions for further research on the LSRA based active suspension system.

7.1 Contributions and achievements

The major contributions and achievements of this thesis can be summarized as follows.

A. Introduction of the LSRA to active suspension system

Electromagnetic active suspension system has been studied and introduced over the past decade, due to the better dynamic and energy-efficient characteristics.

However, most electromagnetic actuators proposed by previous researchers are permanent magnet actuator, which is too expensive for commercial vehicle. In view of this situation, a novel configuration of linear switched reluctance actuator was introduced in suspension application for the first time in this thesis. A lower cost actuator with a high performance is obtained and it proved to be technical feasible.

B. System analysis of active suspension

The suspension system is analyzed based on the quarter vehicle model, which is simple but captures most important properties. The effects of spring stiffness, damping coefficient, sprung and unsprung mass are discussed through the frequency response. It is helpful to determine the optimal system parameters for the actuator design. A linear quadratic regulator (LQR) is proposed and simulated with quarter vehicle model to obtain the force requirement. The proposed method considers the performance of passenger riding comfort and road handling quality to find an optimal solution.

C. Novel configuration of the LSRA

The available space for active suspension is limited if no major mechanical structure of commercial vehicle is modified. This situation put an additional constraint on the volume of actuator, which means higher force density is required for the application. By considering the specific requirements and constraints, a novel configuration of LSRA composed of four double-sided modules is proposed. The elimination of lateral force makes it feasible to assemble in a compact way. The

whole design procedure, ranging from the determination of basic actuator parameters to the calculation of flux linkage characteristics, is covered in this thesis. The proposed design method is based on the geometrical dimension and magnetic equivalent circuit. No extensive knowledge about switched reluctance motor and no rotary-to-linear conversion are required.

D. Longitudinal and transversal end effect analysis

The characteristic of each phase is assumed to be identical when the LSRA is analyzed and controlled. However, there are certain differences between phases because of the mechanical fabrication and longitudinal end effect. This kind of end effect is caused by the finite length of the magnetic and electric circuit in the direction of the travelling field. To evaluate the longitudinal end effect of double-sided LSRA, two-dimensional FEA is carried out. The inductance variations with excitation current and translator position are analyzed, and a simple but practical solution is provided to reduce the imbalance between phases. The major causes that contribute to transversal end effect are concluded in this thesis. By comparing the results of two-dimensional and three-dimensional FEA, the sensitivities of transversal end effect to excitation current, translator position, stack length and translator stack length are analyzed. The results obtained in this thesis are helpful for predicting the actuator characteristics by two-dimensional FEA, which will reduce the computation time and improve the prediction accuracy during the design stage.

E. Multi-objective optimization of the LSRA

It is noted that the actuator parameters determined by analytical method is not the unique solution that meet the design requirements. To improve the performance of designed actuator, a multi-objective optimization method to obtain higher average force, reduced force ripple and higher force density is proposed for the double-sided LSRA in this thesis. Some practical constraints are taken into consideration in the optimization procedure. The effects of stator and translator pole width on three optimization criteria and actuator volume are analyzed.

F. Direct instantaneous force control of the LSRA

The objective of LSRA control is to track the force demand generated by the external suspension controller. To improve the dynamic response and reduce the force ripple, a novel direct instantaneous force control scheme for four-quadrant operation is proposed. The operation efficiency is also considered by optimizing the switching positions according to the force demand. The instantaneous force is on-line estimated based on the measured force characteristics. An adaptive force distribution function (FDF) is proposed to generate individual force demand for each phase. By introducing the on-line estimated force of outgoing phase to FDF, the force demand of incoming phase is adaptively adjusted. Therefore, the force ripple can be minimized over a wider range of switching positions. The force in the proposed scheme is regulated by a hysteresis controller. Since the force demand is distributed into four individual force demands and compared with estimated forces of corresponding phase, the hysteresis controller can be simplified.

7.2 Suggestions for further research

The suggestions for further research following this thesis can be outlined as follows.

A. Operation efficiency of proposed LSRA

The efficiency is an important feature of the proposed LSRA. High efficiency actuator can reduce the energy cost and expand the travel range if it is applied in electric vehicle. To determine the efficiency, there is a need to calculate the iron loss and eddy current loss analytically and further optimize the actuator parameters. The analytical losses need to be verified and corrected by experimental measurement.

B. Thermal analysis of the proposed LSRA

Temperature rise is another key factor during design stage that affecting the efficiency and actuator volume. Therefore, thermal analysis has to be developed for the proposed LSRA. The temperature rise in the actuator need to be calculated, and ensure it is kept within certain thermal constraints when achieving the force and power requirement. Thermal analysis is also helpful to modify the actuator configuration and to improve the cooling system.

C. New configuration of the LSRA

The LSRA proposed in this thesis is not the only configuration that meets the requirements from active suspension system. The proposed configuration could be further improved owing to its relatively complicate structure and high demand for

manufacturing. More configurations of LSRA with simpler structure, higher force density and lower manufacturing cost could be considered and developed.

D. Advanced force control method

Although the force ripple is significantly reduced through the direct instantaneous force control, it can not be minimized due to the hysteresis force controller. The requirement for high bandwidth and the compromise between the switching losses and sensitivity to signal noise lower the performance of force tracking. More advanced control method, such as sliding mode control, robust control, could be considered in the future work to further reduce the force ripple of LSRA.

List of publications generated from this project

Journal papers

[1] Zhu Zhang, Norbert C. Cheung, K. W. E. Cheng, X. D. Xue, "Longitudinal and transversal end-effects analysis of linear switched reluctance motor," *IEEE Trans. on Magnetics*, vol. 47, no. 10, pp. 3979-3982. 2011.

[2] Zhu Zhang, Norbert C. Cheung, K. W. E. Cheng, X. D. Xue, "Direct Instantaneous Force Control with Improved Efficiency for Four-quadrant Operation of Linear Switched Reluctance Actuator in Active Suspension System," *IEEE Trans. on Vehicular Technology,* issue4, vol.61, pp.1567-1576, 2012

Conference proceedings

[1] Zhu Zhang, Norbert C. Cheung and K. W. E. Cheng, "Application of Linear Switched Reluctance Motor for Active Suspension System in Electric Vehicle," The 25th world battery, hybrid and fuel cell electric vehicle symposium and exhibition (EVS25), Shenzhen, China, Nov. 5-9, 2010

[2] Zhu Zhang, N. C. Cheung, K. W. E. Cheng, X. D. Xue and J. K. Lin. "Longitudinal and Transversal End Effects Analysis of Linear Switched Reluctance

Motor," Presented at International Magnetics Conference (INTERMAG2011), Taipei, 2011

[3] Zhu Zhang, Norbert C. Cheung, K. W. E. Cheng, X. D. Xue, “Analysis and Design of a Cost Effective Converter for Switched Reluctance Motor Drives Using Component Sharing,” The 4th International conference on power electronics systems and applications (PESA 2011), Hong Kong, 2011

[4] Zhu Zhang, N. C. Cheung, K. W. E. Cheng, X. D. Xue and J. K. Lin, " Multi-objective optimal Design of a Linear Switched Reluctance Actuator in Active Suspension System, " Accepted for International Magnetics Conference (INTERMAG 2012), Vancouver, 2012

[5] J. K. Lin, K. W. E. Cheng, Z. Zhang, etc., “Integral sliding mode control and its application on active suspension system,” The 4th International conference on power electronics systems and applications (PESA 2011), Hong Kong, 2011

[6] X. D. Xue, K. W. E. Cheng, Z. Zhang, etc., “Investigation on parameters of automotive electromagnetic active suspension,” The 4th International conference on power electronics systems and applications (PESA 2011), Hong Kong, 2011

References

[1] Donald Bastow and Geoffrey Howard, "*Car Suspension and Handling,"* Pentech Press, London, 1993.

[2] R. A. Williams, "Electronically controlled automotive suspensions," *Computing & Control Engineering Journal 5(3),* pp. 143-148. 1994.

[3] M. Appleyard and P. E. Wellstead, "Active suspensions: some background," *Control Theory and Applications, IEE Proceedings,* vol. 142, pp. 123-128, 1995.

[4] L. R. Miller, "Tuning passive, semi-active, and fully active suspension systems," Proceedings of the 27th IEEE Conference on Decision and Control, 1988.

[5] A. A. Ferri and B. S. Heck, "Semi-active suspension using dry friction energy dissipation," Presented at American Control Conference, 1992.

[6] X. D. Xue, K. W. E. Cheng, Z. Zhang, J. K. Lin, D. H. Wang, Y. J. Bao, M. K. Wong and N. Cheung, "Study of art of automotive active suspensions," Presented at the 4th International Conference on Power Electronics Systems and Applications (PESA), Hong Kong, 2011.

[7] V. Bhandari and S. C. Subramanian, "Development of an electronically controlled pneumatic suspension for commercial vehicles," in *2010 International Conference on Power, Control and Embedded Systems (ICPCES), ,* 2010, pp. 1-6.

[8] M. Satoh, N. Fukushima, Y. Akatsu, I. Fujimura and K. Fukuyama, "An active suspension employing an electrohydraulic pressure control system," in *Proceedings of the 29th IEEE Conference on Decision and Control*, pp. 2226-2231 vol.4*,* 1990.

[9] R. Rajamani and J. K. Hedrick, "Performance of active automotive suspensions with hydraulic actuators: Theory and experiment," in *American Control Conference,* pp. 1214-1218 vol.21, 1994.

[10] M. Gubitosa, J. Anthonis, N. Albarello and W. Desmet, "A system engineering approach for the design optimization of a hydraulic active suspension," in *IEEE Vehicle Power and Propulsion Conference, VPPC '09.*, pp. 1122-1130*,* 2009.

[11] Haiping Du and Nong Zhang, "Fuzzy Control for Nonlinear Uncertain Electrohydraulic Active Suspensions with Input Constraint," *IEEE Transactions on Fuzzy Systems,* vol. 17, pp. 343-356, 2009.

[12] Han-Shue Tan and T. Bradshaw, "Model identification of an automotive hydraulic active suspension system," in *Proceedings of the American Control Conference*, pp. 2920-2924 vol.5*,* 1997.

[13] B. L. J. Gysen, J. J. H. Paulides, J. L. G. Janssen and E. A. Lomonova, "Active Electromagnetic Suspension System for Improved Vehicle Dynamics," *IEEE Transactions on Vehicular Technology,* vol. 59, pp. 1156-1163, 2010.

[14] J. Paulides, E. Lomonova and A. Vandenput, "Design considerations for an active electro-magnetic suspension system," in *IEEE International Magnetics Conference (INTERMAG 2006),* pp. 774-774, 2006.

[15] M. Chaves, J. Maia and J. Esteves, "Analysis of an electromagnetic automobile suspension system," in *18th International Conference on Electrical Machines, ICEM 2008*, pp. 1-4*, 2008*.

[16] Jiabin Wang, Weiya Wang, K. Atallah and D. Howe, "Design of a linear permanent magnet motor for active vehicle suspension," in *IEEE International Electric Machines and Drives Conference, IEMDC '09*, pp. 585-591*,* 2009.

[17] A. Stribrsky, K. Hyniova, J. Honcu and A. Kruczek, "Energy recuperation in automotive active suspension systems with linear electric motor," Presented at Mediterranean Conference on Control & Automation, MED '07,2007.

[18] B. L. J. Gysen, T. P. J. van der Sande, J. J. H. Paulides and E. A. Lomonova, "Efficiency of a regenerative direct-drive electromagnetic active suspension," *IEEE Transactions on Vehicular Technology, 60(4),* pp. 1384-1393. 2011.

[19] Yongchao Zhang, Kun Huang, Fan Yu, Yonghui Gu and Daofei Li, "Experimental verification of energy-regenerative feasibility for an automotive electrical suspension system," Presented at IEEE International Conference on Vehicular Electronics and Safety, ICVES, 2007.

[20] M. Montazeri-Gh and M. Soleymani, "Investigation of the energy regeneration of active suspension system in hybrid electric vehicles," *IEEE Transactions on Industrial Electronics, 57(3),* pp. 918-925, 2010.

[21] P. Hsu, "Power recovery property of electrical active suspension systems," Presented at Proceedings of the 31st Intersociety Energy Conversion Engineering Conference, IECEC 96, 1996.

[22] S. Buma, H. Kajino, T. Takahashi and S. Doi, "Consideration of a human dynamic characteristic and performance evaluation of an electric active suspension," in *IEEE/ASME International Conference on Advanced Intelligent Mechatronics, AIM 2008* , pp. 1030-1036, 2008.

[23] Scott Doggett, "Michelin to Commercialize Active Wheel; Technology to Appear in 2010 Cars," Green Car Advisor, Edmunds,com, Sept. 15, 2009 .

[24] W. D. Jones, "Easy ride: Bose Corp. uses speaker technology to give cars adaptive suspension," *IEEE Spectrum,* vol. 42, pp. 12-14, 2005.

[25] I. Martins, J. Esteves, G. D. Marques and F. Pina da Silva, "Permanent-magnets linear actuators applicability in automobile active suspensions," *IEEE Transactions on Vehicular Technology,* vol. 55, pp. 86-94, 2006.

[26] B. L. J. Gysen, J. L. G. Janssen, J. J. H. Paulides and E. A. Lomonova, "Design Aspects of an Active Electromagnetic Suspension System for Automotive Applications," *IEEE Transactions on Industry Applications,* vol. 45, pp. 1589-1597, 2009.

[27] Seungho Lee and Won-jong Kim, "Active Suspension Control With Direct-Drive Tubular Linear Brushless Permanent-Magnet Motor," *IEEE Transactions on Control Systems Technology ,* vol. 18, pp. 859-870, 2010.

[28] Jiabin Wang, Weiya Wang and K. Atallah, "A Linear Permanent-Magnet Motor for Active Vehicle Suspension," *IEEE Transactions on Vehicular Technology ,* vol. 60, pp. 55-63, 2011.

[29] Byeong-Seok Lee, Han-Kyung Bae, P. Vijayraghavan and R. Krishnan, "Design of a linear switched reluctance machine," *IEEE Transactions on Industry Applications, 36(6),* pp. 1571-1580. 2000.

[30] Wai-Chuen Gan and N. C. Cheung, "Design of a linear switched reluctance motor for high precision applications," Presented at IEEE International Electric Machines and Drives Conference, IEMDC, 2001 .

[31] U. S. Deshpande, J. J. Cathey and E. Richter, "High-force density linear switched reluctance machine," *IEEE Transactions on Industry Applications ,* vol. 31, pp. 345-352, 1995.

[32] U. Deshpande, "Two-dimensional finite-element analysis of a high-force-density linear switched reluctance machine including three-dimensional effects," *IEEE Transactions on Industry Applications,* vol. 36, pp. 1047-1052, 2000.

[33] N. Vattikuti, R. Vandana and B. G. Fernandes, "A novel high force density linear segemented switched reluctance machine," in *34th Annual Conference of IEEE Industrial Electronics, IECON 2008*, pp. 1083-1088*,* 2008.

[34] Cheng-Tsung Liu and Tsung-Shiun Chiang, "On the magnetic saturation analyses of a micro linear switched-reluctance motor," *IEEE Transactions on Magnetics,* vol. 40, pp. 2861-2863, 2004.

[35] Hong Sun Lim, R. Krishnan and N. S. Lobo, "Design and Control of a Linear Propulsion System for an Elevator Using Linear Switched Reluctance Motor Drives," *IEEE Transactions on Industrial Electronics ,* vol. 55, pp. 534-542, 2008.

[36] Hong Sun Lim and R. Krishnan, "Ropeless elevator with linear switched reluctance motor drive actuation systems," *IEEE Transactions on Industrial Electronics, 54(4),* pp. 2209-2218. 2007.

[37] Jae-Hak Choi, Tae Heoung Kim, K. Jang and Ju Lee, "Geometric and electrical optimization design of SR motor based on progressive quadratic response surface method," *IEEE Transactions on Magnetics,* vol. 39, pp. 3241-3243, 2003.

[38] B. Mirzaeian, M. Moallem, V. Tahani and C. Lucas, "Multiobjective optimization method based on a genetic algorithm for switched reluctance motor design," *IEEE Transactions on Magnetics ,* vol. 38, pp. 1524-1527, 2002.

[39] R. T. Naayagi and V. Kamaraj, "A comparative study of shape optimization of SRM using genetic algorithm and simulated annealing," Presented at Annual IEEE INDICON, 2005.

[40] Changhwan Choi, Daeok Lee and Kyihwan Park, "Fuzzy design of a switched reluctance motor based on the torque profile optimization," *IEEE Transactions on Magnetics ,* vol. 36, pp. 3548-3550, 2000.

[41] M. Divandari and A. Dadpour, "Radial force and torque ripple optimization for acoustic noise reduction of SRM drives via fuzzy logic control," Presented at 9th IEEE/IAS International Conference on Industry Applications (INDUSCON), 2010.

[42] H. Sahraoui, H. Zeroug and H. A. Toliyat, "Switched reluctance motor design using neural-network method with static finite-element simulation," *IEEE Transactions on Magnetics, 43(12),* pp. 4089-4095, 2007.

[43] S. Brisset and P. Brochet, "Optimization of switched reluctance motors using deterministic methods with static and dynamic finite element simulations," *IEEE Transactions on Magnetics ,* vol. 34, pp. 2853-2856, 1998.

[44] A. M. Stankovic, G. Tadmor, Z. J. Coric and I. Agirman, "On torque ripple reduction in current-fed switched reluctance motors," *IEEE Transactions on Industrial Electronics, 46(1),* pp. 177-183, 1999.

[45] P. L. Chapman and S. D. Sudhoff, "Design and precise realization of optimized current waveforms," *IEEE Transactions on Power Electronics, 17,* pp. 76-83. 2002.

[46] S. K. Sahoo, S. K. Panda and Jian-Xin Xu, "Indirect torque control of switched reluctance motors using iterative learning control," *IEEE Transactions on Power Electronics,* vol. 20, pp. 200-208, 2005.

[47] C. Mademlis and I. Kioskeridis, "Performance optimization in switched reluctance motor drives with online commutation angle control," *IEEE Transactions on Energy Conversion,* vol. 18, pp. 448-457, 2003.

[48] N. T. Shaked and R. Rabinovici, "New procedures for minimizing the torque ripple in switched reluctance motors by optimizing the phase-current profile," *IEEE Transactions on Magnetics, 41(3),* pp. 1184-1192, 2005.

[49] M. Shirahase, S. Morimoto and M. Sanada, "Torque ripple reduction of SRM by optimization of current reference," Presented at International Power Electronics Conference (IPEC), 2010.

[50] M. Ilic-Spong, T. J. E. Miller, S. R. Macminn and J. S. Thorp, "Instantaneous Torque Control of Electric Motor Drives," *Power Electronics, IEEE Transactions on,* vol. PE-2, pp. 55-61, 1987.

[51] R. B. Inderka and R. W. A. A. De Doncker, "DITC-direct instantaneous torque control of switched reluctance drives," *IEEE Transactions on Industry Applications,* vol. 39, pp. 1046-1051, 2003.

[52] J. Liang, D. -. Lee and J. -. Ahn, "Direct instantaneous torque control of switched reluctance machines using 4-level converters," *Electric Power Applications, IET 3(4),* pp. 313-323, 2009.

[53] N. H. Fuengwarodsakul, M. Menne, R. B. Inderka and R. W. De Doncker, "High-dynamic four-quadrant switched reluctance drive based on DITC," *IEEE Transactions on Industry Applications, 41(5),* pp. 1232-1242. 2005.

[54] S. K. Sahoo, S. K. Panda and J. X. Xu, "Iterative learning control based direct instantaneous torque control of switched reluctance motors," Presented at 2004 IEEE 35th Annual Power Electronics Specialists Conference, PESC 04, 2004.

[55] M. Kaleemullah, W. F. Faris and F. Hasbullah, "Design of robust H∞, fuzzy and LQR controller for active suspension of a quarter car model," Presented at 2011 4th International Conference on Mechatronics (ICOM), 2011.

[56] R. Krtolica and D. Hrovat, "Optimal active suspension control based on a half-car model: An analytical solution," *IEEE Transactions on Automatic Control, 37(4),* pp. 528-532. 1992.

[57] A. Kruczek and A. Stribrsky, "A full-car model for active suspension - some practical aspects," Presented at Proceedings of the IEEE International Conference on Mechatronics, ICM '04, 2004.

[58] R. Darus and Y. M. Sam, "Modeling and control active suspension system for a full car model," Presented at 5th International Colloquium on Signal Processing & its Applications, CSPA 2009, 2009.

[59] R. Darus and Y. M. Sam, "Modeling and control active suspension system for a full car model," Presented at 5th International Colloquium on Signal Processing & its Applications, CSPA, 2009.

[60] B. L. J. Gysen, J. L. G. Janssen, J. J. H. Paulides and E. A. Lomonova, "Design Aspects of an Active Electromagnetic Suspension System for Automotive Applications," *IEEE Transactions on Industry Applications,* vol. 45, pp. 1589-1597, 2009.

[61] Abhishek Chaliha, "Sprung mass and unsprung mass," zigwheels.com, 05 Aug, 2011.

[62] S. Ahmad and M. O. Tokhi, "Linear quadratic regulator (LQR) approach for lifting and stabilizing of two-wheeled wheelchair," Presented at 2011 4th International Conference on Mechatronics (ICOM), 2011.

[63] I. Husain and M. Ehsani, "Torque ripple minimization in switched reluctance motor drives by PWM current control," *IEEE Transactions on Power Electronics, 11(1),* pp. 83-88. 1996.

[64] K. Ramu, "*Switched Reluctance Motor Drives: Modeling, Simulation, Analysis, Design, and Application,"* FL: CRC Press, Boca Raton, 2001.

[65] F. Daldaban and N. Ustkoyuncu, "A new double sided linear switched reluctance motor with low cost," *Energy Conversion and Management,* vol. 47, pp. 2983-2990, 11, 2006.

[66] J. G. Amoros and P. Andrada, "Sensitivity analysis of geometrical parameters on a double-sided linear switched reluctance motor," *IEEE Transactions on Industrial Electronics, 57(1),* pp. 311-319. 2010.

[67] Y. Sofiane, A. Tounzi, F. Piriou and M. Liese, "Study of head winding effects in a switched reluctance machine," *IEEE Transactions on Magnetics, 38(2),* pp. 989-992, 2002.

[68] U. Deshpande, "Two-dimensional finite element analysis of a high force density linear switched reluctance machine including three-dimensional effects," in *Industry Applications Conference*, pp. 2235-2241 vol.4*, 1999*.

[69] J. F. Gieras, G. E. Dawson and A. R. Eastham, "A new longitudinal end effect factor for linear induction motors," *IEEE Transactions on Energy Conversion, EC-2(1),* pp. 152-159. 1987.

[70] G. Meunier, "*The Finite Element Method for Electromagnetic Modeling," John Wiley & Sons,USA,* 2008.

[71] R. Arumugam, D. Lowther, R. Krishnan and J. Lindsay, "Magnetic field analysis of a switched reluctance motor using a two dimensional finite element model," *IEEE Transactions on Magnetics, 21(5),* pp. 1883-1885. 1985.

[72] B. Parreira, S. Rafael, A. J. Pires and P. J. C. Branco, "Obtaining the magnetic characteristics of an 8/6 switched reluctance machine: From FEM analysis to the experimental tests," *IEEE Transactions on Industrial Electronics, 52(6),* pp. 1635-1643. 2005.

[73] J. F. Gieras, G. E. Dawson and A. R. Eastham, "A new longitudinal end effect factor for linear induction motors," *IEEE Transactions on Energy Conversion, EC-2(1),* pp. 152-159. 1987.

[74] J. Bastos and N. Sadowski, "*Electromagnetic Modeling by Finite Element Methods," Marcel Dekker Inc., Switzerland,* 2003.

[75] A.Matveev, E.Lomonova, "A new comprehensive approach to estimation of end-effects in switched reluctance motors," Presented at Proceedings ICEM2002, 2002.

[76] A. M. Michaelides and C. Pollock, "Effect of end core flux on the performance of the switched reluctance motor," *IEE Proceedings of Electric Power Applications,* vol. 141, pp. 308-316, 1994.

[77] F. Sahin, H. B. Ertan and K. Leblebicioglu, "Optimum geometry for torque ripple minimization of switched reluctance motors," *IEEE Transactions on Energy Conversion,* vol. 15, pp. 30-39, 2000.

[78] S. Jebarani Evangeline and S. Suresh Kumar, "Torque ripple minimization of switched reluctance drives - A survey," in *5th IET International Conference on Power Electronics, Machines and Drives (PEMD 2010),* pp. 1-6 *,* 2010.

[79] I. Husain, "Minimization of torque ripple in SRM drives," *IEEE Transactions on Industrial Electronics,* vol. 49, pp. 28-39, 2002.

[80] P. J. Lawrenson, J. M. Stephenson, N. N. Fulton, P. T. Blenkinsop and J. Corda, "Variable-speed switched reluctance motors," *IEE Proceedings B on Electric Power Applications,* vol. 127, pp. 253-265, 1980.

[81] M. N. Anwar, I. Husain and A. V. Radun, "A comprehensive design methodology for switched reluctance machines," *IEEE Transactions on Industry Applications,* vol. 37, pp. 1684-1692, 2001.

[82] Jae-Hak Choi, Tae Heoung Kim, K. -. Jang and Ju Lee, "Geometric and electrical optimization design of SR motor based on progressive quadratic response surface method," *IEEE Transactions on Magnetics,* vol. 39, pp. 3241-3243, 2003.

[83] Zhen Gang Sun, N. C. Cheung, Shi Wei Zhao and Wai-Chuen Gan, "Magnetic Analysis of Switched Reluctance Actuators in Levitated Linear Transporters," *IEEE Transactions on Vehicular Technology,* vol. 59, pp. 4280-4288, 2010.

[84] Wai-Chuen Gan, N. C. Cheung and Li Qiu, "Position control of linear switched reluctance motors for high-precision applications," *IEEE Transactions on Industry Applications,* vol. 39, pp. 1350-1362, 2003.

[85] A. A. Goldenberg, I. Laniado, P. Kuzan and C. Zhou, "Control of switched reluctance motor torque for force control applications," *IEEE Transactions on Industrial Electronics,* vol. 41, pp. 461-466, 1994.

[86] I. Husain, "Minimization of torque ripple in SRM drives," *IEEE Transactions on Industrial Electronics,* vol. 49, pp. 28-39, 2002.

[87] S. K. Sahoo, S. K. Panda and J. X. Xu, "Direct torque controller for switched reluctance motor drive using sliding mode control," Presented at International Conference on Power Electronics and Drives Systems, PEDS 2005, 2005.

[88] R. B. Inderka, R. W. De Doncker and M. Krehenbrink, "On-line estimation of instantaneous torque in switched reluctance machine control," Presented at Proceedings of the 2000 IEEE International Symposium on Industrial Electronics, ISIE 2000, 2000.

[89] Zhengyu Lin, D. S. Reay, B. W. Williams and Xiangning He, "On-line torque estimation in a switched reluctance motor for torque ripple minimisation," Presented at2004 IEEE International Symposium on Industrial Electronics, 2004.

[90] T. J. E. Miller, "*Electronic Control of Switched Reluctance Machines," Newnes, Oxford,* 2001.

[91] Zhengyu Lin, D. S. Reay, B. W. Williams and Xiangning He, "Online modeling for switched reluctance motors using B-spline neural networks, *IEEE Transactions on Industrial Electronics, 54(6),* pp. 3317-3322. 2007.

[92] S. Paramasivam and R. Arumugam, "Hybrid fuzzy controller for speed control of switched reluctance motor drives," *Energy Conversion and Management 46(9-10),* pp. 1365-1378, 2005.

[93] D. S. Schramm, B. W. Williams and T. C. Green, "Torque ripple reduction of switched reluctance motors by phase current optimal profiling," Presented at 23rd Annual IEEE Power Electronics Specialists Conference, PESC '92 Record, 1992.

[94] I. Husain and M. Ehsani, "Torque ripple minimization in switched reluctance motor drives by PWM current control," *IEEE Transactions on Power Electronics ,* vol. 11, pp. 83-88, 1996.

[95] S. K. Sahoo, S. K. Panda and Jian-Xin Xu, "Indirect torque control of switched reluctance motors using iterative learning control," *IEEE Transactions on Power Electronics,* vol. 20, pp. 200-208, 2005.

[96] M. Ilic-Spong, T. J. E. Miller, S. R. Macminn and J. S. Thorp, "Instantaneous Torque Control of Electric Motor Drives," *IEEE Transactions on Power Electronics,* vol. PE-2, pp. 55-61, 1987.

[97] X. D. Xue, K. W. E. Cheng and S. L. Ho, "Optimization and Evaluation of Torque-Sharing Functions for Torque Ripple Minimization in Switched Reluctance Motor Drives," *IEEE Transactions on Power Electronics,* vol. 24, pp. 2076-2090, 2009.